6th October 2011

Proceedings of the Conference

Edited by:

Ing. Pavel Padevět, Ph. D.

Ing. Tomáš Plachý, Ph. D.

Ing. Pavel Tesárek, Ph. D.

Ing. Ondřej Zobal

Faculty of Civil Engineering

Czech Technical University in Prague

2011

ISBN 978-80-01-04892-4

Obsah

INFLUENCE OF NANOSILICA ON CONCRETE PROPERTIES

PETR BÍLÝ[1]

Abstract: *Results of numerous recent research projects have shown that silicon dioxide (SiO_2) nanoparticles can strongly affect mechanical properties and chemical resistance of concrete when mixed with cement. The paper tries to summarize state of the art in this new area of concrete science. Particular attention is devoted to the question of nanosilica (nS) impact on hydration process.*

Keywords: *Cement, concrete, hydration, nanosilica.*

1. INTRODUCTION

There are many reasons for adding silicon dioxide (SiO_2) particles to concrete mix. In fresh concrete, it increases cohesion, reduces segregation and bleeding. Enhanced mechanical properties and reduced permeability are observed in hardened concrete. The potential for the use of silica fume (SF) was known in the late 1940s. However, the first practical utilization became possible only after discovery of super-plasticizers in 1970s [1]. Today SF is quite commonly and successfully used to improve concrete characteristics. As the diameter of SF grains is less than 1 μm, it is also called microsilica.

Nanosilica (nS), that is composed of SiO_2 particles less than 100 nm in diameter, is considered to be a concrete admixture of the future. It yields the same benefits as microsilica, but with increased efficiency thanks to its higher specific surface area and reactivity. Research activities focused on this issue are very extensive and so we can expect rapid progress in foreseeable time. Following text is trying to provide the reader with a brief overview of current state of the art and prospective ways of further development.

[1] Ing. Petr Bílý; Department of Concrete and Masonry Structures, Faculty of Civil Engineering, Czech Technical University in Prague; Thákurova 7, 166 29 Prague, Czech Republic; petr.bily@fsv.cvut.cz

2. NANOSILICA PRODUCTION METHODS

Unlike silica fume, that is a byproduct of fabricating certain metals in electric furnaces, nanosilica has to be prepared intentionally. There are several production methods available.

The first one is based on a sol-gel process at room temperature. Starting materials (sodium silicate Na_2SiO_4 or organometallics) are dissolved, silica gel is precipitated, aged and filtered to become a xerogel. The xerogel is dried and burned or dispersed again to produce a concentrated dispersion (20 to 40 % solid content) suitable for use in concrete. Alternatively, vaporization of silica at 1500 – 2000 °C by reducing quartz in an electric furnace or precipitation of different precursors (sodium silicate, magnesium silicate and others) dispersed in a solution at temperatures between 50 to 100 °C can be implemented [2].

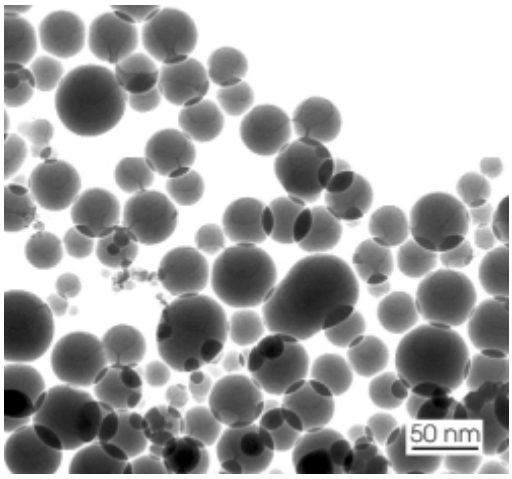

Fig. 1. Nanosilica particles observed using transmission electron microscopy (TEM), reprinted from [6].

Lázaro and Brouwers [3] proposed a process of obtaining nS on industrial scale in large quantities and for low costs. Ground olivine rock is treated by sulphuric acid, precipitated and gravitationally separated from the solution.

In compliance with contemporary struggle for being environmentally friendly, Liou and Yang [4] used rice husk as a raw material to prepare nS. Rice husk is rich in silica (about 20 % wt.) and the annual global production of this commodity is more than 100 million tons, without wider commercial utilization. Nanosilica can be extracted by relatively simple and cheap dissolution-precipitation technique. Even more progressive approach was applied by Estevez et al. [5]. They fed Californian red worms with rice husk, collected created humus and synthesized nS from this resource with 88% efficiency.

3. PRINCIPLES OF CONCRETE PROPERTIES IMPROVEMENTS

As mentioned in the introduction, nS is added to concrete mix because of its possitive impact on concrete properties.

The main advantage of silica is its pozzolanic activity. As the portland cement begins to react chemically, it releases calcium hydroxide (portlandite, $Ca(OH)_2$). Nanosilica reacts with $Ca(OH)_2$ to develop the strength carrying structure of cement – calcium silicate hydrate (CSH). Nanomaterials are well known for their influence on cement hydration. Generally, each crystallization is conditioned by presence of nucleation centers. Properties of resulting structure are largely defined by properties of these nuclei. The finer the nuclei, the finer CSH crystals are formed. As nS particles are at least 200 times smaller than cement grains, much better hydration levels are obtained thanks to higher specific surface area and reactivity of the material. Presence of nS in the mix leads to more rigid cement paste that contains significantly lower share of $Ca(OH)_2$ as compared with CSH, resulting in increased mechanical properties.

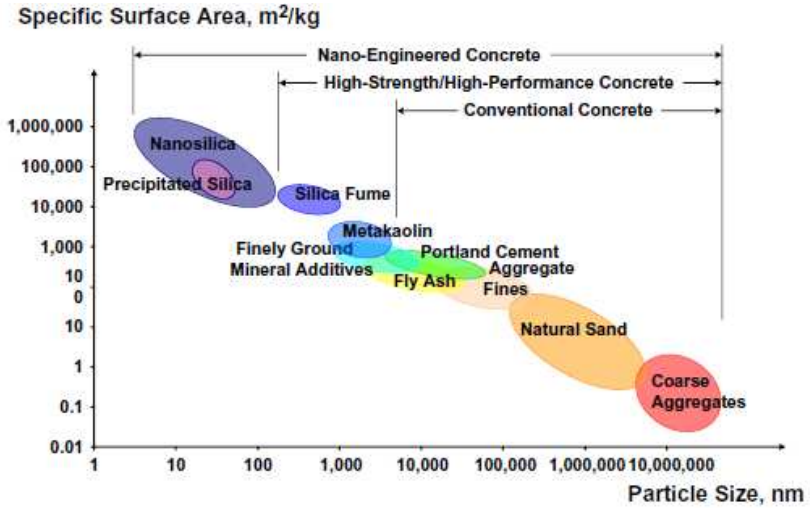

Fig. 2. Particle size and specific surface area of concrete related materials, reprinted from [6].

Nanosilica can serve also as filling material lowering porosity of cement paste. Just like fine aggregate fills in the spaces between coarse aggregate, nS particles occupy the voids between cement grains and CSH crystals. In this way, immobilization of free water is accomplished. Lower bleeding and segregation and better overall chemical resistance of concrete is achieved. Nanosilica doped concrete also shows higher packing density that contributes to higher modulus of elasticity. Some examples of experiments proving abovementioned facts are given in the next chapter.

4. EXAMPLES OF CONCRETE PROPERTIES IMPROVEMENTS

Belkowitz and Armentrout [7] prepared five different cement pastes – plain portland cement paste, silica fume cement paste and three nanosilica cement pastes that differed by the average size of nS particles used. All the mixes contained 425 kg/m^3 of portland cement, 133 kg/m^3 of water, 1,9 *l*/m^3 of high-range water reducer and 21 kg/m^3 of micro- or nanosilica (in case of additised pastes). The results are transparently represented in figure 3. Early strength development was much faster for nanosilica than for microsilica. With 8-nm nS particles, 28-day compressive strength was higher by almost 50 % compared to plain cement paste. Obtained strengths also support the assumption of increasing nanosilica efficiency with decreasing particle size.

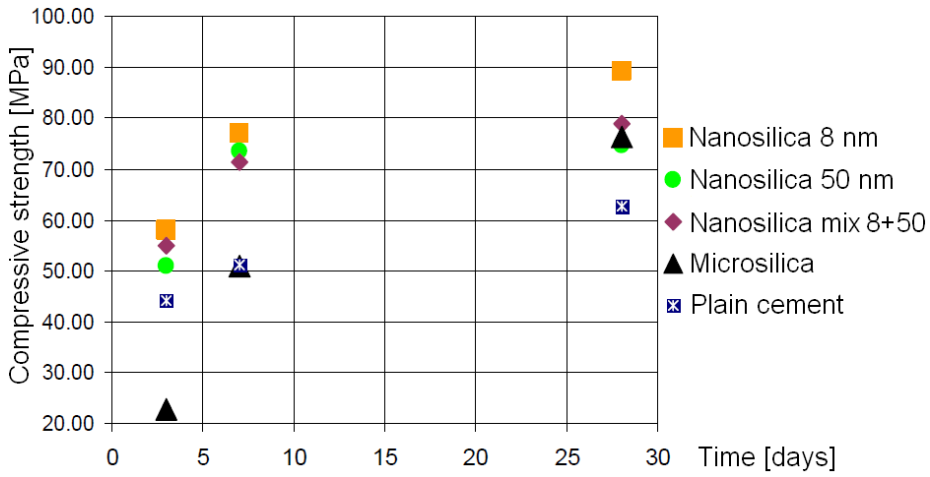

Fig. 3. Averaged compressive strength data for different mixes, adapted from [7].

Gaitero et al. [8] focused on influence of aggressive chemical agents on cement pastes with silica nanoparticles. More specifically, they studied calcium leaching, a degradation process consisting in the progressive dissolution of the cement paste as a consequence of the migration of calcium ions to the aggressive solution. Four different types of nS (three in the form of colloidal dispersion and a dry nanosilica powder) were added to the cement, the dosage was 6 % from the weight of cement in all cases. After 28 days of curing, some of the specimens were tested and the rest was placed into a bath of ammonium nitrate solution where they stayed for 9, 21, 41 or 63 days. Performance of cement pastes was considerably improved by nS both before and during the degradation process. Initial compressive strength was higher, the reduction of strength by calcium leaching was less significant than in reference plain cement samples (see fig. 4). This was due to less porosity of the material, reduced portlandite content and changes undergone by the CSH gel that made it more resistant to the decalcification.

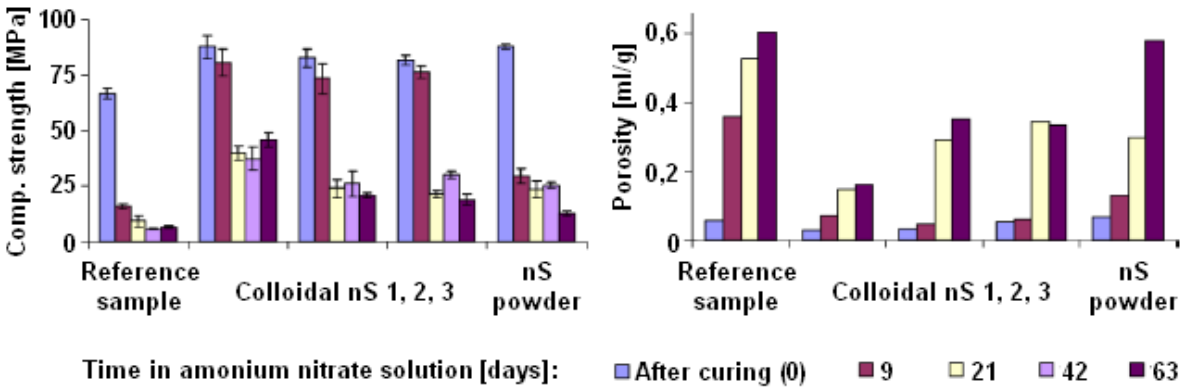

Fig. 4. Compressive strength (left) and total pore volume measured by mercury intrusion porosimetry (right), as a function of the degradation time, adapted from [8].

Hosseini et al. [9] investigated effect of nanosilica on recycled aggregate concretes. They studied compressive strength development in eight different mixes whose compositions and mechanical properties are summarized in table 1. The main outcome was that while the use of recycled aggregate caused ca 18 % drop in compressive strength, addition of only 3 % of cement weight nS eliminated this negative effect. Scanning electron microscopy (SEM) studies confirmed that the application of recycled aggregate led to increased porosity of interstitial transition zone (ITZ) between cement paste and aggregates, but when nS was applied, these voids were omitted, ITZ became denser, more uniform (see figure 5) and therefore was able to transfer higher compressive stresses.

Tab. 1. Concrete mixture proportions and compressive strength development as recorded by the authors of study [9].

Mixture	Aggregate	Water	Cement	nS	Compressive strength [MPa]			
		[kg/m^3]	[kg/m^3]	[kg/m^3]	3 days	7 days	14 days	28 days
NC-400	Natural	177.2	400	0	15.2	24.3	29.6	34.2
RA1-400	Recycled	201.6	400	0	12.6	19.6	24.3	28.1
RA2-400	Recycled + 1.5 % nS	201.6	394	6	13.9	19.6	24.3	28.1
RA3-400	Recycled + 3 % nS	201.6	388	12	15.9	24.6	30.1	35.3
NC-450	Natural	196.3	450	0	19.4	31.4	37.3	41.8
RA1-450	Recycled	219.4	450	0	16.3	25.1	31.2	35.3
RA2-450	Recycled + 1.5 % nS	219.4	443.25	6.75	17.6	29.3	35.4	40.1
RA3-450	Recycled + 3 % nS	219.4	436.5	13.5	20.9	32.1	39.1	43.7

Many further instances of nS-enriched concrete tests reporting positive impact on mechanical and chemical resistance can be found in papers [2] and [6], including reduction of bleeding and segregation of fresh concrete.

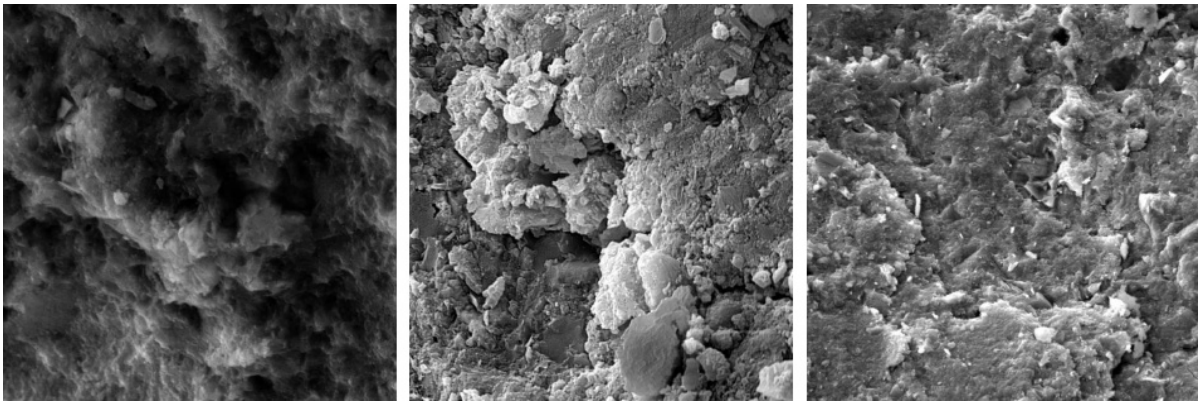

Fig. 5. SEM photos of ITZ. From left to right mixes NC-400, RA2-400 and RA3-400. Reprinted from [9].

5. DRAWBACKS OF NANOSILICA

Unfortunately, nanosilica has also several disadvantages that limit its practical exploitation in concrete industry in the present time.

In some cases, tendency of particle crowding was observed in nS [9]. However, this issue is not such a big problem like in case of carbon nanotubes or carbon nanofibers. Usually good dispersion can be achieved quite easily by sufficient dose of super-plasticizer that is necessary to ensure workability anyway.

Shrinkage can be significantly increased by nS. Li et al. [10] reported values by 198.7 % higher compared to common concrete after addition of 0.75 % of nanosilica with respect to cement content. They also found no improvement in compressive strength. Drawing a comparison between this fact and positive conclusions of other authors (chapter 4), we can define another problem. By changing the dosage or physical properties of nS (average particle diameter, specific surface area etc.), effect on concrete properties can fluctuate in very wide range and improvement of characteristics can't be guaranteed in advance. However, the same is with all admixtures, newly designed concrete mix always has to be properly tested before it is used, so that this fact should not disqualify nanosilica by no means.

Price of nS also can be particularly limiting factor as it increases total construction costs, but this rise can be justified by acquired added value. In these days nanosilica powder is commercially available from $ 5 per kilogram, depending on particle size and ordered quantity. Water suspension can be purchased from $ 1.5 per liter, the amount differs with dry content of nS.

Last but not least, health and environment issues should be concerned. Ultrafine SiO_2 nanoparticles have been classified as human carcinogens, at high concentrations in water (more than 5 g/*l*) have also been reported to damage bacteria [11]. Rats and mice exposed to various types of nanosilica particles suffered from pulmonary inflammation, tissue damage or cardiovascular diseases [12]. Further investigation will be necessary to define safety limits for nanomaterials exposure and their life cycle in the nature. Anyway, it is appropriate to gain maximum possible control of nanomaterials flow through the construction process from the beginning to the end. Workers that will get into everyday contact with them should use protective measures (respirators, coveralls). Users should not be affected as nanosilica will be embedded in concrete matrix tightly. What seems to be the biggest problem is demolition. Removal of structure is usually accomplished by means like explosives, bulldozers and others that do not allow to fully control release of dust to the environment, where it could negatively impact on organisms or water quality. The same concern is applicable to disposal of construction waste.

6. CONCLUSION

Nanosilica represents the future of concrete technology. Plenty of abovementioned facts strongly support this statement. Although several issues impede practical application nowadays, numerous research activities exert on solving these problems and considerable progress is to be expected in the near future.

ACKNOWLEDGEMENT

The author is indebted to the support of Studentská grantová soutěž ČVUT 2011 (SGS 2011) under grant SGS11/106/OHK1/2T/11 „Engineered Concretes and Cement Composites“.

REFERENCES

[1] Holland, T.C.; 2005. *Silica Fume User's Manual*, Silica Fume Association, Washington D.C., USA, 194 p.

[2] Quercia, G.; Brouwers, H.J.H.; 2010. *Application of nanosilica (nS) in concrete mixtures*, 8th fib PhD Symposium in Kgs. Lyngby, Denmark, 6 p.

[3] Lázaro, A.; Brouwers, H.J.H.; 2010. *Nano-silica production by a sustainable process; application in building materials*, 8th fib PhD Symposium in Kgs.Lyngby, Denmark, 6 p.

[4] Liou, Tzong-Horng; Yang, Chun-Chen; 2011. *Synthesis and surface characteristics of nanosilica produced from alkali-extracted rice husk ash,* Materials Science and Engineering B (Elsevier), vol. 176, pp. 521 – 529.

[5] Estevez, M. et al.; 2009. *Silica nano-particles produced by worms through a bio-digestion process of rice husk,* Journal of Non-Crystalline Solids (Elsevier), vol. 355, pp. 844 – 850.

[6] Sobolev, K.; Ferrada Gutiérrez, M.; 2005. *How Nanotechnology Can Change the Concrete World,* American Ceramic Socienty Bulletin, vol. 84, no. 11, pp. 16 – 20.

[7] Belkowitz, J.S.; Armentrout, Daniel; 2010. *An Investigation of Nano Silica in the Cement Hydration Process,* 2010 Concrete Sustainability Conference, 15 p.

[8] Gaitero, J.J.; Zhu, W.; Campillo, I.; 2009. *Multi-scale Study of Calcium Leaching in Cement Pastes with Silica Nanoparticles,* Nanotechnology in Construction 3 – Proceedings of the NICOM3 (Springer), pp. 193 – 198.

[9] Hosseini, P. et al.; 2009. *Use of Nano-SiO_2 to Improve Microstructure and Compressive Strength of Recycled Aggregate Concrete,* Nanotechnology in Construction 3 – Proceedings of the NICOM3 (Springer), pp. 215 – 221.

[10] Li, P.-F.; Zhang, Q.; Li, J.-J.; 2010. *Road performance of cement concrete with nano-SiO_2,* Journal of Chang'an University (Natural Science Edition), vol. 30, issue 3, pp. 41 – 46.

[11] Lee, J.; Mahendra, S.; Alvarez, P.J.J.; 2009. *Potential Environmental and Human Health Impacts of Nanomaterials Used in the Concrete Industry,* Nanotechnology in Construction 3 – Proceedings of the NICOM3 (Springer), pp. 1 – 14.

[12] Napierska, D. et al.; 2010. *The nanosilica hazard: another variable entity.* Particle and Fibre Toxicology 2010, 7:39, 32 p.

EXPERIMENTAL VERIFICATION OF THE EXTERNAL FIXATOR FOR LENGTHENING OF LONG BONES

MIROSLAV PETRTÝL [1], FRANTIŠEK DENK [2], ALEŠ LERACH [3], PAVEL PADEVĚT [4]

Abstract: *The lengthening of long bones in children using the traction osteogenesis method is performed by the gradual distraction of the opposite ends of bone fragments. Mechanical factors are of major importance for the development of the callus between two successive elongations, as well as during the time of its consolidation and modelling. New designed external fixator accelerates the healing process and stimulates the formation of callus and subsequent ossification. The limitation of pain during the actual lengthening process such as by selecting the appropriate size and frequency of distraction steps together with dynamic effect is also equally important.*

Keywords: *prolongation, gradual distraction, biomechanics, external fixation, ossification*

1. BASIC PRINCIPLES OF LENGTHENING OF LONG BONES

The lengthening of long bones in children using the traction osteogenesis (desmogenesis) method is performed by the gradual stretching of the callus of the healing bone tissue, i.e. by the gradual lengthening of the opposite ends of bone fragments. Mechanical factors are of major importance for the development of the callus between two successive elongations, as well as during the time of its consolidation and modelling (after the completion of

[1] Prof. Ing. Miroslav Petrtýl, DrSc.; Laboratory of Biomechanics and Biomaterial engineering, Department of mechanics, Faculty of Civil Engineering, CTU in Prague; Thákurova 7, 160 00, Prague, Czech republic; petrtyl@fsv.cvut.cz

[2] Ing. arch. et Ing. František Denk; Laboratory of Biomechanics and Biomaterial engineering, Department of mechanics, Faculty of Civil Engineering, CTU in Prague; Thákurova 7, 160 00, Prague, Czech republic; frantisek.denk@fsv.cvut.cz

[3] Ing. Aleš Lerach; MEDIN Orthopaedics, a.s.; Jinonická 329, 150 07, Prague, Czech republic; ales.lerach@medin.cz

[4] Ing. Pavel Padevět, Ph.D.; Department of mechanics, Faculty of Civil Engineering, CTU in Prague; Thákurova 7, 160 00, Prague, Czech republic; pavel.padevet@fsv.cvut.cz

elongation). Changes in stresses and deformations initiated by external force and moment effects very efficiently regulate the velocity of healing, the formation of bearing structures in the tissue and, last, but not least, the development of adequate elastic and viscoelastic properties in the tissue.

Discussions are presently going on concerning possibilities of speeding up the healing of the callus and the metabolic processes of new formation of connective tissues. The laws affecting the velocity of the bone tissue regeneration (modelling) have not been formulated with due exactness yet. Clinical practice knows methods of speeding up the healing of diaphysal fractures (treated, for example, by intramedullar nails) with an effective application of dynamic force effects during the patient's gait.

The objective of the research was to develop an efficient tool for the elongation of long bones in children allowing the speeding up of osteogenesis through harmonically varied forces (or microdeformations induced in children during the day).

The method of bone fragment distraction using an external fixator (EF) has a tradition of more than a hundred years in clinical practice. The founder of modern external fixators was A. Lambote, who first designed and used a "fixateur externe" in 1907. A highly original method (so-called physiological collation) was developed in the second half of the 20th century by G.A. Ilizarov (in Kurgan, Russsia). He was the first researcher who successfully tested the compression-distraction method in clinical practice using a circular external fixator which stimulates the bone tissue growth. Based on clinical experience, he formulated the basic biomechanical conditions for neo-osteogenesis, which may be synoptically summed up as follows:

(1) ensure stability of external fixation of long bone fragments;
(2) observe a sufficiently long interval before the start of distraction;
(3) ensure in the maximum possible way the supply of bone fragments with extraosseous and medullary vessels;
(4) ensure daily distraction cycles with 1 mm elongations;
(5) after the completion of diaphyses lengthening observe a sufficient time interval for stable neutral fixation;
(6) allow loading of lengthened extremities from the very start of treatment.

Since Ilizarov's pioneering times there has been a rapid growth in the development of various types of lengtheners using both rings connected to transverse bars intersecting the diaphysis walls and one-sided lengtheners. All these types are characterized by a possibility of

imposing only static tensile forces, which exert a single daily elongation (i.e. distraction of bone fragments) by 1 - 1.5 mm.

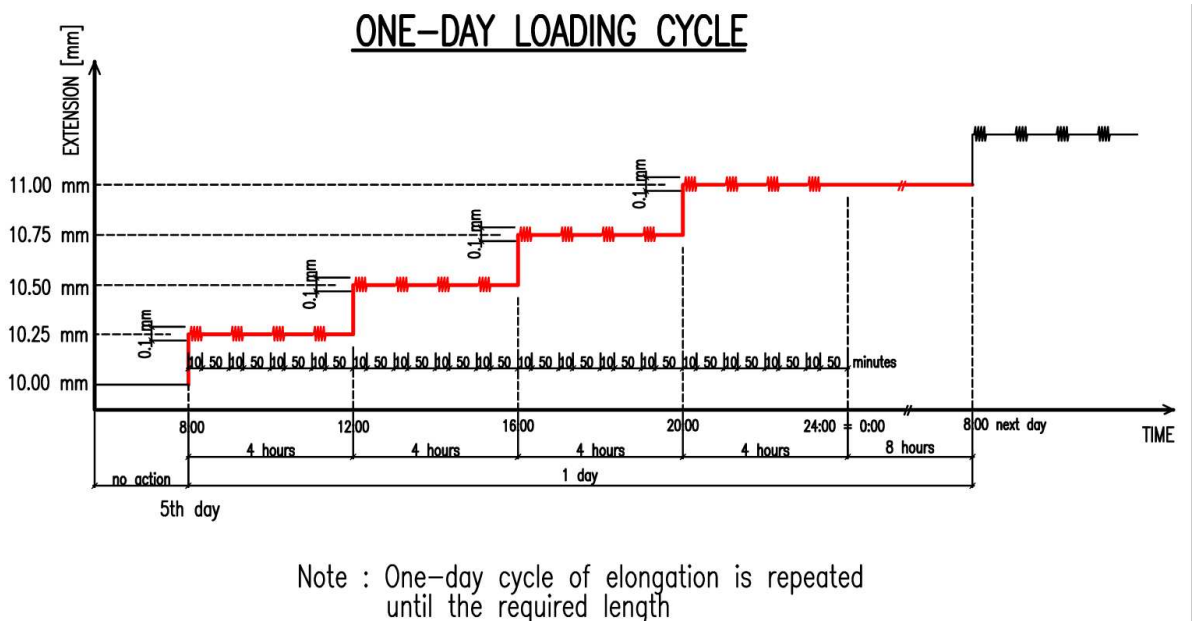

Fig. 1. The load cycle of regenerated bone tissue during every 24 hours

We have further methodologically extended Ilizarov's (and his successors') conditions by adding electronically regulated elongation (Fig. 1), consisting in a very careful gradual lengthening of the ends of bone fragments by 0.25 mm which takes place every 4 hours (16 hours in total). Successively, during 8 hours, the tissues were kept in a quiescent state (i.e. the time of the patient's sleep). With regard to the acceleration of healing, the tissues were loaded with cyclic deformations with amplitudes of oscillations of 0.1 mm during 4 x 4 hours, always for a period of 10 minutes. After each cyclic loading the healing tissues were kept in a quiescent state for a period of 50 minutes.

The methodology of traction neo-osteogenesis, i.e. new formation of bone tissue presented by our team, is biomechanically initiated by the action of its combined loading, i.e. by constant tensile stress and short-term repetitive cyclic load acting perpendicular to the plane of the osteotomy. After the initial (after-operation) relatively quiescent phase (i.e. before the initial loading), the biosynthesis of new tissue, the proliferation and differentiation of cells is dynamically in progress, in correlations with gradual lengthening with low magnitudes of amplitudes of 240 μm. The intensity of the metabolic activity in the cells highly depends on their supply with blood and on programmed functional loading of the lengthened proximity.

The designed electronically regulated lengthener (Fig. 2) speeds up desmogenic ossification. Its construction allows imposing tensile microdeformations and harmonically

varied forces with low amplitudes to tissues. These microdeformations and oscillation frequencies are controlled by means of an electronic unit.

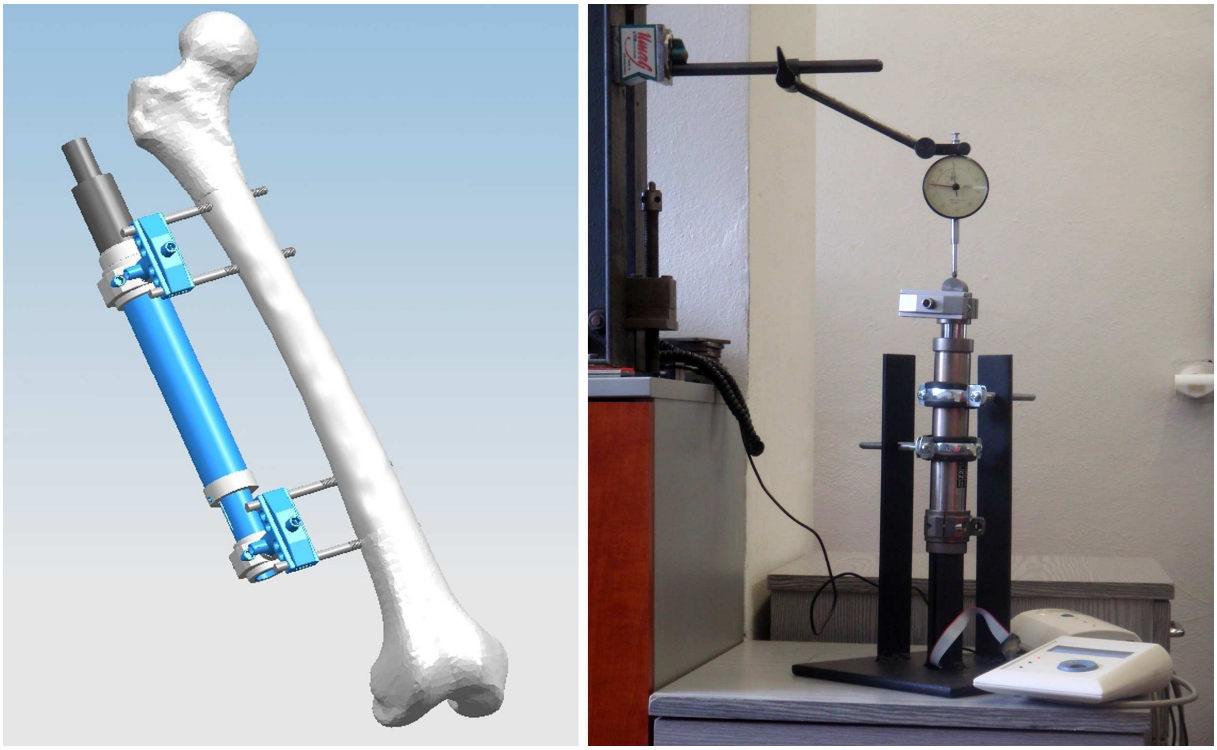

Fig. 2. The electronically regulated lengthener with programmable parameters of bone fragments shifts (on the left) and their induced harmonic oscillations (on the right)

2. EXPERIMENTAL VERIFICATION

Experimental testing of the external fixator for lengthening of the diaphysis consists of several related phases. The initial phase includes, in particular a preliminary verification of the basic physical and mechanical properties of the proposed structure and functionality of complex electronic eject mechanism with regard to ability of overcoming the resistance to the effects of variable loads.

2.1. STATIC LOAD TEST

The main principle of this type of experimental test is to verify the electromechanical pull-out system ability in overcoming resistance derived by centric constant load of 100 N, 300 N and 500 N acting in the axis of shaft. One of the predefined automatic programs for the progressive dynamic extension in the theoretical values of deflection amplitudes (200 µm x 5 after 2 hours) is activated during the test cycle. The result of measurements is to compare the actual absolute values of the total extension in a single program cycle (Fig. 3, Tab. 1). The default correlation factor represents the course of the reference test cycle without load.

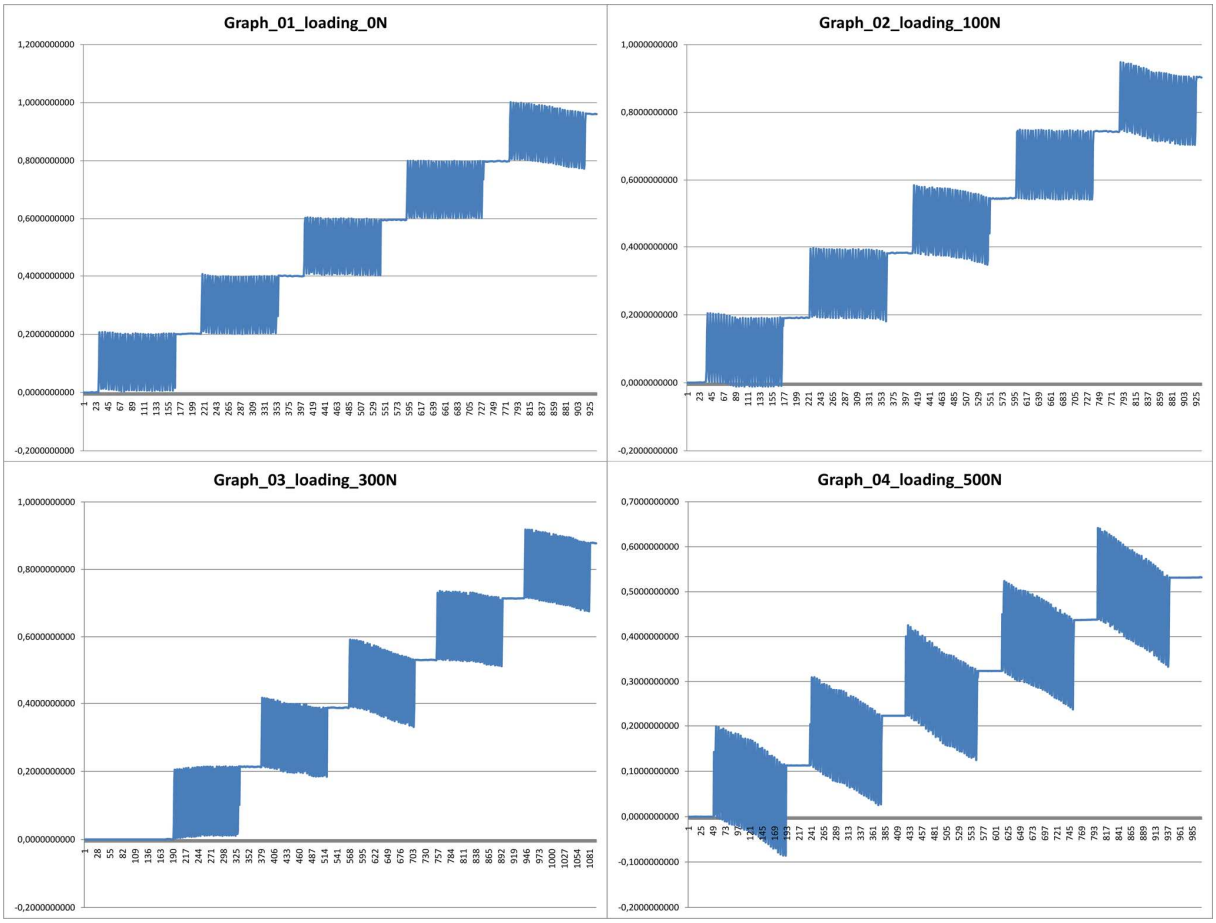

Fig. 3. Graphs of dependence of time and corresponding deflections in the test cycles for load 0 N, 100 N, 300 N, 500 N

Tab. 1. Recapitulation of the measured values of total and partial pull-out (μm)

Sub-series	0 N	100 N	300 N	500 N
1 (initial)	200.871	190.090	214.558	112.847
2	401.743	381.084	386.636	222.240
3	596.352	546.546	530.051	323.628
4	798.547	742.576	714.138	436.572
5 (final)	963.040	905.132	877.275	531.504
Theoretical extension	1000.000	1000.000	1000.000	1000.000
Percentage	96.30 %	90.51 %	87.73 %	53.15 %

2.2. DETERMINANTION OF PRESSURE RIGIDITY OF THE STRUCTURE

Whereas that the real axis of the load is positioned excentric and parallel to the shaft of external fixator, it is necessary to determine the effect of bending stiffness of the cantilevers with anchor nails, which provide positional anchoring and stabilizing the disrupted fragments of the shaft. Experimental determination of structural stiffness of the prolongator in compression was performed using an electromechanical testing machine MTS Alliance RT-30 with a range of ±0/30 kN. The external fixator was clamped between the press heads and loaded excentric in the axis of the femoral diaphysis future position. Experimental determination of stiffness is determined from the dependence of gradually increasing axial forces in the range from 0 to 500 N and the corresponding readings of the press head movements, which represents the mutual deformations of the ends of anchor nails, respectively mutual displacements of opposite surfaces of bone fragments (Tab. 2).

Tab. 2. Summary of deformation changes dependence in the loading process

Δ F (N)	20.490	23.900	97.700	100.000 *)
Δ u (mm)	0.052	0.065	0.251	0.243 *)
$k_p = \Delta F.\Delta u^{-1}$ (N.mm^{-1})	394.038	367.692	389.243	411.523

*) Measurement was terminated prematurely because of the collapse of the screw clamping during acting load of 250 N

2.3. WEIGHT DETERMINATION

Verification of basic physical and mechanical properties also includes determining the mass of the complete structural system, including electronic components and parts for clamping the femoral diaphysis fragments. Weight was determined using equipment KERN EW 6200-2NM with a range of 1/6200 g. The total weight of the complete assembly of the external fixator is 1865 g.

3. CONCLUSION

The following most important conclusions, which provide a picture of the effects of basic mechanical properties of the new external fixator for further testing and the conditions of future use in clinical practice, can be mentioned on the basis of presented results:

(1) Experimental verification of the real size of the shifts of the moving part of the external fixator according to the applied load indicates that the fixator body under the compressive normal load leads to a corresponding fall in the resulting strain values, and thus to the deviations between the actual displacements and theoretically determined values. From

this perspective, it is necessary to perform an initial calibration of the electromechanical pull-out system through an individual approach. This calibration will be performed on the basis of power assembled curve and the corresponding real effects of displacements from the performed load tests.

(2) The theoretical shift is characterized by extension value of the moving parts external fixator in the reference measurements (under zero load). The real shift is defined as the product of the theoretical value of the shift and reduction coefficients (calibration constants) that can be derived from assembled curves experimentally established from the dependency of deformations (on the stem of the external fixator) and sizes of the active load power.

(3) Accuracy of telescopic part deflection amplitudes of the external fixator is highly influenced by the structural system (due to the helical extension path). From this perspective, it is necessary to design devices for scanning the fair value of extension or number of revolutions of spindle shaft with a view to control of achieving the theoretical (prescribed) extension.

(4) In practical course of initial prolongation the active participation is expected the surrounding muscle and other connective tissue around the resected diaphysis. The immediate activation of resistance the surrounding connective tissue, which manifests reactionary pressure effect in the body of the external fixator, occurs within single distraction of opposite ends of the bone fragments. Comparing real and theoretical displacements of moving parts of the external fixator is ensured a unique determination of resistance size of connective tissue in the early hours and days after invasive intervention.

(5) The course of the diaphysis lengthening is in the initial stages influenced by the size of tensile resistance of the surrounding connective tissue and structural flexibility of the system including the interaction with external fixator cantilever anchor nails. The stiffness of the external fixator is manifested especially during normal walking of the patient, when there is movement in the callus as a result of natural cycles of load. In subsequent stages, the effect of stiffness emerging callus tissue between the bone fragments is gradually beginning to significantly contribute to the behavior of the entire system.

(6) Experimental verification of external fixator stiffness in pressure during eccentric loading in anchoring points to diaphysis provides the dependence of real movements of opposite ends of the bone fragments due to the applied load, especially in the initial stages of the process of lengthening. The fair values of the mutual movement of opposite ends of the bone fragments (Tab. 3), which can be simultaneously in accordance with the principle of

superposition combined with the regression curves shaft external fixator in centric pressure, can be derived from the observed constant stiffness of the external fixator.

Tab. 3. Calculation of bone fragments displacements from the specified stiffness constant of the structure

F (N)	100 N	300 N	500 N
Δ u (mm)	0.250	0.750	1.250

(7) The total weight of the complete assembly of the external fixator is 1865 g. In the next phase of the experiments will be solved lightness shaft fixator and the use of lightweight composite materials that will not reduce the overall rigidity.

ACKNOWLEDGEMENT

This article was based on the support of Grant No. SGS10/136/OHK1/2T/11, Advanced experimental methods, and within and supported by research plan No. 6840770012.

REFERENCES

[1] Bellemore, M.C. Advances in limb lengthening. SterilizAust, 12, 1993,p. 20-21.

[2] Frost H.M. The Utah paradigma of skeletal physiology. Vol. 1. Bone and Bones and Associated Problems, ISMNI, Greece , 2004, 427 pp.

[3] Illizarov G.A. Deviatov A.A. Operative elongation of the leg with simultaneous correction of the deformities, Ortop. Travmatol Protez, 30; 0969, pp.32-37.

[4] Ilizarov G.A. Basic principles of transosseous compression and distraction osteosynthesis. Ortop.Traum.Trot.,32,1971, pp. 7-15.

[5] Iobst C.A., Dahl M.T, Limb lengthening with submuscular plate stabilization: a case series and description of the technique. J. Perdiatr. Ortop., 2007, Jul-Aug; 27(5):pp. 504-509.

[6] Marotti G. The structure of bone tissue and the cellular control of their deposition. Ital. J. Anat.Embryol. 101, 1996, pp. 25-79.

[7] Mařík I., Sobotka Z.: Biomechanical coaction of external fixators in complications during the lengthening of lower extremities. In: Biomechanika člověka´98, Ed. Jelen et al., Praha:FTVS UK Praha, 1998, pp.58-60.

[8] Noonan K.J. et al. Distraction osteogenesis of the lower extremity with use of monolateral external fixation. A study of two hundred and sixty-one femora and tibiae. J. Bone Joint. Surg. Am,1968, Jun:80(6): 793-806.

[9] Petrtýl M., Danešová J. Dynamics of corticalis stiffening. Locomotor apparatus – advances in diagnostics, research and therapy, 10, 2004, No. 1-2, pp.49-60.

PREDICTION OF EFFECTIVE THERMAL CONDUCTIVITY OF NANOPOROUS MATERIALS USING MICROMECHANICAL METHODS

MARTIN DOŠKÁŘ[1], JAN ZEMAN[2]

Abstract: *The purpose of this paper is to examine the applicability of effective media theories to the prediction of effective thermal conductivity of nanocomposite materials. In particular, we examine well-established Mori-Tanaka and Self-Consistent scheme applied to nanoporous silica films with regular structure. It is found that the experimentally determined data can be fairly well reproduced by models accounting for the Kapitza resistance at the pore-matrix interface. Somewhat surprisingly, the optimal value of the resistance has been found to be negative.*

Keywords: *effective thermal conductivity, nanoporous materials, Mori-Tanaka method, Kapitza resistance*

1. INTRODUCTION

The increasing demands on material properties lead to a widespread use of micro- and nano-composite materials in virtually all areas of engineering. This, in turn, results in the need to predict relevant physical properties of composites directly from their composition. While this programme was highly succesfull for the classical micro-composites, e.g. [3], validity of these techniques at the nano-scale remains much less explored. Thus, the focus of this work is on the application of effective media theories to the prediction of effective conductivity of nanoporous media.

Concretely, two representatives of micromechanical models will be explored, namely the Mori-Tanaka (M-T) method and the Self-Consistent (S-C) scheme. These methods will be validated against experimental data obtained in [2] for the effective conductivity of

[1] Martin Doškář; Department of Mechanics, Faculty of Civil Engineering, CTU in Prague; Thákurova 7, 166 29 Prague 6, Czech Republic; martin.doskar@fsv.cvut.cz

[2] doc. Ing. Jan Zeman Ph.D., Department of Mechanics, Faculty of Civil Engineering, CTU in Prague, Thákurova 7, 166 29 Prague 6, Czech Republic; zemanj@cml.fsv.cvut.cz

nanoporous films. These material systems feature highly regular structures, which makes them ideally suited for the assessment of homogenization methods.

The remainder of this paper is organized as follows. Section 2 briefly reviews the principles of the micromechanical schemes used in the study. In Section 3, we compare their prediction against experimental data [2] and demonstrate the need to account for interfacial thermal resistance (also known as the Kapitza resistance) in the model. The accuracy of the improved model is analyzed in Section 4, and the obtained results are summarized in Section 5.

2. MICROMECHANICAL METHODS

Both micromechanical models used in this paper are based on the equivalent inclusion method. Its main idea is to replace an inhomogenity with an inclusion with the properties of the matrix phase, and subsequently to add inclusion heat flux so as to achieve equivalence with the original situation. Using continuity of the heat flux across the matrix-inclusion interface, it is possible to relate the overall thermal gradient and the thermal gradient in inclusion by means of the concentration factor. When interaction among individual inclusions is neglected, this information is sufficient to estimate the overall conductivity using the *dilute approximation method*, e.g. [1] and references therein. The resulting relation, however, is found to be to inaccurate for practical needs.

The *self-consistent method* accounts for the the presence of multiple inhomogenities by replacing the matrix thermal conductivity with effective thermal conductivity in the expression for the concentration factor:

$$A = \frac{\dim \lambda_m}{(\dim - 1)\lambda_m + \lambda_i} \tag{1}$$

where λ denotes thermal conductivity, index m refers to matrix properties, i stands for the inhomogenity and dim=2 for hexagonal arrangement of pores, while for the cubic arrangement, we set dim=3. This replacement leads to an implicit formula, which can be solved for two-phase materials in the closed form [3]

$$\lambda_{eff} = \frac{\alpha + \sqrt{\alpha^2 + 4(\dim - 1)\lambda_m \lambda_i}}{4(\dim - 1)} \tag{2}$$

$$\alpha = \lambda_m (\dim \varphi_m - 1) + \lambda_i (\dim \varphi_i - 1) \tag{3}$$

where φ is the volume fraction.

The *Mori-Tanaka method* deals with the presence of multiple inclusions in bulk by an additional thermal gradient caused by presence of inhomogenities in the matrix phase. This results in a modification of the concentration factor, otherwise the derivation of effective thermal conductivity formula is similar to the dilute approximation method [1]. The final relation reads as

$$\lambda_{eff} = (\varphi_m \lambda_m + \sum_{j=2}^{N} \varphi_i^j A_i^j \lambda_i^j)(\varphi_m I + \sum_{j=2}^{N} \varphi_i^j A_i^j)^{-1} \tag{4}$$

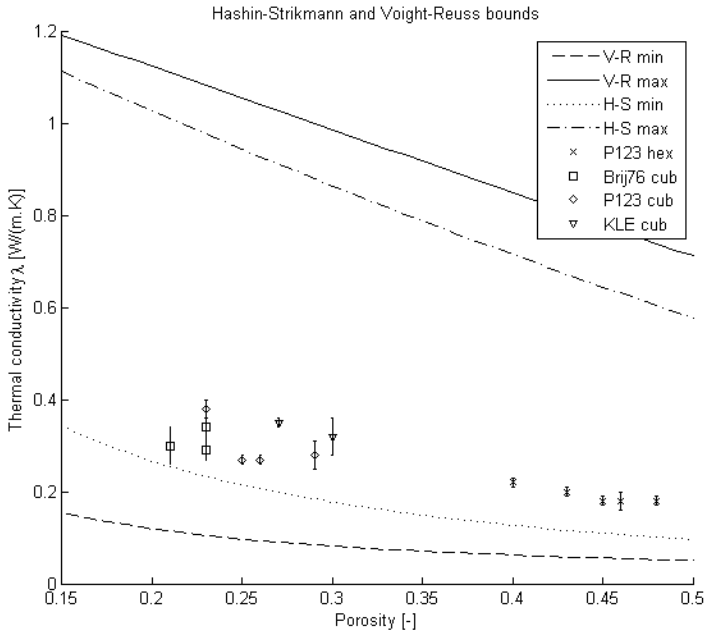

Fig. 1. Hashin-Strikmann and Voight-Reuss bounds

3. APPLICATION TO EXPERIMENTAL DATA

As the first step, the experimentally obtained thermal conductivities [2] are compared to the Hashin-Strikmann bounds (5), and the Voight-Reuss bounds (6):

$$\lambda_i (1 + \frac{3\varphi_m (\lambda_m - \lambda_i)}{3\lambda_i + \varphi_i (\lambda_m - \lambda_i)}) \leq \lambda_{eff} \leq \lambda_m (1 - \frac{3\varphi_i (\lambda_m - \lambda_i)}{3\lambda_m - \varphi_m (\lambda_m - \lambda_i)} \tag{5}$$

$$(\frac{\varphi_m}{\lambda_m} + \frac{\varphi_i}{\lambda_i})^{-1} < \lambda_{eff} < \lambda_m \varphi_m + \lambda_i \varphi_i \tag{6}$$

In all results repored below, we set λ_m=1.40 W/(m.K) for the matrix phase, and λ_i=0.0257 W/(m.K) for the porous phase, respectivelly. Each sample is characterized by its spatial arrangement (cubic or hexagonal) and surfactant type (P123, Brij76 , P123 and KLE) used in production of the material. The results shown in Fig.1 confirm that all measured

conductivities all located in the region defined by both bounds, therefore the measured data are consistent with the basic constraints of micromechanics.

Subsequently, the Mori-Tanaka and Self-consistent methods were used to theoretically predict the measured values. As evident from Table 1, a significant discrepancy between the model predictions and the measured values are found. This indicates that the need for incorporating another factor influencing the effective thermal conductivity.

Tab. 1. Results of the Mori-Tanaka and Self-consistent methods

#	Sample type [-]	Porosity [%]	Pore diameter d [nm]	Exp. value [W/(mK)]	M-T [W/(mK)]	S-C [W/(mK)]	M-T with Kapitza res. [W/(mK)]	Kapitza res. for M-T [W/(m^{2}K)]	S-C with Kapitza res. [W/(mK)]	Kapitza res. for S-C [W/(m^{2}K)]
1	P123 hex	46	8.5	0.18	0.540	0.252	0.164	-1.632e+06	0.159	3.291e+04
2	P123 hex	48	8.5	0.18	0.514	0.219	0.135	-1.632e+06	0.119	3.291e+04
3	P123 hex	40	8.5	0.22	0.621	0.372	0.260	-1.632e+06	0.304	3.291e+04
4	P123 hex	43	8.5	0.20	0.580	0.309	0.211	-1.632e+06	0.228	3.291e+04
5	P123 hex	45	8.5	0.18	0.553	0.270	0.180	-1.632e+06	0.181	3.291e+04
6	Brij76 cub	21	4.0	0.30	1.011	0.973	0.367	-6.888e+06	0.671	-3.227e+06
7	Brij76 cub	23	4.0	0.29	0.977	0.932	0.294	-6.888e+06	0.484	-3.227e+06
8	Brij76 cub	23	4.0	0.34	0.977	0.932	0.294	-6.888e+06	0.484	-3.227e+06
9	P123 cub	29	9.0	0.28	0.881	0.812	0.170	-2.953e+06	0.328	-1.076e+06
10	P123 cub	23	9.0	0.38	0.977	0.932	0.361	-2.953e+06	0.541	-1.076e+06
11	P123 cub	26	9.0	0.27	0.929	0.872	0.263	-2.953e+06	0.431	-1.076e+06
12	P123 cub	25	9.0	0.27	0.945	0.892	0.295	-2.953e+06	0.467	-1.076e+06
13	KLE cub	27	16.5	0.35	0.912	0.852	0.353	-1.489e+06	0.506	-5.571e+05
14	KLE cub	30	16.5	0.32	0.865	0.791	0.268	-1.489e+06	0.413	-5.571e+05

4. IMPROVED MODELS

The most direct possibility is to account for the presence of interfacial thermal barrier, known as the Kapitza resistance. This class of models was presented e.g. [1], and is based on a simple modification of the original scheme by replacing the inclusion conductivity by its apparent value

$$\lambda_{i,d} = \lambda_i \frac{dh}{dh + 2\lambda_i} \tag{7}$$

where where $\lambda_{i,d}$ stands for modified inclusion thermal conductivity, d denotes diameter of inclusion and h stands for value of Kapitza resistance.

In the current case, all data except for the value of the Kapitza resistance are known, therefore its optimal value can be directly computed for each sample. It was found that data can be categorized into four groups, according to the spatial arrangement of pores and the

surfactant type used in sample preparation. Thus, a single value of Kapitza resistance was determined for each group by minimizing the error function expressed as

$$\sum_{i=1}^{N} \frac{(\lambda_{\exp}{}^{i} - \lambda_{calc}{}^{i})^2}{(\sigma^i)^2} \tag{8}$$

where σ^i denotes the standard deviation of experimental mesurements [2]. For the S-C scheme, this was complemented with an additional constraint necessary to ensure that the resulting conductivity remains a real number. The resulting values are presented in Tab. 1. It is worth noting that for almost all samples, the value of the Kapitza resistance is negative (except P123 hex for the S-C method). This is rather surprising result, which deserves further investigation. Nevertheless, the negative values of h in nanofluids were found in [6] using molecular simulations. These results are further supported with data in Tab. 2, confirming a significant decrease in the objective function (8), and by Fig. 2, showing a reasonable match

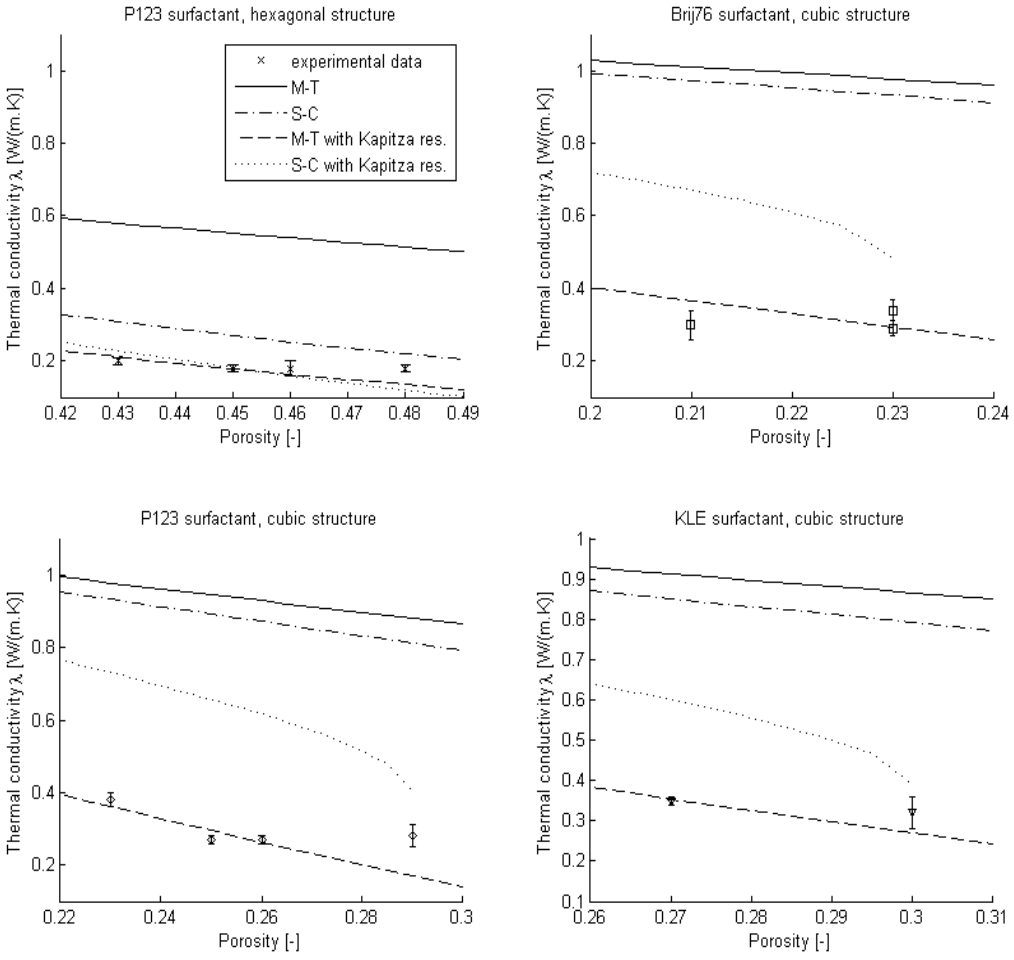

Fig.2: Comparison of calculated and measured values

namely between M-T predictions and experimental data.

Tab. 2. Error function values

	P123 hexagonal	Brij76 cubic	P123 cubic	KLE cubic	Sum
M-T	5878.29	1948.70	10181.95	3349.73	21358.68
S-C	458.88	1704.09	8566.53	2655.76	13385.26
M-T with Kapitza res.	38.02	5.16	21.07	1.78	66.03
S-C with Kapitza res.	116.34	204.00	3013.88	624.73	3958.94

5. CONCLUSION

In this paper, the effective media theories, represented by Mori-Tanaka method and Self-Consistent method, were employed to predict effective thermal conductivity of nanoporous thin films. Our findings can be summarized as follows:

1. Without the interfacial resistance factor, neither Mori-Tanaka nor Self-Consistent method are suitable for predicting the effective thermal conductivity of nanopourous materials.
2. It is possible to reach fairly good prediction, especially for Mori-Tanaka method, when accounting for the Kapitza resistance. However, results of the inverse analysis suggest that the value is negative.

In a near future, we plan to complement these results with detailed finite element simulations.

ACKNOWLEDGEMENT

This work was supported by the Czech Science Foundation, project No. P105/11/0411 and by the Czech Technical University in Prague, project No. SGS11/021/OHK1/1T/11.

REFERENCES

[1] J. Stránský: Mikromechanické modely pro tepelnou vodivost v kompozitních materiálech s nedokonalým spojením složek, bachelor thesis, ČVUT v Praze, 2009

[2] T. Coquil, E. K. Richman, N. J. Hutchinson, S. H. Tolbert, and L. Pilon: Thermal conductivity of cubic and hexagonal mesoporous silica thin films, Journal Of Applied Physics 106, 034910 2009

[3] S.Torquato: Random Heterogeneous Materials, corrected edition (October 19,2001), Springer, 2001, 728pages, ISBN-10: 0387951679

[4] M. E. Davis: Ordered porous materials for emerging applications, Nature 417, 2002, 813-821

[5] S.-M. Lee, D. G. Cahill: Heat transport in thin dielectric films, Journal of Applied Physics, Volume 81, Issue 6, March 15, 1997, pp.2590-2595

[6] J. Eapen, J. Li, S. Yip: Beyond the Maxwell limit: Thermal conduction in nanofluids with percolating fluid structures, 2007, Physical Review E 76, 062501

MICRO AND MACRO PROPERTIES OF BAMBOO REINFORCEMENT

ANDREA HÁJKOVÁ[1], HANA NĚMCOVÁ [2], TOMÁŠ PLACHÝ[3]
PAVEL TESÁREK [4], VLASTIMIL KRÁLÍK [5]

Abstract: *Bamboo is very important, cheap and high quality construction element. For several centuries, it is commonly used in subtropical and tropical countries as auxiliary structures, as well as a supporting element. Normally it is possible to meet with bamboo scaffolding, roofs and other structures. Based on current utilization of bamboo in Asia there is an opportunity to use bamboo as a structural element in our country too, e.g. as a reinforcement, which can replace the steel reinforcement in some cases. If we would like to use bamboo as a structural material in our geographical conditions, it is necessary to define its mechanical properties and its behavior in our climate.*

Keywords: *bamboo, mechanical properties, nanoindentation, reinforcement, steel*

1. INTRODUCTION

Thanks to its properties, which are given by its unique composite structure, bamboo is not only in Asia one of the basic building materials. His woody fibers contain cellulose and lignin, but also silicates (silicate content is dependent on environmental conditions during growth). They are stored mainly in sklerenchymatic cells and deliver its high hardness of

[1] Ing. Andrea Hájková; Czech Technical University in Prague, Faculty of Civil Engineering, Department of Mechanics; Thákurova 7, 166 29 Prague 6 - Dejvice, Czech Republic, andrea.hajkova@fsv.cvut.cz

[2] Ing. Hana Němcová; Czech Technical University in Prague, Faculty of Civil Engineering, Department of Mechanics; Thákurova 7, 166 29 Prague 6 - Dejvice, Czech Republic, hana.nemcova@fsv.cvut.cz

[3] Ing. Tomáš Plachý, Ph.D.; Czech Technical University in Prague, Faculty of Civil Engineering, Department of Mechanics; Thákurova 7, 166 29 Prague 6 - Dejvice, Czech Republic, plachy@fsv.cvut.cz

[4] Ing. Pavel Tesárek, Ph.D.; Czech Technical University in Prague, Faculty of Civil Engineering, Department of Mechanics; Thákurova 7, 166 29 Prague 6 - Dejvice, Czech Republic, tesarek@fsv.cvut.cz

[5] Ing. Vlastimil Králík; Czech Technical University in Prague, Faculty of Civil Engineering, Department of Mechanics; Thákurova 7, 166 29 Prague 6 - Dejvice, Czech Republic, vlastimil.kralik@fsv.cvut.cz

bamboo. High hardness and strength of the bamboo allows its use for fittings in concrete instead of steel, replacing the heavy steel scaffolding, etc. [1].

Bamboo is an excellent building material. It is round, light, and hollow and divided by partitions, it is also waterproof and can withstand significant stress. With unique features, durability, ease of availability and recoverability, the bamboo seems to be the ideal natural material that satisfies both technical requirements as well as environmental and economic aspects [2].

Today, bamboo is a popular material not only in civil engineering and architecture but also in many other sectors. However, the widest application is still being found in construction, where steel is replaced by bamboo in the form of reinforcement (Figure 1). Figures 1 shows that, for example in Asia the usage of whole or cut stalks of bamboo as a reinforcement is quite common, especially in combination with poured concrete or raw bricks, clay, etc.

Fig. 1. Bamboo reinforcement of outer walls (http://www.aplaceofsense.com) - left. Bamboo flooring reinforcement (http://www.buildinginasia.com) - right

The overall mechanical properties of materials at the macro level are directly proportional to the overall properties of the material at the micro level. If it is a homogeneous material as steel, then the characteristics of both the macro and micro levels are almost identical. In contrast, variability of material properties of heterogeneous building materials – especially on natural base (wood, bamboo) is wide. Each micro-mechanical property – for example bending strength – depends on the type of used material. The nanoindentaion is a suitable method for verification of micro-mechanical properties and macro-mechanical properties using homogenization, which reflects the approximate strength values for different phases of the

material at the micro level, respectively nanoindentation is an instrument for determination of dependence between micro and macro mechanical properties as a function of micro and macrostructure and microstructural mechanical properties in different phases of the material. For the purpose of dependence between the mechanical properties at the macro and micro level, a typical natural building material – bamboo (Phyllostachys sp. – also known as yellow bamboo) – was chosen.

2. STRUCTURE AND GENERAL PROPERTIES OF BAMBOO

Bamboo is a very old plant, which in many countries for many centuries is used thanks to its excellent properties. Bamboo is essentially a timber that is classic but from woody stems it is different in growth, structure and chemical composition.

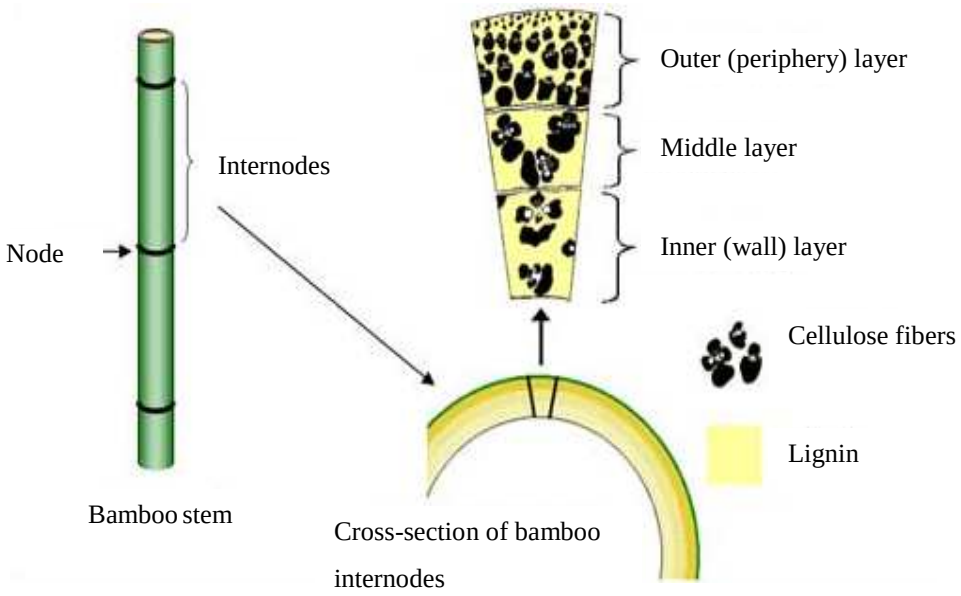

Fig.2. Anatomical features of bamboo internodes [4]

Bamboo stem is a composite material, as it can be seen from testing of its micro mechanical properties. From a macroscopic view of the cross-section, the bamboo consists of several components (Figure 2). Based on these parameters the strength characteristics of the stems were tested. The three-point bending test was chosen for determination of basic strength characteristics of bamboo. The test results are shown in Table 1 [3].

Tab. 1. Three-point bending test results [3]

Properties	Internodes	Stem with nodes
n [-]	15	20
σ_p [MPa]	204.0	214.0
E [GPa]	11.0	11.4

Table 1 shows the values mechanical characteristics along the length of bamboo stalks. In cross section, the values of strength depend on the content of dark fiber from cellulose (Figure 3). In determining the overall strength, it is necessary to take into account the age of the plants and the ratio of fibers to the content of fillers [4].

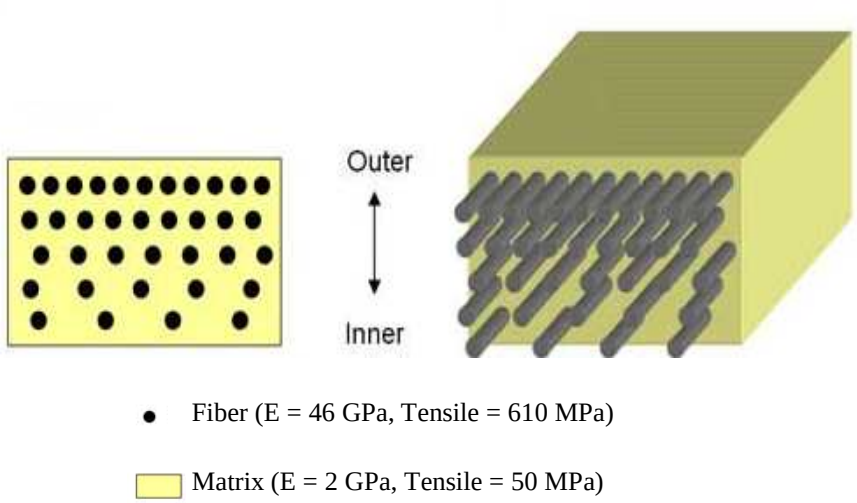

Fig.3. Bamboo strip as orthotropic unidirectional fibrous composite [4]

3. MICROMECHANICAL PROPERTIES OF BAMBOO

Figure 4 shows the structure of the stalk of bamboo under the microscope at a magnification of 200 ×. Figure 4 shows the different structure of the bamboo stalk. Globally, the structure can be divided into three main parts – denoted as a), b) and c):

a) The dark fibers of the image are largely made up phloem, xylem, cellulose 60 %, approximately 5 % silica, lignin (used for the transport of vitamins, hormones, water, etc.),

b) Clear dark filaments inside a clump of fibers are formed predominantly from silica 0.2 %, xylem and cellulose (used primarily to transport minerals),

c) Ground filling fiber among clumps of dark fibers are made of lignin, phloem, metaxylem vessel (matrix) [2].

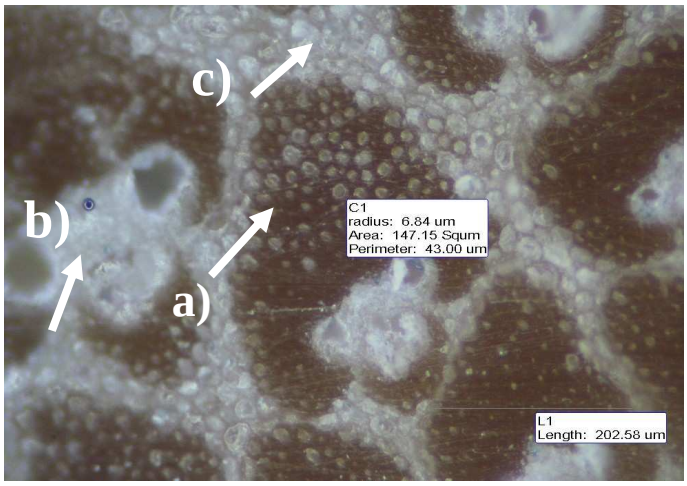

Fig. 4. Typical cut bamboo stalk at 200 × magnification

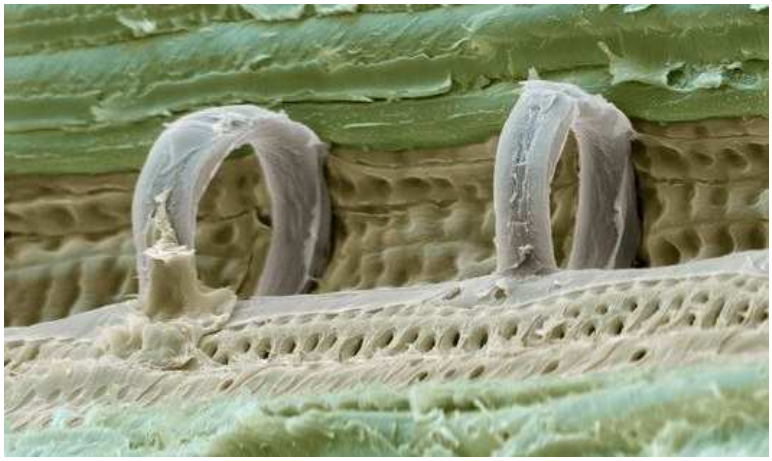

Fig. 5. Colored scanning electron micrograph (SEM) of a section through a xylem vessel in a bamboo stem with magnification 1150 × (http://www.sciencephoto.com)

Before testing of micro-mechanical properties using nanoindentation, it is necessary to remember that bamboo is highly porous. In essence, the whole strength of the stem is formed only after drying walls of hollow fibers consisting of different structures. Dark fibers are considered for the strongest walls (Figure 4), which are reinforced even by small grey loops of lignin – Figure 5 [5].

4. MICRO MECHANICAL PROPERTIES OF BAMBOO STEM

The basic elastic properties were measured by device Hysitron TriboIndenter® using in-situ SPM imaging mode, maximal force was 10 mN and the fluid Berkovich tip was used for testing. A sample bamboo stem was sealed in a resin from Struers, cut and polished. Figure 6 describes (in-situ SPM imaging mode) the measured area of the tested sample (matrix × inclusion). The bamboo material is porous with high irregular porosity and with several phases of different composition.

The sample was sanded using several technological processes, which closely matches our application. The only criterion was the alignment of the sample and the surface roughness. Struers grinding on the grinding machine was used for preparing of the samples:

1) SiC 2000, 5 min., 100 rpm., underwater, pressure 10 to 15 N
2) SiC 4000, 5 min., 100 rpm., underwater, pressure 10 to 15 N

Preparation of the sample surface quality is essential if we want to use Oliver-Pharr theory for nanoindentation [6]. Due to the achieved indentation depths of 800 nm, the roughness of 50 nm is optimal. The average values of sample surface roughness are Rq ~ 27 nm and Ra ~ 22 nm. Roughness was measured by SPM imaging. A contact force between the tip and the surface was in our case 2 μN. Size of scanned area was 50 x 50 μm.

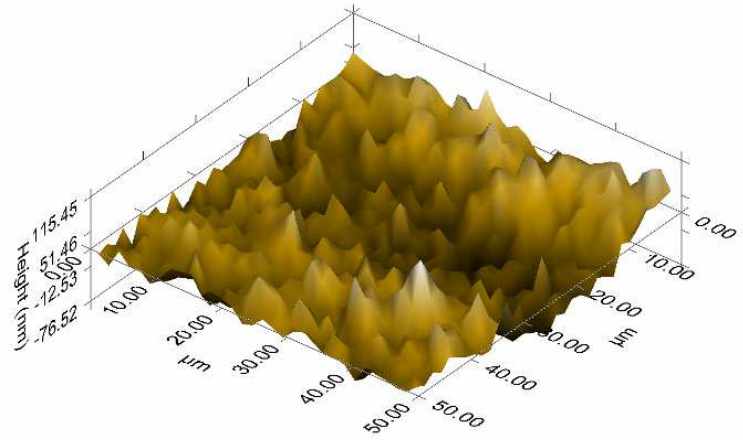

Fig. 6. 3D fence of the scan the sample surface TF (50 × 50 micron)

In our case only one sample was tested. Three positions were selected on the surface of the sample. In these positions, the 4x4 matrix of indents were made. Indents were spaced 20 μm. Average values of selected parameters as contact depth, reduced elastic modulus and hardness are given in Table 2 for each position.

Tab. 2. Comparison of elastic mechanical properties for 3 positions

Force	Position	Contact depth	stdev	Reduced elastic modulus	stdev	Hardness	stdev
[μN]	nr.	[nm]		[GPa]		[GPa]	
3000	1	**763.2**	41.2	**5.5**	0.24	**0.182**	0.019
	2	**736.3**	38.8	**5.2**	0.24	**0.194**	0.019
	3	**748.6**	42.3	**5.9**	0.42	**0.189**	0.020

5. CONCLUSION

At first it will be necessary to separate the individual components of bamboo when determining its microscopic properties. In the future work the bamboo will be subjected to closer investigation and measurement of its components from the view of physical and chemical behavior. It can be said that bamboo as a natural material with an unusually high strength is a very suitable building material with the possibility of wider use.

ACKNOWLEDGEMENT

This work has been supported by grant CTU under No. SGS10/136/OHK1/2T/11, Advanced experimental methods.

REFERENCES

[1] Yu, W. K., Chung, K., F., Chans, S., L., 2003: *Column buckling of structural bamboo*. Engineering Structures 25. pp. 755–768. ISSN 0141-0296.

[2] Cung, K., F., Yu, W., K., 2002: *Mechanical properties of structural bamboo for bamboo Scaff oldings*. Engineering Structures 24. pp. 429–442. ISSN 0141-0296.

[3] Sebera, V., Tippner, J., Horacek, P., Dejmal, A., Beniček, M., 2010: *Finite element model of bamboo culm (Phyllostachys sp.) and its comparison to two experimental tests*. Acta Universitatis Agriculture et Silviculturae Mendellianae Brunensis, LVIII, No. 1, pp. 153–160.

[4] Nirman, L., 2010. *Bamboo Structural Material*, [online], [cit. 2011-08-03], <www.assambambooworld.com/bamboo-structural-material.htm>.

[5] Schneidereit, S. 2002: *Bamboo as a building material*, [online], [cit. 2011-18-08], <http://www.koolbamboo.com>.

[6] Tesárek, P., Němeček, J. (2011): Microstructural and micromechanical study of gypsum, Chem. Listy 102, pp. 852- 853. ISSN 1213-7103.

MODELING OF CONCRETE CREEP BASED ON MICROPRESTRESS-SOLIDIFICATION THEORY

PETR HAVLÁSEK[1], MILAN JIRÁSEK[2]

Abstract: *A realistic description of concrete creep can be achieved by advanced models, such as model B3 and its improved version that uses the concept of microprestress. In this paper, values of parameters used by the microprestress-solidification theory (MPS) are recommended and their influence on the creep compliance function is evaluated and checked against experimental data from the literature. Certain deficiencies of MPS are pointed out and its modified version is proposed.*

Keywords: *creep, concrete, microprestress, solidification, finite elements*

1. INTRODUCTION

In contrast to metals, concrete exhibits creep already at room temperature. This phenomenon results into a gradual but considerable increase of deformation at sustained loads and needs to be taken into account in design and analysis of concrete structures. The present paper examines an advanced concrete creep model, which extends the original B3 model [5] and uses the concepts of solidification [9], [10] and microprestress [6]-[8]. The main objective of the paper is to clarify the role of non-traditional model parameters and provide hints on their identification. The creep tests performed by Fahmi, Polivka and Bresler [1], covering creep of both sealed and drying specimens under elevated and variable temperatures, are used as a source of experimental data and are compared with the results of numerical simulations.

All numerical computations have been performed using the finite element package OOFEM [2]-[4] developed mainly at the CTU in Prague by Bořek Patzák.

[1] Ing. Petr Havlásek; Department of Mechanics, Faculty of Civil Engineering, Czech Technical University in Prague; Thákurova 7, 166 29, Prague 6, Czech Republic; petr.havlasek@fsv.cvut.cz

[2] Prof. Ing. Milan Jirásek, DrSc.; Department of Mechanics, Faculty of Civil Engineering, Czech Technical University in Prague; Thákurova 7, 166 29, Prague 6, Czech Republic; milan.jirasek@fsv.cvut.cz

2. DESCRIPTION OF THE MATERIAL MODEL

The complete constitutive model for creep and shrinkage of concrete can be represented by the rheological scheme shown in Fig. 1. It consists of (i) a non-aging elastic spring, representing instantaneous elastic deformation, (ii) a solidifying Kelvin chain, representing short-term creep, (iii) an aging dashpot with viscosity dependent on the microprestress, *S*, representing long-term creep, (iv) a shrinkage unit, representing volume changes due to drying, and (v) a unit representing thermal expansion. In the experiments, shrinkage and thermal strains were measured separately on load-free specimens and subtracted from the strain of the loaded specimen under the same environmental conditions. It should be noted that even after subtraction of shrinkage and thermal strain, the evolution of mechanical strain is affected by humidity and temperature. Dry concrete creeps less than wet one, but the process of drying accelerates creep. Higher temperature leads to faster cement hydration and thus to faster reduction of compliance due to aging, but it also accelerates the viscous processes that are at the origin of creep and the process of microprestress relaxation.

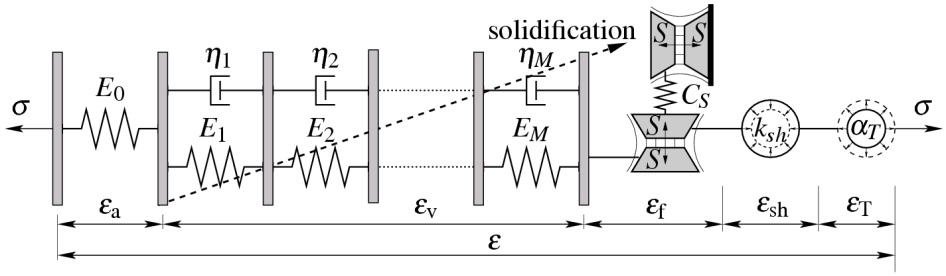

Fig. 1. Rheological scheme of the complete hygro-thermo-mechanical model.

The microprestress is understood as the stress in the microstructure generated due to large localized volume changes during the hydration process. It builds up at very early stages of microstructure formation and then is gradually reduced by relaxation processes. Additional microprestress is generated by changes of internal relative humidity and temperature. This is described by the non-linear differential equation

$$\frac{dS}{dt} + \psi_S(T,h)c_0 S^2 = k_1 \left| \frac{d(T \ln h)}{dt} \right| \tag{1}$$

in which *T* denotes the absolute temperature, *h* is the relative pore humidity (partial pressure of water vapor divided by the saturation pressure), c_0 and k_1 are constant parameters, and ψ_S is a variable factor that reflects the acceleration of microprestress relaxation at higher temperature and its deceleration at lower humidity (compared to the standard conditions). Owing to the presence of the absolute value operator on the right-hand side of (1), additional

microprestress is generated by both drying and wetting, and by both heating and cooling, as suggested in [8].

The dependence of factor ψ_S on temperature and humidity is assumed in the form

$$\psi_S(T,h) = exp\left[\frac{Q_s}{R}\left(\frac{1}{T_0}-\frac{1}{T}\right)\right]\cdot\left[\alpha_S+(1-\alpha_S)h^2\right] \qquad (2)$$

where Q_S is the activation energy, R is the Boltzmann constant, T_0 is the reference temperature (room temperature) in absolute scale and α_S is a parameter. The default parameter values recommended in [8] are Q_S/R = 3000 K and $\alpha_S \approx 0.1$. More detailed description of this material model can be found in the original papers [6]-[8] or in [11].

3. NUMERICAL SIMULATIONS

In this section, experimental data of Fahmi, Polivka and Bresler are compared to results obtained with the MPS theory, which reduces to the standard B3 model in the special case of basic creep. All examples concerning drying and thermally induced creep have been run as a staggered problem, with the heat and moisture transport analyses preceding the mechanical one. The available experimental data contained the mechanical strains (due to elasticity and creep), with the thermal and shrinkage strains subtracted.

In these experiments, all specimens had a shape of a hollow cylinder with inner diameter 12.7 cm, outer diameter 15.24 cm and height 101.6 cm. The weight ratio of the components of the concrete mixture was water : cement : aggregates = 0.58 : 1 : 2. From that we can estimate that the concrete mixture contained approximately 520 kg of cement per cubic meter. The average 21-day compressive strength was 40.3 MPa. Using CEB-FIP recommendations, the 28-day strength can be estimated as 42.2 MPa. The experiment was performed for four different histories of loading, temperature and relative humidity. The loading program of the first two is summarized in Table 1, the other two loading programs with cyclic thermal loading are specified in Table 2.

Table 1. Testing program with one temperature cycle

	Data set 1						Data set 2					
Time duration [day]	21	37	26	82	10	25	18	14	37	108	10	25
Temperature [°C]	23	23	47	60	23	23	23	23	23	60	23	23
Relative humidity [%]	100	98	98	98	98	98	100	50	50	50	50	50
Compressive stress [MPa]	0	6.27	6.27	6.27	6.27	0	0	0	6.27	6.27	6.27	0

Table 2. Testing programs with several temperature cycles and sealed conditions, i.e. RH = 98% (data set 3) or drying conditions (data set 4)

							repeat 4x				
data set 3	Time duration [day]	21	35	9	5	14	7	7	7	12	40
	Temperature [°C]	23	23	40	60	23	60	23	60	23	23
	Compressive stress [MPa]	0	6.27	6.27	6.27	6.27	6.27	6.27	6.27	6.27	0
data set 4	Time duration [day]	18	14	33	15	14	7	7	7	13	14
	Temperature [°C]	23	23	23	60	23	60	23	60	23	23
	Relative humidity [%]	100	50	50	50	50	50	50	50	50	50
	Compressive stress [MPa]	0	0	6.27	6.27	6.27	6.27	6.27	6.27	6.27	0

3.1 Standard MPS

The four parameters of the B3 model describing the basic creep, $q_1 - q_4$, were determined from the composition of the concrete mixture and from the compressive strength using empirical formulae according to [5]. The result of this prediction exceeded the expectations; only minor adjustments were necessary to get the optimal fit (see the first part of the strain evolution in Fig. 2 left). The following values were used: q_1 = 19.5, q_2 = 160, q_3 = 5.25 and q_4 = 12.5 (all in 10^{-6}/MPa). They differ significantly from the values recommended in [8], q_1 = 25, q_2 = 100, q_3 = 1.5 and q_4 = 6, which do not give a satisfactory agreement with experimental data.

The MPS theory uses three additional parameters, c_0, k_1 and c, but parameter c can be replaced by $c_0 q_4$. It has been found that the remaining parameters c_0 and k_1 are not independent. What matters for creep is only their product. For different combinations of c_0 and k_1 giving the same product, the evolution of microprestress is different but the evolution of creep strain is exactly the same. Since microprestress is not directly measurable, c_0 and k_1 cannot (and need not) be determined separately. In practical computations, k_1 can be set to a fixed value (eg. 1 Mpa/K), and c_0 can be varied until the best fit with experimental data is obtained; in all the following figures c_0 is specified in $\text{Mpa}^{-1}\text{day}^{-1}$. All other parameters were used according to standard recommendations.

A really good fit of the first experimental data set (98% relative humidity, i.e., h=0.98) was obtained for c_0 = 0.235 $\text{Mpa}^{-1}\text{day}^{-1}$; see Fig. 2 left. The agreement is satisfactory except for the last interval, which corresponds to unloading. It is worth noting that the thermally induced part of creep accounts for more than a half of the total creep (compare the black and gray solid curves in Fig. 2 left). Unfortunately, with default values of the other parameters, the same value of c_0 could not be used to fit experimental data set number 2, because it would have led to overprediction of creep (see the gray dashed curve in Fig. 2 right). In the first loading

interval of 37 days, creep takes place at room temperature and the best agreement would be obtained with parameter c_0 set to 0.940 $Mpa^{-1}day^{-1}$; see the black dashed curve in Fig. 2 right. However, at the later stage when the temperature rises to 60°C, the creep would be grossly overpredicted. A reasonable agreement during this stage of loading is obtained with c_0 reduced to 0.067 $Mpa^{-1}day^{-1}$ (dotted curve in Fig. 2 right), but then the creep is underpredicted in the first interval in Fig. 2 left. Raising parameter α_S from its recommended value 0.1 to 0.3 (solid black curve in Fig. 2 right) has approximately the same effect as decreasing c_0 from 0.235 to 0.067 $Mpa^{-1}day^{-1}$. Parameter α_S controls the effect of reduced humidity on the rate of microprestress relaxation and its modification has no effect on the response of sealed specimens.

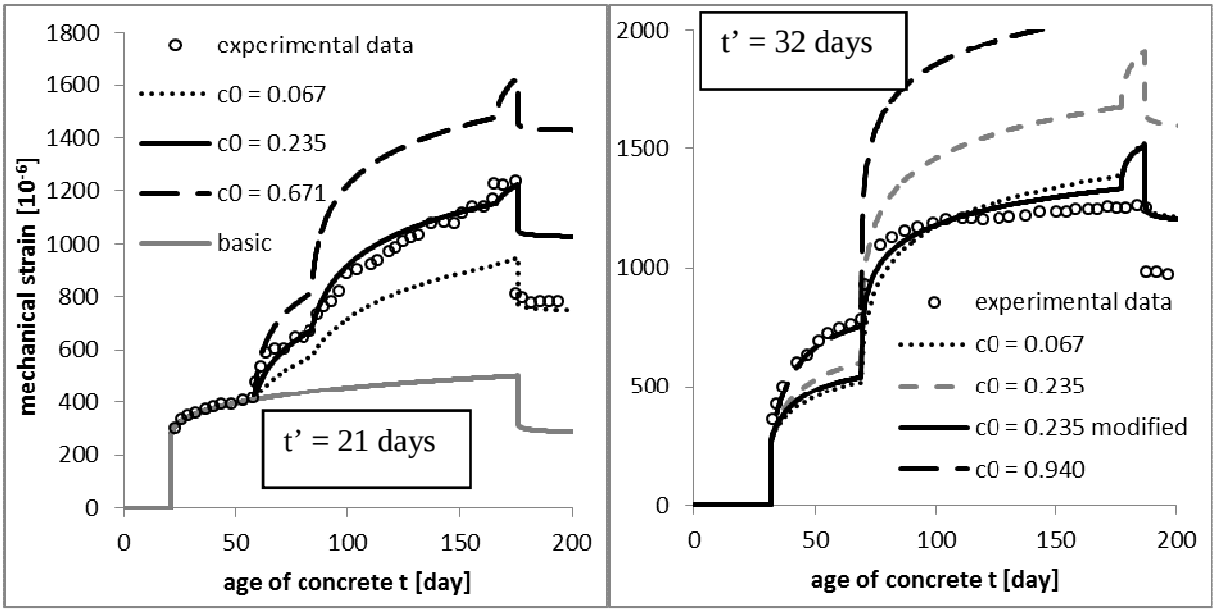

Fig. 2. Mechanical strain evolution for sealed specimens, i.e. relative humidity of pores is assumed to be 98% (left) and drying specimens at 50% relative environmental humidity (right) loaded by compressive stress 6.27 Mpa at time t'.

For the last two testing programs described in Table 2, the agreement between experimental and computed data is reasonable only until the end of the second heating cycle (solid curves in Fig. 3). In case of *data set 3*, the final predicted compliance exceeds the measured value almost twice (Fig. 3 left), in case of *data set 4* almost five times (Fig. 3 right). In order to obtain a better agreement, parameter c_0 would have to be reduced, but this would result into an underprediction of creep in the first two testing programs. Experimental data show that temperature cycles significantly increase creep only in the first cycle; during subsequent thermal cycling their effect on creep diminishes. Therefore it could be beneficial to enhance the material model by adding internal memory, which would improve the behavior

under cyclic thermal loading, while the response to sustained loading would remain unchanged.

Another deficiency of the model is illustrated by the graphs in Fig. 4. They refer to the first set of experiments. As documented by the solid curve in Fig. 2 left, a good fit was obtained by setting parameter c_0 = 0.235 Mpa^{-1}day^{-1}, assuming that the relative pore humidity is 98%. The pores are initially completely filled with water; however, even if the specimen is perfectly sealed, the relative humidity slightly decreases due to the water deficiency caused by the hydration reaction. This phenomenon is referred to as self-desiccation.

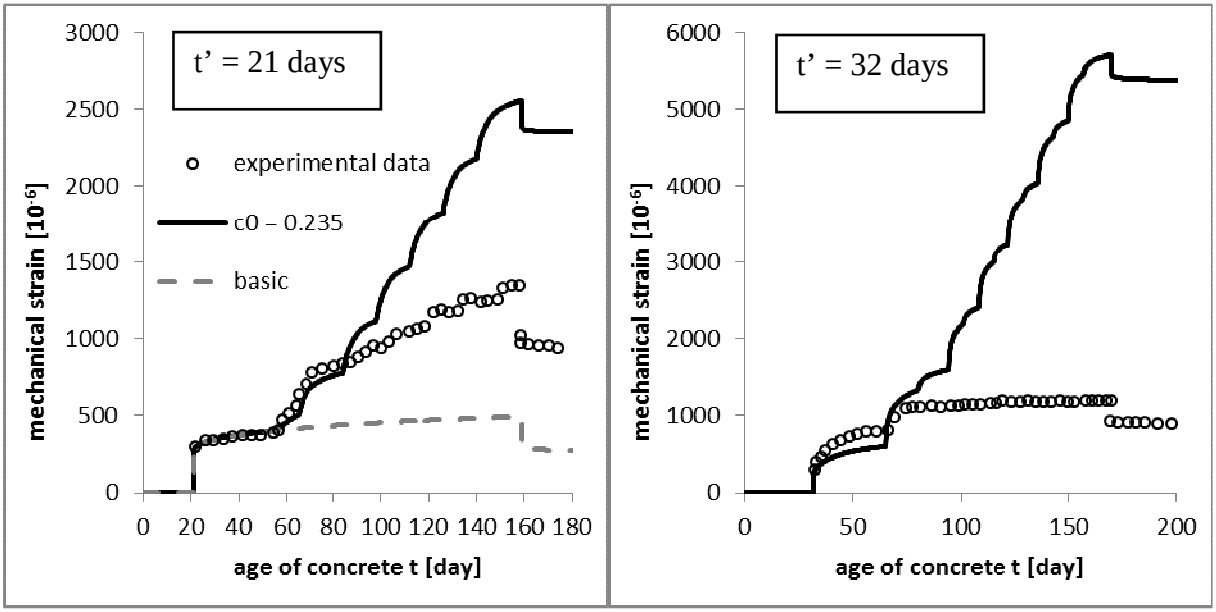

Fig. 3. Mechanical strain evolution for sealed specimen (left) and for specimen subjected to drying at the age of 18 days (right) loaded by stress 6.27 Mpa at time t' and subjected to cyclic variations of temperature.

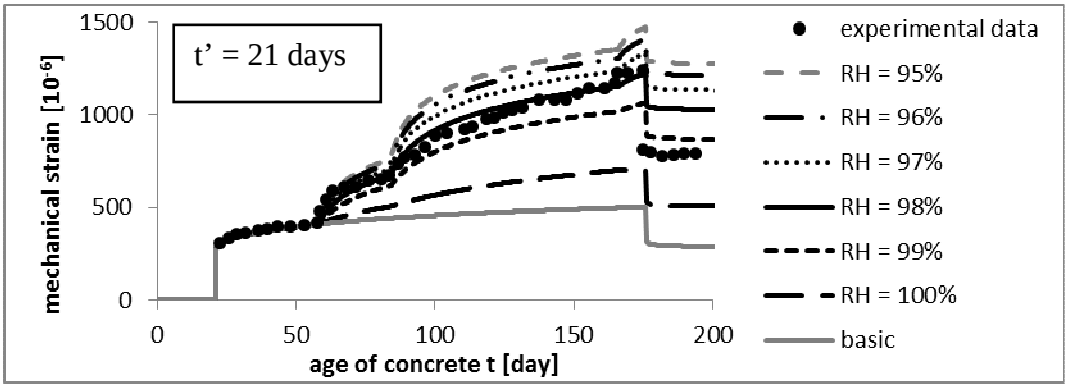

Fig. 4. Mechanical strain evolution for sealed specimens loaded by compressive stress 6.27 Mpa from age 21 days, with the assumed relative humidity of pores varied from 95% to 100%. Parameters of MPS theory: k_1 = 1 Mpa/K, c_0 = 0.235 Mpa^{-1}day^{-1}.

The problem is that the exact value of pore humidity in a sealed specimen and its evolution in time are difficult to determine. In simple engineering calculations, a constant value of 98%

is often used. Unfortunately, the model response is quite sensitive to this choice, and the creep curves obtained with other assumed values of pore humidity in the range from 95% to 100% would be different; see Fig. 4. The source of such a strong sensitivity is in the assumption that the instantaneously generated microprestress is proportional to the absolute value of the change of $T \ln(h)$; see the right-hand side of (1). Rewriting (1) as

$$\frac{dS}{dt} + \psi_S(T,h) c_0 S^2 = k_1 \left| \ln h \frac{dT}{dt} + \frac{T}{h}\frac{dh}{dt} \right| \tag{3}$$

we can see that at (almost) constant humidity close to 100%, the right-hand side is proportional to the magnitude of temperature rate, with proportionality factor $k_1|\ln h| \approx k_1(1-h)$. If the assumed humidity is changed from 99% to 98%, this proportionality factor is doubled.

3.2 Improved MPS

As a simple remedy to overcome these problems, the microprestress relaxation equation (1) is replaced by

$$\frac{dS}{dt} + \psi_S(T,h) c_0 S^2 = k_1 \left| \frac{T}{h}\frac{dh}{dt} - \kappa_T k_T \frac{dT}{dt} \right| \tag{4}$$

$$\text{with } k_T = e^{-c_T(T_{max}-T)} \tag{5}$$

in which κ_T and c_T are new parameters and T_{max} is the maximum reached temperature. With κ_T = 0.02, the creep curves in Fig. 4 plotted for different assumed pore humidities would be almost identical with the solid curve that nicely fits experimental results. Introduction of a new parameter provides more flexibility needed to improve the fit of the second testing program in Fig. 2 right, with combined effects of drying and temperature variation. For sealed specimens and monotonous thermal loading, only the product $c_0 k_1 \kappa_T$ matters, and so the good fit in Fig. 2 right could be obtained with different combinations of κ_T and c_0.

The results are shown in Fig. 5 for sustained thermal loading (data sets 1 and 2) and in Fig. 6 for cyclic thermal loading (data sets 3 and 4). Default values of parameters α_S, α_R, α_E and activation energies are used. In these charts, data series labeled original MPS show results obtained with standard MPS. Data series *kappaT = ln(0.98)* were obtained with c_0 = 0.235 MPa^{-1}day^{-1}, k_1 = 1 MPa/K, κ_T = 0.020203 and c_T = 0. Data series *kappaT adjusted* correspond to parameters c_0 = 0.235 MPa^{-1}day^{-1}, k_1 = 4 MPa/K, κ_T = 0.005051 and c_T = 0. Note that in case of constant relative humidity (Figs. 5 and 6 left) these series coincide with data series original MPS.

The best agreement with experimental data is obtained with c_0 = 0.235 MPa^{-1}day^{-1}, k_1 = 4 MPa/K, κ_T = 0.005051 and c_T = 0.3/K; these series are labeled *improved*. In Fig. 5, only a small change can be observed compared to data series *kappaT adjusted*; these differences arise when the temperature ceases to be monotonous. For the sealed specimen (Fig. 5 left), this change is detrimental, but looking at Fig. 6, this deterioration is negligible comparing to a substantial improvement in the case of cyclic thermal loading.

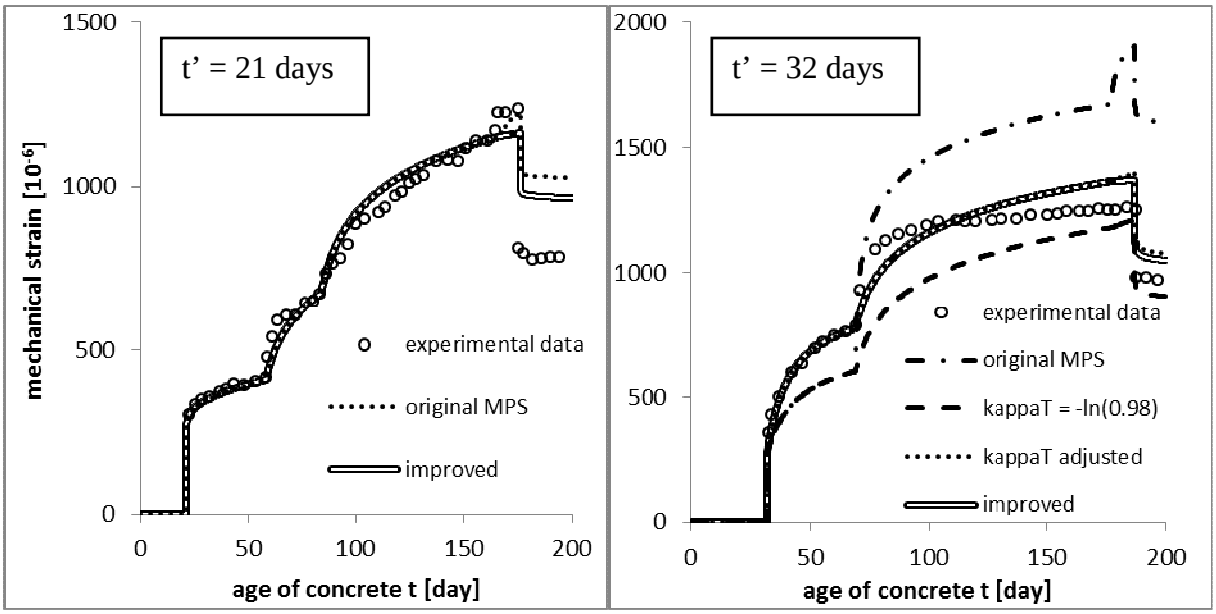

Fig. 5. Mechanical strain evolution for sealed specimens (left) and for specimens subjected to drying (right) loaded by compressive stress 6.27 MPa from age t'.

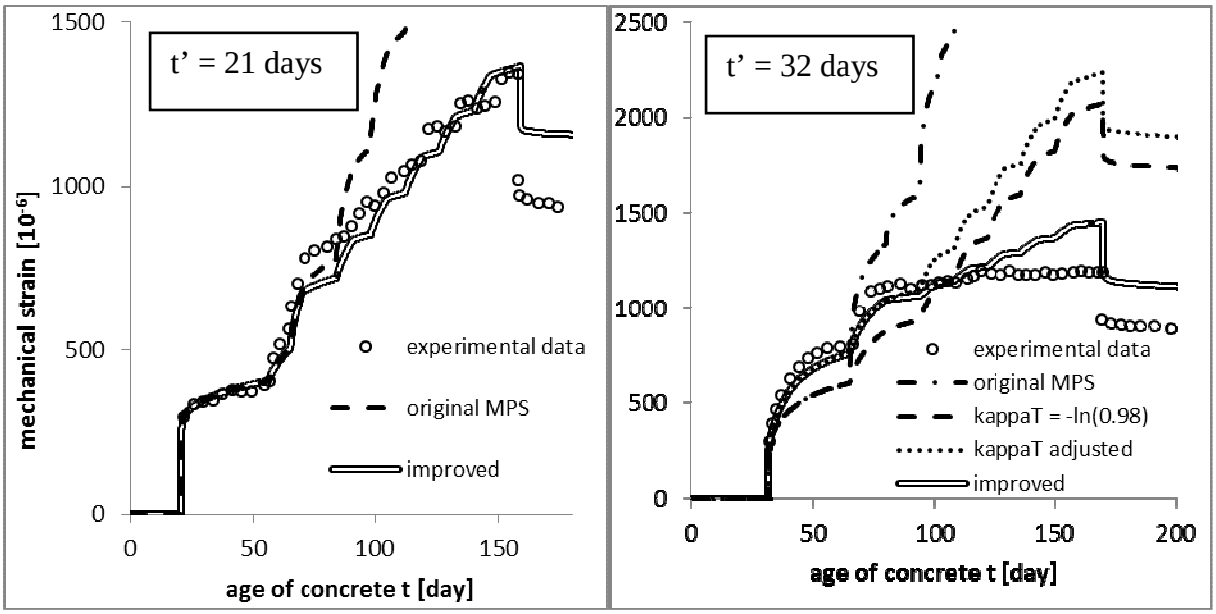

Fig. 6. Mechanical strain evolution for sealed specimens (left) and for specimens subjected to drying (right) loaded by compressive stress 6.27 MPa at time t' and subjected to cyclic variations of temperature.

4. CONCLUSIONS

The material model based on the MPS theory has been successfully implemented into the finite element package OOFEM and has been used in simulations of concrete creep at variable temperature and humidity.

For sealed specimens subjected to variable temperature, the results predicted by the MPS theory are very sensitive to the assumed value of relative pore humidity (which is slightly below 100% due to self-desiccation). In order to overcome this deficiency, a modified version of the model has been proposed and successfully validated. Excessive sensitivity to the specific choice of relative humidity has been eliminated. Also, it has become easier to calibrate the model because thermal and moisture effects on creep are partially separated.

The original model MPS theory grossly overpredicts creep when the specimen is subjected to cyclic temperature. A new variable k_T has been introduced in order to reduce the influence of subsequent thermal cycles on creep. This modification does not affect creep tests where the evolution of temperature is monotonous.

The improved MPS material model contains even more free parameters than its ancestor. To obtain a good agreement in all loading cases requires usage of automatic optimization algorithm. This will be the subject of further work.

ACKNOWLEDGEMENT

Financial support of the Czech Technical University in Prague under grants no. SGS10/020/OHK1/1T/11 and SGS11/021/OHK1/1T/11 is gratefully acknowledged.

REFERENCES

[1] Fahmi, H.M., Polivka, M. & Bresler, B., 1972. *Effects of Sustained and Cyclic Elevated Temperature on Creep of Concrete*. Cement and Concrete Research. Vol. 2, pp. 591-606.

[2] Patzák, B., 2000. *OOFEM project home page*. http://www.oofem.org

[3] Patzák, B., Bittnar, Z., 2001. *Design of object oriented finite element code*. Advances in Engineering Software, Vol. 32, Issue 10-11, pp. 759—767.

[4] Patzák, B., Rypl, D., & Bittnar, Z., 2001. *Parallel explicit finite element dynamics with nonlocal constitutive models*. Computers and Structures, Vol. 79, Issue 26-28 pp. 2287—2297.

[5] Bažant, Z.P., Baweja, S., 2000. *Creep and Shrinkage Prediction Model for Analysis and Design of Concrete Structures: Model B3*. In Adam Neville Symposium: Creep and Shrinkage – Structural Design Effects.

[6] Bažant, Z.P., Hauggaard, A.B., Baweja, S. & Ulm, F., 1997. *Microprestress-Solidification Theory for Concrete Creep. I: Aging and Drying Effects*. Journal of Engineering Mechanics, Vol. 123, No. 11, pp. 1188—194.

[7] Bažant, Z.P., Hauggaard, A.B. & Ulm, F., 1997. *Microprestress-Solidification Theory for Concrete Creep. II: Algorithm and Verification*. Journal of Engineering Mechanics, Vol. 123, No. 11, pp. 1195—1201.

[8] Bažant, Z.P., Cedolin, L. & Cusatis, G., 2004. *Temperature Effect on Concrete Creep Modeled by Microprestress-solidification Theory*. Journal of Engineering Mechanics, Vol. 130, No. 6, pp. 691—699.

[9] Bažant, Z.P., Prasannan, S., 1989. *Solidification Theory for Concrete Creep I: Formulation*, Journal of Engineering Mechanics, Vol. 115, No. 8, pp. 1691-1703 (1989)

[10] Bažant, Z.P., Prasannan, S., 1989. *Solidification Theory for Concrete Creep II: Verification and Application*, Journal of Engineering Mechanics, Vol. 115, No. 8, pp. 1704—1725.

[11] Havlásek, P., Jirásek, M., 2011. *Modeling of Concrete Creep based on Microprestress-solidification Theory*, Engineering Mechanics, submitted.

CEMENT GRAINS WITH SURFACE-SHYNTETIZED CARBON NANOFIBRES: MECHANICAL PROPERTIES AND NANOSTRUCTURE

PETR HLAVÁČEK [1], VÍT ŠMILAUER [2], PAVEL PADEVĚT [3]

Abstract: *The carbon nanotubes were synthetized directly on the surface of Portland cement particles. Mixing this new carbon/cement material with ordinary cement creates a modified cementitious substance, where carbon is perfectly dispersed in the volume.. The composites with weight fractions of carbon nanotubes/paste in the ranges 0-0.038 were prepared and mechanically tested. Slight increase in fracture energy and compressive strength was observed even in the low carbon weigh fraction 0.019.*

Keywords: *Carbon, cement, fracture energy, nanotubes*

1. INTRODUCTION

The main objective of this work is to show the mechanical properties of the cement paste/mortar reinforced with carbon nanofibres/nanotubes (CNT/CNF) directly synthetized on the cement particles. Elimination of the demanding dispersion of CNT in the volume is the main advantage of the synthesis of the CNT/CNF on the cement grains surface. Fig. 1 shows the SEM image of

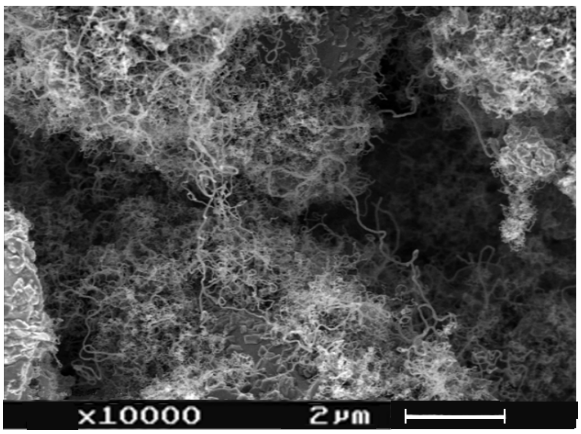

Fig 1. SEM image of the CNF synthetized directly on the cement grains surface. Overtaken from L. Nasibulina et al. [1.].

[1] Ing. Petr Hlaváček; Czech Technical University in Prague, Thákurova 7; 166 29 Praha 6, Czech Republic; petr.hlavacek@fsv.cvut.cz

[2] Doc. Ing. Vít Šmiluer, Ph.D.; Czech Technical University in Prague, Thákurova 7; 166 29 Praha 6, Czech Republic; vit.smilauer@fsv.cvut.cz

[3] Ing. Pavel Padevět, Ph.D.; Czech Technical University in Prague, Thákurova 7; 166 29 Praha 6, Czech Republic; pavel.padevet@fsv.cvut

the CHM, the Portland cement particles are completely covered with the CNF.

High performance cement composites produced in last decade exhibit high compressive strength however they have extremely brittle failure, low tensile capacity and high autogenous shrinkage [2]. Simultaneously to become more sustainable, the amount of Portland clinker in common cement has been reduced and partially replaced by secondary cementitious materials. The further reduction is possible when the strength of the binder could increase. It seems from other applications of carbon nanotubes/nanofibers [2], that the CNT/CNF reinforcement at the nanoscale presents feasible solution.

2. MATERIALS AND METHODS

2.1. CEMENT BINDER, CHM, AGGREGATES

The cement, CEM I 42.5 R originated from Mokrá, the Czech Republic, was used as the source material for all specimens. Specific Blaine surface has the value of 306 m^2/kg. The chemical composition is given in the Table 1.

The cement hybrid material (CHM) was synthesized by L. Nasibulina et al. by the chemical vapor deposition method [1]. The Portland sulfate-resistant cement (CEM I 42.5N) was used as the base for CNT/CNF growth. In the synthesis, acetylene was utilized as the main carbon source for its low decomposition temperature and affordability; CO and CO_2 presents promoting additives [1]. The CNT/CNF growth runs at temperature about 600°C in fluidized bed reactor see Fig. 2 for the scheme of the reactor [1]. The CNT typically grown on the cement particles are 30 nm in diameter and 3 μm in length [3], the specific surface area of CNT is about 10 – 20 m^2/g. CNT exhibit elastic modulus in the range of 180 - 588 GPa and tensile strength from 2 to 6 GPa [3, 4].

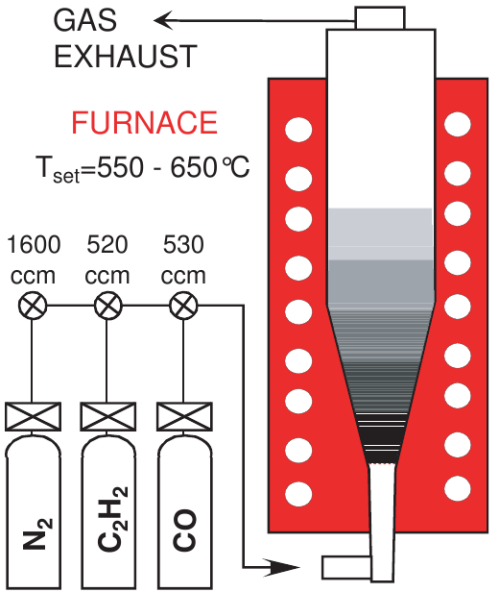

Fig 2. Scheme of the fluidized bed reactor, overtaken from L. Nasibulina et al. [1.].

Pure silica sand, fraction 0 – 2 mm was utilized in the mortar specimens. Three fractions PG1 (0 – 0.25 mm), PG2 (0.25 – 1 mm) and PG3 (1 – 2 mm) were mixed in the ratio 1:1:1.

2.2. SPECIMEN PREPARATION

Five cement paste and five mortar sets of specimens were casted. The water/binder ratio was set to 0.35 and the carbon nanotubes/paste ratio varied from 0.0 to 0.038. The CHM was intermixed with pure cement and (in case of mortar) with dry silica sand; the water with superplasticizer was added at the end. Table 1 shows the specimens composition. The hand stiring took four minutes, consecutive vibrating and form filling took extra four minutes.

After 28 days of curing under water were the specimens cutted on diamond saw; in the case of the paste specimens to nine parts (approx. 13x13x80 mm), in case of mortar to four parts (approx. 19x19x80 mm). According to RILEM standards for mechanical testing [5] nodges were cutted in the middle of the beams to the 45% of the height. The production of such small sized specimens this way is more efficient than direct casting into small molds.

Table 1: Cement paste and mortar composition; weight fractions per one sample.

Sample	**total binder weight**	**cement hybrid material**	**w/binder ratio**	**total weight of water**	**super plasticizer (63% water)**	**sand fraction 0 - 2 mm**
Paste	234 g	0 - 70.2 g	0.35	81.9 g	0.47 g	–
Mortar	75 g	0 - 22.5 g	0.35	26.25 g	0.38 g	225 g

2.3. FRACTURE ENERGY DETERMINATION

The fracture energy, G_f, was determined according to the RILEM standard [5]. See Fig. 3 for the experiment scheme. Three point displacement-controlled bending test was carried out to obtain the load-displacement curve. The work of external force P could be calculated as $W_f = \int_0^{u_i} P du$, *(1)*, where P is the external force, u is the load-point displacement and u_i presents the final displacement at which the load is equal to zero. The average (effective) fracture energy in the ligament,

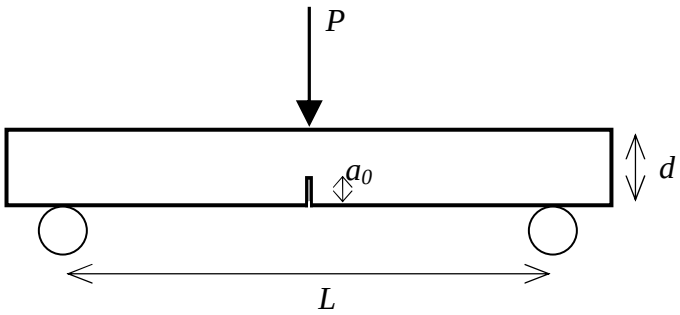

Fig 3. Scheme of the three point bending test used for the fracture energy determination

according to the RILEM standart, is defined as

$$G_f = \frac{W_f}{bl}, \quad l = h - a_0, \tag{2}$$

where l represents the length of the ligament, b the thickness of the beam, h the total height of the beam and a_0 is the depth of the nodge. The support span L was in case of mortar set to 65 mm and in case of cement paste 50 mm.

3. RESULTS AND DISCUSSION

3.1. COMPRESSIVE STRENGTH

The measurements on the paste samples have shown that replacing 3.5% cement with CHM could increase the compressive strength by 25%, in our case from average 56 MPa to average 70 MPa. However in the case of mortar samples, the effect of CHM was negative. The mortar samples with 7% replaced cement exhibit a 15% lower compressive strength, in our case decrease from average 62 MPa to average 53 MPa. See Fig. 4 for the compressive strengths of mortar and paste samples with different cement/CHM ratia.

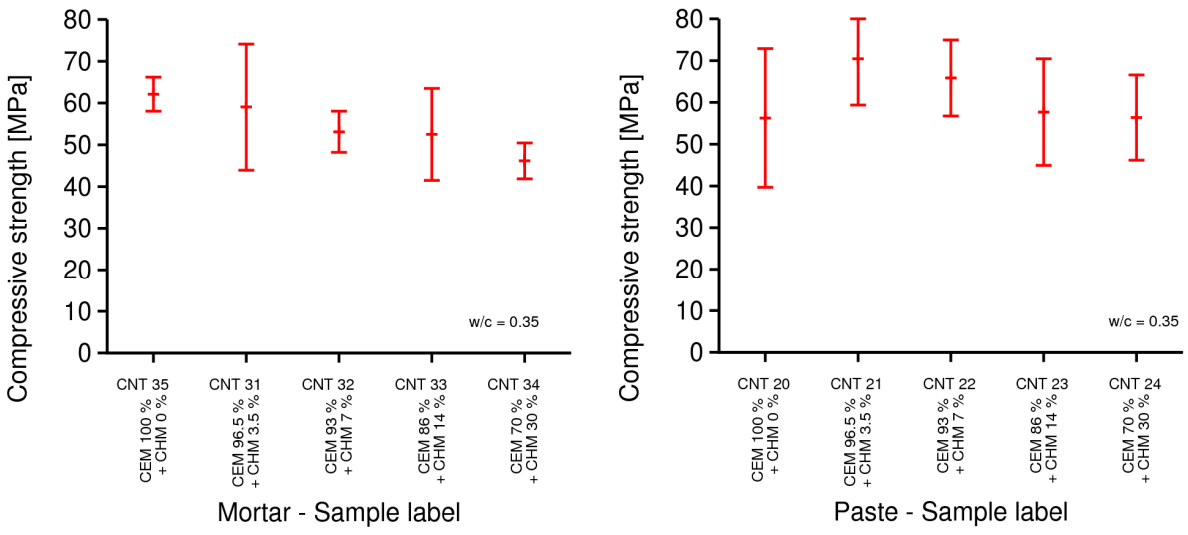

Fig 4. Compressive strength of mortar and paste samples with different cement/CHM ratio.

3.2. FRACTURE ENERGY

The fracture energy measurements results are depicted on the Fig. 5. The paste samples exhibit significant increase in the fracture energy even if a small amount of cement is replaced by CHM. Replacing 3.5% of cement causes an increase in the fracture energy of 14%. The

mortar samples does not exhibit almost any change in the fracture energy with the amount of CHM in the mixture.

3.3. HYPOTHESES

The paste samples reinforced with the carbon nanotubes exhibit the expected increase as in the compressive strength as in the fracture energy. The CNT appear as a nano-reinforcement improving the gel properties [6.]. The compressive strength maximum around 3.5% of CHM can be caused by the strong hydrophobicity of the carbon nanotubes, preventing the larger amount of CHM from hydration.

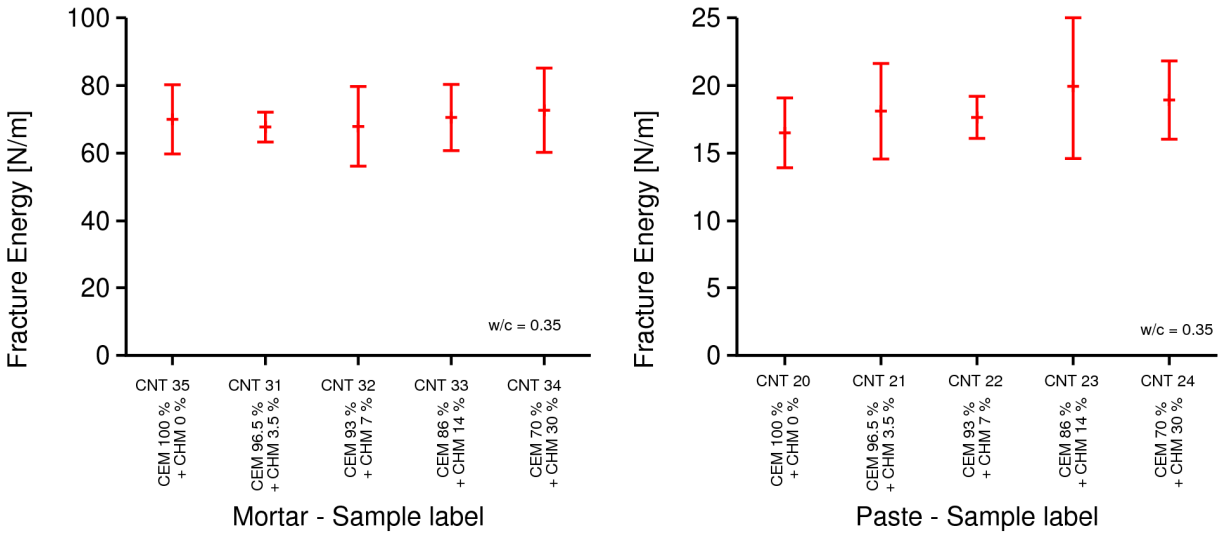

Fig 5. Fracture energy of mortar and paste samples with different cement/CHM ratio.

The decrase in the compressive strength of the mortar samples could be described by the non-homogenous gel formation. The carbon nanotubes appear as the nucleating sites [7.] for the cement hydration products (CSH gel, calcium hydroxide) and gather the cement paste. The water is pushed to the sand grains, into the interfacial transition zone (ITZ). Due to the water, the porosity in the ITZ increases and the bond with the paste matrix is getting worse.

Another explanation deals with the wekaest link theory. When the stress in the body reach the ultimate strength of the weakest member, the deformation localizes to this point and stress decreases. In case of the mortar, the fracture energy can increase (or have not to change) and the strength can be reduced.

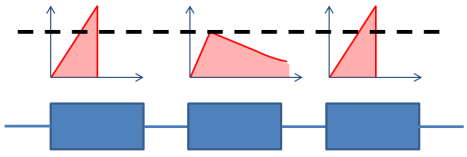

Fig 6. Weakest link theory, strength and fracture energy visualization.

4. CONCLUSION

Previous attempts to create nano-reinforced composite materials suffered from flocculation and improper dispersion of separately added nanofibers/nanotubes. The main advantage of the new method presents the elimination of the demanding CNT dispersion. The decrease of compressive strength on CNT-reinforced mortar samples could be caused by the higher amount of water in the ITZ which was pushed out by the extremely hydrophobic carbon nanotubes. Preliminary experiments with high compacted (60 MPa) mortar samples with the mixing w/c ratio 0.35 does not exhibit the compressive strength reduction. The future work will focuse on the reduction of ITZ effect incorporating the CNT into the ITZ.

ACKNOWLEDGEMENT

We gratefully acknowledge support from the Czech Technical University in Prague under grant No. SGS10/135/OHK1/2T/11.

REFERENCES

[1] Nasibulina L.et al., *Direct Synthesis of Carbon Nanofibers on Cement Particles.* Journal of the Transportation Research Board 2010, No. 2142, 96-101, doi:10.3141/2142-14.

[2] Hammel E., Tang X., Trampert M., Schmitt T., Mauthner K., Eder A., Prötschke P., *Carbon nanofibers for composite applications*. Carbon 2004; 42; 1153 –1158.

[3] la Mudimela P. et al., *Synthesis of carbon nanotubes and nanofibers on silica and cement matrix materials.* Journal of Nanomaterials 2009, doi:10.1155/2009/526128.

[4] Li G.Y., Wang P.M., Zhao X., *Mechanical behavior and microstructure of cement.* Carbon 2005, 43, 1239–1245.

[5] RILEM TCS, RILEM *Determination of the fracture energy of mortar and concrete by means of three-pointbend tests on notched beams.* Materials and Structures 1985, vol. 18, issue 106, 285-290.

[6] Raki L., Beaudoin J., Alizadeh R., Makar J., Sato T., *Cement and Concrete Nanoscience and Nanotechnology*. Materials 2010, vol. 3, 918-942; doi:10.3390/ma3020918.

[7] Makar J.M., Chan G.W., *Growth of Cement Hydration Products on Single-Walled Carbon Nanotubes.* Journal of the American Ceramic Society 2009, 92, (6), pp. 1303-1310, DOI: 10.1111/j.1551-2916.2009.03055.x.

[8] Metaxa Z.S., Konsta-Gdoutos M.S., Shah S.P., *Mechanical Properties and Nanostructure of Cement-Based Materials Reinforced with Carbon Nanofibers and Polyvinyl Alcohol (PVA) Microfibers.* Advances in the Material Science of Concrete, SP-270—10.

GRADIENT-ENHANCED MODEL OF TRABECULAR BONE

MARTIN HORÁK[1], MILAN JIRÁSEK [2],

Abstract: *The present paper deals with a regularized constitutive model of trabecular bone, combining anisotropic elasto-plasticity with isotropic damage. The regularization is based on the implicit gradient approach applied to the damage-driving variable. The gradient-enhanced model has been implemented into a finite element code and has been used to simulate compressive failure of a vertebral body.*

Keywords: *trabecular bone, plasticity, damage, gradient-enhanced continuum*

1. INTRODUCTION

Trabecular bone is a porous, heterogeneous and anisotropic material with a complex microstructure. The morphological information computed from μCT can provide a good basis for the development of phenomenological models at the macroscopic level. The structure of trabecular bone is described by the volume fraction and the fabric tensor.

2. CONSTITUTIVE MODEL

This section presents a constitutive model of trabecular bone at small strains [1, 2]. Trabecular bone is modeled as an anisotropic elasto-plastic material with isotropic damage. The stress-strain law for such a model is

$$\boldsymbol{\sigma} = (1-\omega)\overline{\boldsymbol{\sigma}} = (1-\omega)\mathbf{D}_e : (\boldsymbol{\varepsilon} - \boldsymbol{\varepsilon}_p) \qquad (1)$$

where ω is a scalar describing the amount of damage, $\mathbf{D}_e$ is the anisotropic stiffness tensor, $\boldsymbol{\varepsilon}$ is the total strain, $\boldsymbol{\varepsilon}_p$ is the plastic part of strain, $\boldsymbol{\sigma}$ is the nominal stress and $\overline{\boldsymbol{\sigma}}$ is the effective stress.

[1] Ing. Martin Horák; Faculty of Civil Engineering, Czech Technical University in Prague, Thakurova 7/2077, Praha 6, Czech Republic, 166 29, Martin.Horak@fsv.cvut.cz

[2] Prof. Ing., DrSc; Milan Jirásek; Faculty of Civil Engineering, Czech Technical University in Prague, Thakurova 7/2077, Praha 6, Czech Republic, 166 29, Milan.Jirasek@fsv.cvut.cz

2.1 ANISOTROPIC ELASTICITY

The anisotropy of bone is described by a second-order positive definite fabric tensor

$$\mathbf{M} = \sum_{i=1}^{3} m_i (\mathbf{m}_i \otimes \mathbf{m}_i) \qquad (2)$$

where $\mathbf{m}_i$ are eigenvectors and m_i are eigenvalues normalized by $m_1 + m_2 + m_3 = 3$.

In principal coordinates of the fabric tensor, the orthotropic elastic compliance tensor $\mathbf{C}$ is represented by the matrix

$$\mathbf{C} = \begin{bmatrix} \frac{1}{E_1} & -\frac{\nu_{12}}{E_1} & -\frac{\nu_{13}}{E_1} & 0 & 0 & 0 \\ -\frac{\nu_{21}}{E_2} & \frac{1}{E_2} & -\frac{\nu_{23}}{E_2} & 0 & 0 & 0 \\ -\frac{\nu_{31}}{E_3} & -\frac{\nu_{32}}{E_3} & \frac{1}{E_3} & 0 & 0 & 0 \\ 0 & 0 & 0 & \frac{1}{2G_{23}} & 0 & 0 \\ 0 & 0 & 0 & 0 & \frac{1}{2G_{13}} & 0 \\ 0 & 0 & 0 & 0 & 0 & \frac{1}{2G_{13}} \end{bmatrix} \qquad (3)$$

with elastic moduli and Poisson's ratios expressed in terms of the fabric tensor eigenvalues as

$E_i = E_0 \rho^k m_i^{2l}$, $\nu_{ij} = \nu_0 \frac{m_i^l}{m_j^l}$ and $G_{ij} = G_0 \rho^k m_i^l m_j^l$.

Parameter ρ is the bone volume fraction, which reflects porosity of the bone, and parameters E_0, ν_0, G_0 are the elastic modulus, Poisson's ratio and shear modulus of a poreless ($\rho = 1$) isotropic material ($m_1 = m_2 = m_3 = 1$). The elastic stiffness matrix

$$\mathbf{D}_e = \mathbf{C}^{-1} \qquad (4)$$

is obtained simply by inversion of elastic compliance.

2.2 ANISOTROPIC PLASTICITY

The plastic part of the model is described in the effective stress space, i.e. in the undamaged space. The main ingredients of the theory of plasticity are the yield function, the flow rule, the hardening law and the loading-unloading conditions. The yield function

$$f(\overline{\boldsymbol{\sigma}}, \kappa) = \sqrt{\overline{\boldsymbol{\sigma}} : \mathbf{F} : \overline{\boldsymbol{\sigma}}} - \sigma_y(\kappa) \qquad (5)$$

corresponds to a generalized Hill's criterion with isotropic hardening. The current yield stress

$$\sigma_y(\kappa) = 1 + \sigma^H\left(1 - e^{-s\kappa}\right) \qquad (6)$$

grows as a function of the cumulative plastic strain. The flow rule is considered as associative:

$$\dot{\boldsymbol{\varepsilon}}^p = \dot{\lambda}\frac{\partial f}{\partial \overline{\boldsymbol{\sigma}}} \qquad (7)$$

The loading-unloading conditions have the classical form

$$\dot{\lambda} \geq 0 \qquad f \leq 0 \qquad \dot{\lambda} f = 0 \qquad (8)$$

In the equations above, λ is the plastic multiplier, s and σ^H are positive material parameters, to be identified from experiments and κ is the cumulative plastic strain defined incrementally as

$$\dot{\kappa} = \sqrt{\dot{\boldsymbol{\varepsilon}}^p : \dot{\boldsymbol{\varepsilon}}^p} \qquad (9)$$

The structure of the fourth-order tensor $\mathbf{F}$ is linked to the fabric tensor and bone volume fraction and has a similar structure to the compliance tensor; in principal coordinates it is represented by the matrix

$$\mathbf{F} = \begin{bmatrix} \frac{1}{(\sigma_1^p)^2} & -\frac{\chi_{12}}{(\sigma_1^p)^2} & -\frac{\chi_{13}}{(\sigma_1^p)^2} & 0 & 0 & 0 \\ -\frac{\chi_{21}}{(\sigma_2^p)^2} & \frac{1}{(\sigma_2^p)^2} & -\frac{\chi_{23}}{(\sigma_2^p)^2} & 0 & 0 & 0 \\ -\frac{\chi_{31}}{(\sigma_3^p)^2} & -\frac{\chi_{32}}{(\sigma_3^p)^2} & \frac{1}{(\sigma_3^p)^2} & 0 & 0 & 0 \\ 0 & 0 & 0 & \frac{1}{2\tau_{23}^2} & 0 & 0 \\ 0 & 0 & 0 & 0 & \frac{1}{2\tau_{13}^2} & 0 \\ 0 & 0 & 0 & 0 & 0 & \frac{1}{2\tau_{12}^2} \end{bmatrix} \qquad (10)$$

with $\sigma_i^p = \sigma_0^p \rho^k m_i^{2q}$, $\chi_{ij} = \chi_0 \frac{m_i^{2q}}{m_j^{2q}}$, $\tau_{ij} = \tau_0 \rho^k m_i^q m_j^q$, where σ_i^p is the uniaxial yield stress along the i-th axis $(i = 1,2,3)$, τ_{ij} is the yield stress in shear in the $i-j$ plane $(i, j = 1,2,3; i \neq j)$ and χ_{ij} are the interaction coefficients. Parameters σ_0^p, χ_0, τ_0 correspond to a poreless isotropic material.

2.3 ISOTROPIC DAMAGE

Damage evolution is assumed to be driven by the cumulative plastic strain, and the scalar damage variable is given by

$$\omega(\kappa) = \omega_c \left(1 - e^{-a\kappa}\right) \qquad (11)$$

where ω_c is the critical damage and a is a positive dimensionless parameter that controls the softening part of the stress-strain diagram.

3. IMPLICIT GRADIENT REGULARIZATION

Evolution of damage leads to softening, which is a destabilizing factor that may lead to localization of inelastic processes into narrow bands. The boundary value problem becomes ill-posed due to the loss of ellipticity of the governing differential equation resulting to pathological sensitivity of the numerical results with respect to the size and orientation of the finite element mesh. To avoid this pathological behavior, the model is regularized by the implicit gradient formulation. In this approach, the damage variable is computed from the so-

called over-nonlocal cumulated plastic strain while the plastic part of the model remains local. The over-nonlocal cumulated plastic strain is defined as

$$\hat{\kappa} = (1-m)\kappa + m\bar{\kappa} \qquad (12)$$

where $\bar{\kappa}$ is the nonlocal cumulated plastic strain and m is a model parameter. Full regularization can be achieved only if parameter *m* is greater than 1 [4]. The nonlocal cumulated plastic strain is computed from a Helmholz-type differential equation

$$\bar{\kappa} - l^2 \nabla^2 \bar{\kappa} = \kappa \qquad (13)$$

with homogeneous Neumann boundary condition. In *(13)*, *l* is the length-scale parameter and ∇^2 is the Laplace operator.

4. NUMERICAL IMPLEMENTATION

4.1 RETURN-MAPPING ALGORITHM

To implement the local constitutive model into a displacement-driven finite element code, the governing equations need to be expressed in an incremental form and an algorithm for the evaluation of the stress increment from a given strain increment must be developed. In plasticity, this procedure is called the stress-return algorithm. Within a computational increment number $n+1$, the mapping of strain at the end of the step, $\boldsymbol{\varepsilon}^{n+1}$, onto the effective stress at the end of step, provided by the stress-return algorithm, is denoted as function $\boldsymbol{\theta}$, and the mapping of strain $\boldsymbol{\varepsilon}^{n+1}$ onto cumulated plastic strain κ^{n+1} at the end of the step is denoted as function $\boldsymbol{\theta}_\kappa$. Details about the stress-return algorithm can be found in [1, 2]. The over-nonlocal formulation described in the previous chapter has a computational advantage, because the plastic part of the model remains local and the standard return mapping algorithm can be used.

4.2 GRADIENT-ENHANCED MODEL

Here we focus on the numerical implementation of the gradient-enhanced constitutive model into the finite element code. We start from the strong form of the set of governing differential equations

$$\nabla \cdot \boldsymbol{\sigma} = \mathbf{0} \tag{14}$$

$$\bar{\kappa} - l^2 \nabla^2 \bar{\kappa} = \kappa \tag{15}$$

Following the standard procedure, equations *(14)* and *(15)* are recast in the weak form,

$$\int_V (\nabla \cdot \boldsymbol{\sigma}) \boldsymbol{\eta} dx = 0 \tag{16}$$

$$\int_V \left(\bar{\kappa} - l^2 \nabla^2 \bar{\kappa}\right) \eta dx = \int_V (\kappa) \eta dx \tag{17}$$

where $\boldsymbol{\eta}$ and η are suitable test functions. The displacements and the nonlocal cumulative plastic strains are discretized at the element level by

$$\mathbf{u} = \mathbf{N}\mathbf{d} \qquad \bar{\kappa} = \mathbf{N}_\kappa \mathbf{d}_\kappa \tag{18}$$

After discretization, we obtain the set of nonlinear algebraic equations

$$\begin{Bmatrix} \mathbf{f}_{\text{int}} \\ \varphi_{\text{int}} \end{Bmatrix} = \begin{Bmatrix} \mathbf{f}_{ext} \\ \mathbf{0} \end{Bmatrix} \tag{19}$$

in which $\mathbf{f}_{\text{int}} = \int_V \left(\mathbf{B}^T \boldsymbol{\sigma}\right) dx$ and $\mathbf{f}_{ext} = \int_\Gamma \mathbf{N}^T \mathbf{t} dS$ are the standard internal and external forces and $\varphi_{\text{int}} = \int_V \left(\mathbf{N}_\kappa^T \mathbf{N} + l^2 \mathbf{B}_\kappa^T \mathbf{B}_\kappa - \kappa \mathbf{N}_\kappa^T\right) dx$ are generalized internal forces.

The set of nonlinear equations *(19)* is solved by the Newton-Raphson iteration scheme. This numerical method requires a tangent matrix, which is obtained by differentiating the internal force vector with respect to the nodal unknowns:

$$\mathbf{K} = \begin{bmatrix} \dfrac{\partial \mathbf{f}_{\text{int}}}{\partial \mathbf{d}} & \dfrac{\partial \mathbf{f}_{\text{int}}}{\partial \mathbf{d}_\kappa} \\ \dfrac{\partial \varphi_{\text{int}}}{\partial \mathbf{d}} & \dfrac{\partial \varphi_{\text{int}}}{\partial \mathbf{d}_\kappa} \end{bmatrix} \tag{20}$$

where

$$\frac{\partial \mathbf{f}_{\text{int}}}{\partial \mathbf{d}} = \int_V (1-\omega)\mathbf{B}^T \frac{\partial \boldsymbol{\theta}}{\partial \boldsymbol{\varepsilon}} \mathbf{B} dx \qquad \frac{\partial \mathbf{f}_{\text{int}}}{\partial \mathbf{d}} = -\int_V m \frac{d\omega}{d\kappa} \mathbf{B}^T \bar{\boldsymbol{\sigma}} \mathbf{N}_\kappa dx$$

$$\frac{\partial \varphi_{\text{int}}}{\partial \mathbf{d}_\kappa} = -\int_V \mathbf{N}_\kappa^T \frac{\partial \boldsymbol{\theta}_\kappa}{\partial \boldsymbol{\varepsilon}} \mathbf{B} dx \qquad \frac{\partial \varphi_{\text{int}}}{\partial \mathbf{d}_\kappa} = \int_V \mathbf{N}_\kappa^T \mathbf{N}_\kappa + l^2 \mathbf{B}_\kappa^T \mathbf{B}_\kappa dx$$

In the equations above, functions $\boldsymbol{\theta}$ and $\boldsymbol{\theta}_\kappa$ are supplied by the return mapping algorithm, and $\mathbf{B} = \frac{\partial \mathbf{N}}{\partial \mathbf{x}}$, $\mathbf{B}_\kappa = \frac{\partial \mathbf{N}_\kappa}{\partial \mathbf{x}}$.

5. NUMERICAL EXAMPLE

The regularized constitutive model has been implemented into OOFEM [7,8], an object-oriented finite element code. As an example, simulation of a vertebral body performed with the gradient version of the damage-plasticity model of trabecular bone is presented, and the results are compared to the integral nonlocal version of the model [1]. The force-displacement curve shows good agreement between the results obtained by the integral nonlocal formulation and the gradient-enhanced scheme.

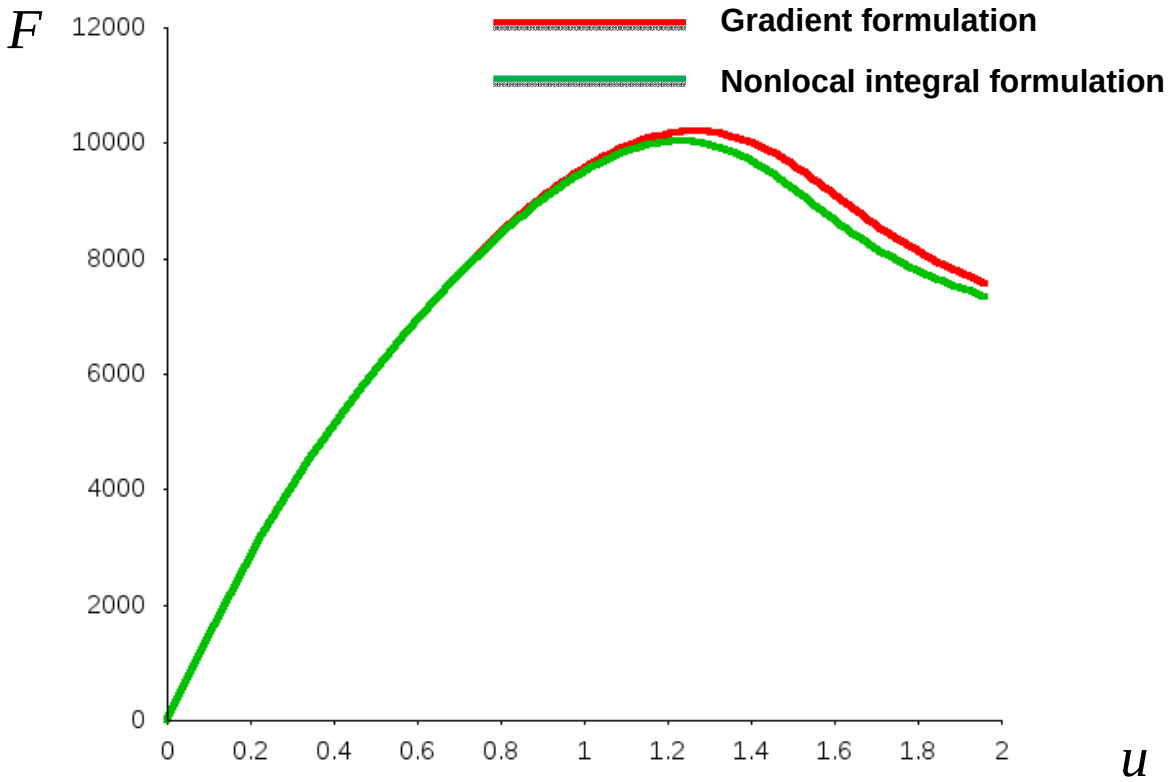

Fig. 1. Force displacement curve

6. CONCLUSION

The gradient-enhanced model of trabecular bone has been described and its computational implementation has been presented. The numerical example shows that the results obtained by the gradient approach are close to the results obtained by the nonlocal integral approach. The future work will focus on the comparison of the computational efficiency of gradient and integral approaches and on the extension of the model to the large-strain regime.

ACKNOWLEDGEMENT

Financial support received from the Czech Science Foundation under project GACR P108/11/1243 and from the Czech Technical University in Prague under project SGS11/021/OHK1/1T/11 is gratefully acknowledged.

REFERENCES

[1] Charlebois, M., Jirásek, M., Zysset, P.K. 2010. *A nonlocal constitutive model for trabecular bone softening in compression*. in Biomech. Model. Mechanobiol. 9

[2] Horák, M., Jirásek, M., Charlebois, M., Zysset, P.K. 2011. *Nonlocal tangent operator for damage-plasticity model*, in Programs and Algorithms of Numerical Mathematics

[3] Bažant, Z.P., Jirásek, M. 2002. *Nonlocal integral formulations of plasticity and damage: Survey of progress*, in Journal of Engineering Mechanics ASCE, 128

[4] Jirásek, M. & Rolshoven, S. (2003) *Comparison of integral-type nonlocal plasticity models for strain-softening materials,* in International Journal of Engineering Science, 41,

[5] Peerlings, R. H. J., de Borst, R., Brekelmans, W. A. M., de Vree, J. H. P. 1996. *Gradient-enhanced damage for quasi-brittle materials*, in International Journal for Numerical Methods in Engineering, 39

[6] Simone, A., Askes, H., Peerlings, R.H.J., Sluys, L.J. 2003. *Interpolation requirements for implicit gradient-enhanced continuum damage models*, in Communications in Numerical Methods in Engineering, 19

[7] Patzák, B. & Bittnar, Z. 2001. *Design of object oriented finite element code,* Advances in Engineering Software, 32

[8] Patzák, B., Rypl D., Bittnar, Z. 2001. *Parallel explicit finite element dynamics with nonlocal constitutive models.* Computers and Structures, 79

PRECISE FULL-VOLUME STRAIN MEASUREMENT WITHIN TRABECULAR BONE USING DIGITAL VOLUMETRIC CORRELATION METHOD

Ivan Jandejsek[1], **Ondřej Jiroušek** [2], **Daniel Vavřík** [3]

Abstract: *Digital volumetric correlation (DVC) method was employed for evaluation of full-volume displacement and strain fields in deformed trabecular bone specimen. Volumetric image data were acquired using time lapse X-ray micro-CT during gradually specimen loading. Tetrahedral Finite Element (FE) mesh was generated describing related volumetric data. The displacement fields were measured in set of control points by DVC utilizing vertices of this tetrahedral FE mesh and subsequently, the strain fields were computed from the measured displacement fields.*

Keywords: *Digital Volumetric Correlation, trabecular bone, Micro-CT, Strain measurement*

1. INTRODUCTION

Microstructural properties and spatial arrangement of the inner structure are the key factor for the overall mechanical properties of complex natural materials such as trabecular bone [1]. In recent years 3-D imaging techniques were established which enables direct measurement of structural properties of the complex material, namely microfocus Computed Tomography (micro-CT) [2]. Micro-CT can be used not only for non-destructive reconstruction of the inner microstructure and for measuring of some morphological properties of a material, but it can be successfully applied to record deforming microstructure under applied mechanical (or other) loading.

[1] Ing. Ivan Jandejsek; Faculty of Civil Engineering CTU in Prague; Thákurova 7, 166 29 Prague 9, Czech Republic; jandejs@itam.cas.cz

[2] Doc. Ing. Ondřej Jiroušek Ph.D.; Institute of Theoretical and Applied Mechanics CAS, v.v.i.; Prosecká 76, 190 00 Prague 9, Czech Republic; jirousek@itam.cas.cz

[3] Ing. Daniel Vavřík Ph.D.; Institute of Experimental and Applied Physics CTU in Prague; Horská 3a/22, 128 00 Prague 2, Czech Republic; vavrik@itam.cas.cz

In this study a three-dimensional variant of digital image correlation algorithm (DIC) [3] - digital volumetric correlation (DVC) is used to quantify the displacements and strains in the material with complex microstructure – trabecular bone. The bone microstructure is discretized using a tetrahedral mesh. In the nodal points of the mesh the displacement vector is computed using DVC. For each of the tetrahedral element the Green-Lagrange strain tensor is calculated from the displacements of its vertices. The overlaid tetrahedral mesh serves not only for the calculation of the deformation tensor, but also for easy visualization of the vector and tensor fields and for fast and direct comparison with results of numerical simulations. The numerical simulations can use the existing tetrahedral mesh or the mesh can easily refined/coarsened if needed.

2. EXPERIMENT

A cylindrical sample (diameter = 5mm, height = 8mm) of trabecular bone was extracted from porcine proximal femur. A special loading device with the mounted sample were placed on the rotating table into the micro-CT shielded box and scanned during incremental compressive loading, see Fig. 1.

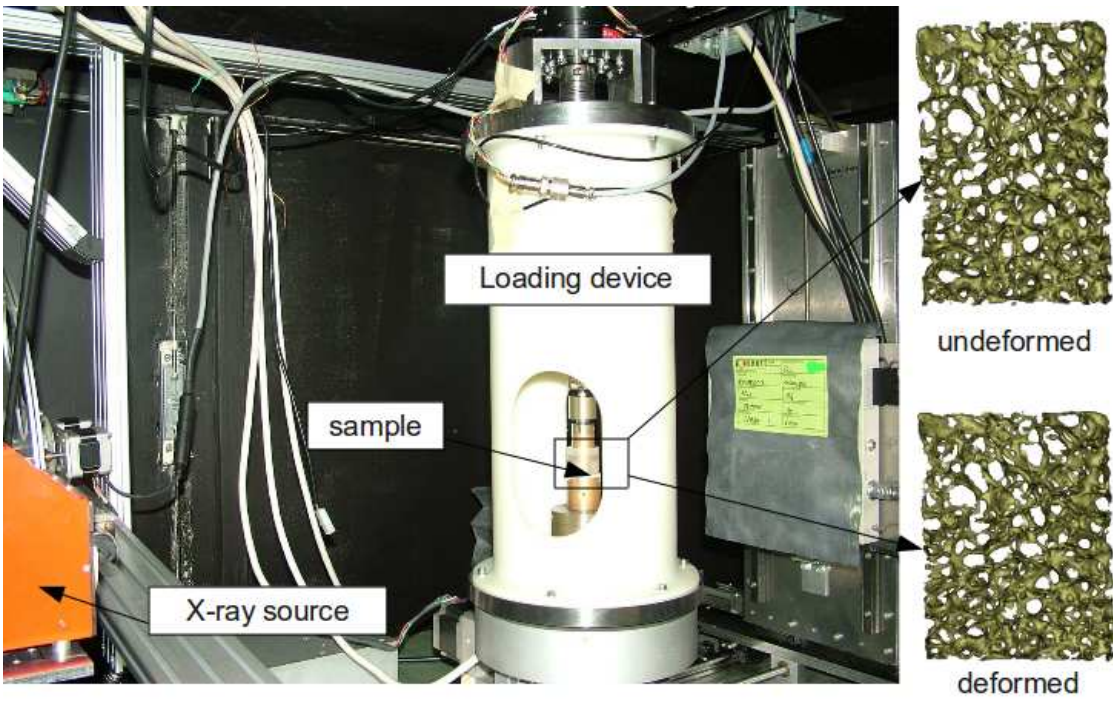

Fig. 1. Experimental setup and the reconstructed specimen of trabecular bone in reference (un-deformed) state and deformed state.

The sample was gradually loaded in compression up to 3% strain in six 0,5% increments and in each loading step the deformed microstructure was tomographically captured. After

each load step the sample was allowed to relax for 20 minutes until the force value relaxed. The force was continuously recorded with a 100 N load cell (U9B, Hottinger Baldwin Messtechnik, Germany). For the tomographic measurements an X-ray source (Hamamatsu L8601-01 with 5 mm focal spot size) and large-area flat-panel detector (Hamamatsu C7942CA-22, 1200×1000 pixel resolution and 50 µm pitch, physical dimensions 120×120 mm) were used.

3. DEFORMATION MEASUREMENT

3.1. DEFINITION OF MEASUREMENT GRID FOR DVC

After the 3D image data reconstruction, a finite element (FE) mesh was defined on the un-deformed sample consisting of connected linear tetrahedra using a Delaunay triangulation, see Fig. 2.

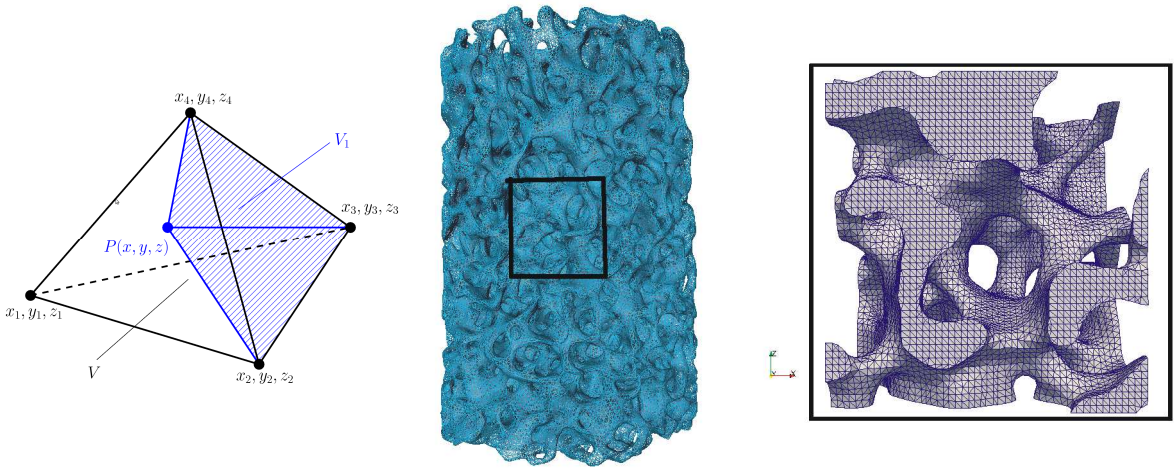

Fig. 2. Tetrahedral element (left), tetrahedral mesh of the entire reconstructed data (middle) and the smaller central part in which the strain measurement was carried out (right).

The FE mesh serves as a reference (un-deformed) state from which the deformed states are incrementally computed by sequential tracking of the displacements of the vertices. Moreover, the FE mesh provides easy visualization of the results, basically any FE postprocessor can be used. The movement of the vertices is tracked using a Digital Volumetric Correlation (DVC) method described in following paragraphs.

3.2. DIGITAL VOLUMETRIC CORRELATION - DISPLACEMENT MEASUREMENT

The digital volumetric correlation (DVC) method employed for evaluation of the full-volume displacement field is an extension of the well-known two-dimensional digital image correlation (DIC) [3] to all three spatial dimensions. Computational principles of these methods are very similar except that in DVC one works with 3D image data instead of classical 2D images in DIC. The technique utilizes a sequence of consecutive 3D image data (at least two) that represents the process of the object deformation. In this sequence DVC observes a movement of individual sub-volume templates by employing the correlation technique, see Fig. 3. The sub-volume template is a small part of the 3D image data that has to contain a distinguishable part of the object inner structure.

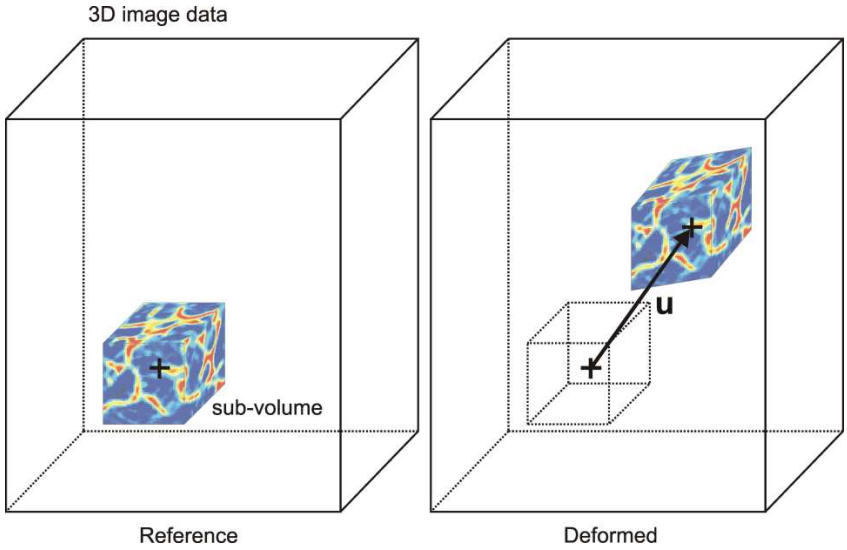

Fig. 3. Principle of Digital Volumetric Correlation - evaluation of sub-volume template displacement vector between reference image data and deformed image data.

The tracking algorithm works in two steps. First, an integer value of voxel displacement is evaluated using normalized cross-correlation. Subsequently, these integer values of displacement are passed on as initial inputs into the second step which is 3D extension of iterative Lucas-Kanade algorithm [4]. This step takes into account own deformation of the reference sub-volume template. The algorithm is based on the minimizing of the sum of squared error between reference and deformed sub-volume. After a few iterations (3-6), LK gives a new sub-pixel destination of the central voxel of the sub-volume template. Precision of the displacement has been shown to be 0.005 pixel in the means of standard deviation [5].

3.3. STRAIN EVALUATION

From the displacement field assessed by the described correlation method in each vertex of the FE mesh, the strain tensor is computed in every element. Due to the relatively large strain increments and due to the highly localized strains in thin trabeculae, it is necessary to compute the finite Green-Lagrange strain tensor instead of the often used infinitesimal (small) strain tensor. Typical feature of this method is that the precision of measured displacements are fine instead of computed strains that are affected by noisy displacements. Therefore, a smoothing process of the displacement field had to be employed before strain computation.

4. RESULTS

Due to the extremely complex inner structure of the specimen, the entire tetrahedral mesh consisted of more than 1 million elements. For easier visualization smaller FE models have been created from the volumetric image data as shown in Fig. 1. These smaller FE parts were developed in the central part of the specimen using 50x50x50 voxels and served for evaluation of the displacements and strains during the compression test. Even for these smaller volumes the DVC had to be performed in $35x10^3$ nodal points and $154x10^3$ elements. Each of the nodal points served as the center of a 17x17x17 voxel sub-volume template for the DVC which made the DVC for the whole sample extremely computationally expensive. Finally, resulting strain fields (vertical nominal component in the direction of loading) showing the localized strain bands within two smaller parts of the trabecular structure are shown in Fig. 4.

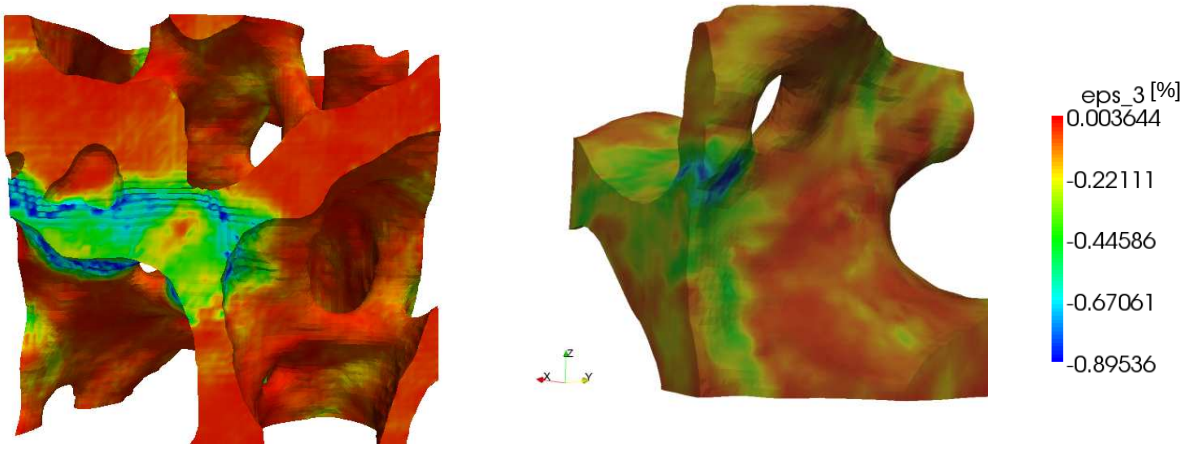

Fig. 4. Vertical nominal strain ε_3 evaluated in the smaller parts of the specimen at maximal loading level. Localized strain bands in the trabecular structure are clearly visible.

5. CONCLUSIONS

Presented DVC technique enables measurement of displacements and strains in a loaded microstructure. The underlying FE mesh serves not only for visualization but also verification of FE models against experiments. This is important e.g. in comparison of material models used for large-strain analysis, where material and geometrical nonlinearities are dominant. This will be addressed in future work. Described algorithms are computationally expensive and for large number of control points the evaluation of such an experiment is time consuming. It is not easy to reduce the number of nodal points because of the shape complexity of studies materials. However, since all the algorithms used in the study are in principle efficient for parallel computing, it is possible to use a multiprocessor system or to utilize modern GPUs. The method is suitable for parallelization using the CUDA architecture.

ACKNOWLEDGEMENT

The research has been supported by the Grant Agency of Czech Technical University in Prague (grant No. SGS10/135/OHK1/2T/11) and by the Grant Agency of the Czech Republic (grant No. P105/10/2305).

REFERENCES

[1] Wagner, H.D., Weiner, S., On the relationship between the microstructure of bone and its mechanical stiffnes, *J Biomech* 1992, 25(11), 1311–1320.

[2] Jones A.C., Sakellariou A., Limaye A., et al., Investigation of microstructural features in regenerating bone using micro computed tomography. *J Mater Sci Mater Med*. 2004;15:529–532.

[3] T.C. Chu, W.F. Ranson, M.A. Sutton and W.H. Peters, Application of digital-image-correlation techniques to experimental mechanics, *Exp. Mech. 25*, 1985, 232.

[4] B. D. Lucas and T. Kanade, An iterative image registration technique with an application to stereo vision. *Proceedings of Imaging Understanding Workshop*, 1981, 121-130.

[5] I. Jandejsek, O. Jiroušek, D. Vavřík, Precise strain measurement in complex materials using Digital Volumetric Correlation and time lapse micro-CT data, *Procedia Engineering, Vol. 10, 11th International Conference on the Mechanical Behavior of Materials (ICM11)*, 2011, 1730-1735

SAMPLING-BASED SENSITIVITY ANALYSIS FOR DESIGNING TRUSS STRUCTURES

ELIŠKA JANOUCHOVÁ[1], ANNA KUČEROVÁ[2]

Abstract: *Sensitivity analysis is a useful tool in the process of designing large truss structures to determine the most important dimensions and material properties influencing stability and price of the structure. The accuracy of the sensitivity prediction depends on the choice of design points called as the design of experiments. The aim of the presented paper is to review and compare available criteria determining the design of experiments suitable for sampling-based sensitivity analysis.*

Keywords: *design of experiments, discrete domains, space-filling, orthogonality, sampling-based sensitivity analysis*

1. INTRODUCTION

Sensitivity analysis (SA) is an important tool for investigating properties of complex systems. It is an essential part of inverse analysis procedures [1] and it is also closely related to response surface modelling [2] or uncertainty analysis [3]. To be more specific, sensitivity analysis provides some information about the contributions of individual system parameters/model inputs to the system response/model outputs. A number of approaches to sensitivity analysis has been developed, see e.g. [4] for an extensive review. The presented contribution is focused on widely used sampling-based approaches [2], in particular to evaluation of Spearman's rank correlation coefficient (SRCC), which is able to reveal nonlinear monotonic relationship between the inputs and the corresponding outputs.

When computing the sensitivity analysis in a case of some real system using expensive experimental measurements or some computationally exhaustive numerical model simulations, the number of samples to be performed within some reasonable time is rather

[1] Eliška Janouchová; Faculty of Civil Engineering, Czech Technical University in Prague; Thákurova 7/2077, 166 29 Prague, Czech Republic; eliska.janouchova@fsv.cvut.cz

[2] Ing. Anna Kučerová, Ph.D.; Faculty of Civil Engineering, Czech Technical University in Prague; Thákurova 7/2077, 166 29 Prague, Czech Republic; anicka@cml.fsv.cvut.cz

limited. Randomly chosen sets of input parameters do not ensure appropriate estimation of related sensitivities. Therefore the sets must be chosen carefully. In this contribution we would like to present a review and comparison of several criteria, which can govern the stratified generation of input sets called as design of experiments (DOE).

2. CRITERIA FOR ASSESING OPTIMAL DESIGNS

A number of different criteria for assessing the quality of particular DOE can be found in literature. They can be organized into groups with respect to the preferred DOE property.

2.1 SPACE-FILLING CRITERIA

One of the most widely preferred features is space-filling property, which is needed in order to allow for evaluation of sensitivities valid for the whole given domain of admissible input values, so-called design space.

Audze-Eglais objective function (AE) proposed by Audze and Eglais [6] is based on a potential energy among design points. The points are distributed as uniformly as possible when the potential energy E^{AE} proportional to the inverse of the squared distance between points is minimized, i.e.

$$E^{AE} = \sum_{i=1}^{n} \sum_{j=i+1}^{n} \frac{1}{L_{ij}^2}, \qquad (1)$$

where n is the number of design points and L_{ij} is the Euclidean distance between points i and j.

Euclidean maximin (EMM) distance is probably the best-known space-filling measure [7, 8]. It states that the minimal distance $L_{min,ij}$ between any two points i and j should be maximal. In order to apply the minimization procedure to all presented criteria, we minimize the negative value of minimal distance.

Modified L_2 discrepancy (ML_2) is a computationally cheaper variant of discrepancy measure, which is widely used to assess precision for multivariate quadrature rules [9]. Here, the designs are normalized to the interval [0; 1] in each dimension and then, the value of ML_2 is computed according to

$$E^{ML_2} = \left(\frac{4}{3}\right)^k - \frac{2^{(1-k)}}{n} \sum_{d-1}^{n} \prod_{i=1}^{k} \left(3 - x_{di}^2\right) + \frac{1}{n^2} \sum_{d=1}^{n} \sum_{j=1}^{n} \prod_{i=1}^{k} \left[2 - \max\left(x_{di}, x_{ji}\right)\right], \qquad (2)$$

where *k* is the number of input parameters, i.e. the dimension of the design space.

D-optimality criterion (Dopt) was proposed by Kirsten Smith in 1918 [10] as a pioneering work in the field of DOE for regression analysis. This criterion minimizes the variance associated with estimates of regression model coefficients. We employ a Bayesian modification to the so-called information matrix (Z^TZ) in order to eliminate duplicates in the final D-optimal design [11,12]. In order to apply a minimization procedure we can minimize negative value of the determinant of the information matrix, i.e.

$$E^{Dopt} = -\det\left(Z^T Z\right), \tag{3}$$

where Z is a matrix with evaluated regression terms in design points. In the case of second order polynomial regression and two-dimensional design space, the matrix becomes

$$Z = \begin{bmatrix} 1 & x_{11} & x_{12} & x_{11}^2 & x_{12}^2 & x_{11}x_{12} \\ 1 & x_{21} & x_{22} & x_{21}^2 & x_{22}^2 & x_{21}x_{22} \\ \vdots & \vdots & \vdots & \vdots & \vdots & \vdots \\ 1 & x_{n1} & x_{n2} & x_{n1}^2 & x_{n2}^2 & x_{n1}x_{n2} \end{bmatrix} \tag{4}$$

2.2 ORTHOGONALITY-BASED CRITERIA

Orthogonality of DOE is necessary to assess the impact of individual input parameters.

Conditional number (CN) is commonly used in numerical linear algebra to examine the sensitivities of a linear system [13]. Here, we use conditional number of X^TX, where X is a matrix of design points' coordinates, so-called design matrix

$$X = \begin{bmatrix} x_{11} & x_{12} & \cdots & x_{1k} \\ x_{21} & x_{22} & \cdots & x_{2k} \\ \vdots & \vdots & & \vdots \\ x_{n1} & x_{n2} & \cdots & x_{nk} \end{bmatrix}, \tag{5}$$

where *n* is the number of design points and *k* is the dimension of design space and the columns are centered to sum to 0 and scaled to the range [-1; 1].

Pearson product-moment correlation coefficient (PMCC) is a standard measure of linear dependence between two variables. In case of multi-dimensional design space, the orthogonality of the DOE can be achieved by minimizing

$$E^{PMCC} = \sqrt{\sum_{i=1}^{k}\sum_{j=i+1}^{k} c_{ij}^2}\,, \qquad (6)$$

where c_{ij} is the covariance of the two variables divided by the product of their standard deviations.

Spearman's rank correlation coefficient (SRCC) can be used to capture nonlinear but monotonic relationship between two variables and therefore, it can be efficiently applied for estimation of correlations in sample-based sensitivity analysis [2]. The idea is to replace the values of variables by their corresponding ranks. The orthogonality of the DOE can be achieved similarly to (6).

Kendall tau rank correlation coefficient (KRCC) is an alternative measure of nonlinear dependence between two variables. In particular, it is based on the number of concordant and discordant pairs of samples.

3. SENSITIVITY ANALYSIS

Each presented metric defines different DOE, which we obtained by the simulated re-annealing algorithm. It involved the repeated restart of the algorithm, namely, at the moments the temperature decreased to the prescribed minimal value. This modification increased the ability of the original algorithm to explore the search domain and to escape from local extremes. [14, 15]. DOE were generated according to LH restrictions [16], because employed examples are rather complex.

Sensitivity analysis was performed for four truss structures [17]. Figures 3, 4 and 5 show their schema, material properties and number of possible values for the cross-sectional areas, i.e. a size of a domain *n*. In every example a number of parameters *k* equals the amount of bars forming the structure. Weight *w*, maximum displacement *d* and maximum stress *s* of a structure are values of model response. The chosen model is evaluated in the set of *n* design points and corresponding parameter-response correlations is computed.

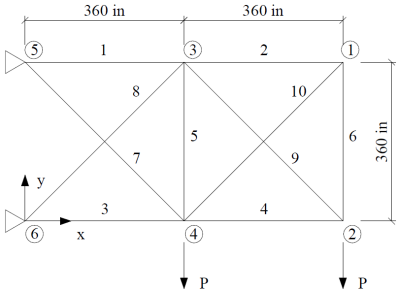

Material:	Aluminium
Density:	0.1 lb/in^3
Young's modulus:	10^7 psi
Load:	P =100 000 lb
Cross-sectional areas:	42

Fig. 3. Ten-bar planar truss.

To evaluate the error in the correlation prediction, we computed this correlation also for more extensive designs. An amount of design points differs according to the solved example. It is 6^{10} and 2^{25} for the ten- and 25-bar truss, respectively. These designs generated as an equal-spaced *k*-dimensional grid, while in case of the two other examples, the dimension of the search space is too large and hence, $5 \cdot 10^6$ design points were drawn randomly from the uniform distribution.

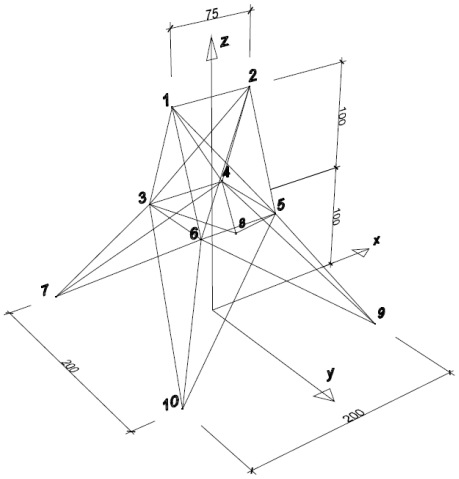

Material: Aluminium
Density: 0.1 lb/in^3
Young's modulus: 10^7 psi
Cross-sectional areas: 30
Load:

Joint	P_x [lb]	P_y[lb]	P_z[lb]
1	1000	-10 000	-10 000
2	0	-10 000	-10 000
3	500	0	0
6	600	0	0

Fig. 4. Twenty-five-bar space truss.

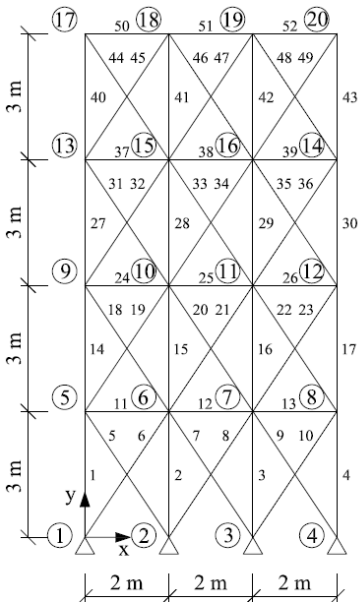

Density: 0.284 lb/in^3
Young's modulus: $3 \cdot 10^7$ psi
Cross-sectional areas: 64
Load:

Joint	P_x[lb]	P_y[lb]]
17	22 481	44 962
18	22 481	44 962
19	22 481	44 962
20	22 481	44 962

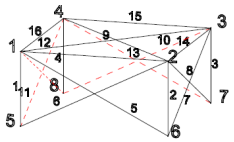

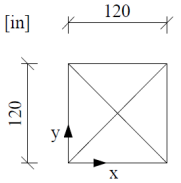

Density: 0.1 lb/in^3
Young's modulus: 10^7 psi
Cross-sectional areas: 32
Load:

Joint	P_x [lb]	P_y[lb]	P_z[lb]
1	5 000	5 000	-5 000

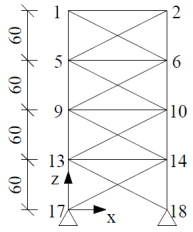

Fig. 5. Fifty-two-bar planar truss and seventy-two-bar space truss.

Following tables present the mean (Tab.1) and maximum (Tab.2) error in correlation estimates and, for an easier visible comparison, also the mark, which is obtained by multiplicating the error by 100 (in Tab. 2 by 10), rounding the result up and dividing by 12 (a number of models), i.e. the smaller mark is better.

Tab. 1. Mean errors in sensitivity prediction of the presented examples.

Example		AE	EMM	ML_2	Dopt	PMCC	SRCC	KRCC	CN
10 bar	w	0.046 ***5***	0.047 ***5***	0.022 ***3***	0.038 ***4***	0.067 ***7***	0.060 ***6***	0.058 ***6***	0.054 ***6***
	d	0.034 ***4***	0.038 ***4***	0.105 ***11***	0.046 ***5***	0.042 ***5***	0.045 ***5***	0.057 ***6***	0.052 ***6***
	s	0.035 ***4***	0.040 ***4***	0.138 ***14***	0.069 ***7***	0.066 ***7***	0.032 ***4***	0.082 ***9***	0.064 ***7***
25 bar	w	0.078 ***8***	0.074 ***8***	0.185 ***19***	0.037 ***4***	0.039 ***4***	0.073 ***8***	0.113 ***12***	0.039 ***4***
	d	0.103 ***11***	0.085 ***9***	0.151 ***16***	0.097 ***10***	0.069 ***7***	0.110 ***11***	0.123 ***13***	0.106 ***11***
	s	0.124 ***13***	0.108 ***11***	0.128 ***13***	0.117 ***12***	0.128 ***13***	0.133 ***14***	0.130 ***13***	0.149 ***15***
52 bar	w	0.077 ***8***	0.068 ***7***	0.157 ***16***	0.040 ***4***	0.058 ***6***	0.096 ***10***	0.086 ***9***	0.046 ***5***
	d	0.101 ***11***	0.068 ***7***	0.085 ***9***	0.045 ***5***	0.055 ***6***	0.099 ***10***	0.085 ***9***	0.044 ***5***
	s	0.091 ***10***	0.089 ***9***	0.069 ***7***	0.075 ***8***	0.079 ***8***	0.103 ***11***	0.106 ***11***	0.079 ***8***
72 bar	w	0.126 ***13***	0.126 ***13***	0.187 ***19***	0.104 ***11***	0.112 ***12***	0.156 ***16***	0.133 ***14***	0.140 ***14***
	d	0.122 ***13***	0.122 ***13***	0.138 ***14***	0.136 ***14***	0.125 ***13***	0.132 ***14***	0.143 ***15***	0.145 ***15***
	s	0.138 ***14***	0.142 ***15***	0.158 ***16***	0.140 ***14***	0.131 ***14***	0.132 ***14***	0.143 ***15***	0.156 ***16***
Mark		***9.50***	***8.75***	***13.08***	***8.17***	***8.50***	***10.25***	***11.00***	***9.33***

Tab. 2. Maximum errors in sensitivity prediction of the presented examples.

Example		AE	EMM	ML_2	Dopt	PMCC	SRCC	KRCC	CN
10 bar	w	0.102 ***2***	0.105 ***2***	0.064 ***1***	0.089 ***1***	0.184 ***2***	0.111 ***2***	0.130 ***2***	0.125 ***2***
	d	0.108 ***2***	0.082 ***1***	0.280 ***3***	0.141 ***2***	0.128 ***2***	0.115 ***2***	0.099 ***1***	0.114 ***2***
	s	0.098 ***1***	0.121 ***2***	0.339 ***4***	0.174 ***2***	0.205 ***3***	0.084 ***1***	0.171 ***2***	0.182 ***2***
25 bar	w	0.173 ***2***	0.226 ***3***	0.485 ***5***	0.085 ***1***	0.074 ***1***	0.144 ***2***	0.368 ***4***	0.108 ***2***
	d	0.287 ***3***	0.270 ***3***	0.312 ***4***	0.246 ***3***	0.187 ***2***	0.245 ***3***	0.294 ***3***	0.253 ***3***
	s	0.337 ***4***	0.270 ***3***	0.390 ***4***	0.386 ***4***	0.359 ***4***	0.346 ***4***	0.529 ***6***	0.390 ***4***
52 bar	w	0.251 ***3***	0.206 ***3***	0.223 ***3***	0.130 ***2***	0.201 ***3***	0.256 ***3***	0.261 ***3***	0.155 ***2***
	d	0.328 ***4***	0.245 ***3***	0.246 ***3***	0.130 ***2***	0.217 ***3***	0.302 ***4***	0.235 ***3***	0.172 ***2***
	s	0.338 ***4***	0.255 ***3***	0.227 ***3***	0.193 ***2***	0.247 ***3***	0.317 ***4***	0.315 ***4***	0.222 ***3***
72 bar	w	0.514 ***6***	0.352 ***4***	0.557 ***6***	0.383 ***4***	0.271 ***3***	0.423 ***5***	0.447 ***5***	0.494 ***5***
	d	0.392 ***4***	0.401 ***5***	0.555 ***6***	0.415 ***5***	0.376 ***4***	0.420 ***5***	0.471 ***5***	0.480 ***5***
	s	0.477 ***5***	0.402 ***5***	0.439 ***5***	0.469 ***5***	0.350 ***4***	0.485 ***5***	0.479 ***5***	0.469 ***5***
Mark		***3.33***	***3.08***	***3.92***	***2.75***	***2.83***	***3.33***	***3.58***	***3.08***

4. CONCLUSION

In our previous work [18] we compare eight criteria used for optimizing DOE in terms of ease of their optimization and their mutual qualities and we also computed SA for several elementary functions in two-dimensional domain. It was shown that Dopt is the most suitable for SA, followed the second best result obtained by PMCC with LH restrictions.

This paper reviews these criteria and presents their suitability for usage in sampling-based SA for designing truss structures. The obtained results in sensitivity predictions for behaviour of the presented structures confirm the previous results and Dopt and PMCC to be the most suitable criteria for SA. DOE of EMM, CN and AE provide also good results, while the

sensitivity predictions of KRCC and SRCC contain again large errors. ML_2 unexpectedly deteriorates giving the worst results of all the criteria.

ACKNOWLEDGEMENT

This outcome has been achieved with the financial support of the Czech Science Foundation, project No. 105/11/P370.

REFERENCES

[1] A. Kučerová, 2007. *Identification of nonlinear mechanical model parameters based on softcomputing methods*, Ph.D. thesis, Ecole Normale Supérieure de Cachan, Laboratoire de Mécanique et technologie.

[2] J.C. Helton, J.D. Johnson, C.J. Sallaberry, C.B. Storlie, 2006. *Survey of sampling-based methods for uncertainty and sensitivity analysis*, Reliab Eng Syst Safe.

[3] J.C. Helton, J.D. Johnson, W.L. Oberkampf, C.J. Sallaberry, 2006. *Sensitivity analysis in conjunction of with evidence theory representations epistemic uncertainty*, Reliab Eng Syst Safe.

[4] A. Saltelli, K. Chan , E. M. Scott, editors, 2000. *Sensitivity analysis*, New York, NY: Wiley.

[5] T. Goel, R.T. Haftka, W. Shyy, L.T. Watson, 2008. *Pitfalls of using a single criterion for selecting experimental design*, Int J Numer Meth Eng.

[6] P. Audze, V. Eglais, 1977. *New approach for planning out of experiments*, Problems of Dynamics and Strengths, Zinatne Publishing House.

[7] M. Johnson, L. Moore, D. Ylvisaker, 1990. *Minimax and maximin distance designs*, J Stat Plan Infer.

[8] M.D. Morris, T.J. Mitchell, 1995. *Exploratory designs for computer experiments*, J Stat Plan Infer.

[9] K.T. Fang, Y. Wang, 1994. *Number-theoretic Methods in Statistics*, London: Chapman & Hall.

[10] K. Smith, 1918. *On the standard deviations and interpolated values of an observed polynomial function and its constants and the guidance they give towards a proper choice of the distribution of observations*, Biometrika. 85 s.

[11] P.F. de Aguiar, B. Bourguignon, M.S. Khots, D.L. Massart, R. Phan-Than-Luu, 1995. *D-optimal designs*, Chemometr Intell Lab.

[12] M. Hofwing, N. Strömberg, 2010. *D-optimality of non-regular design spaces by using a Bayesian modification and a hybrid method*, Struct Multidiscip O.

[13] T.M. Cioppa, T.W. Lucas, 2007. *Efficient nearly orthogonal and space-filling Latin hypercubes*, Technometrics.

[14] S. Kirkpatrick, C. J. Gelatt, M. P. Vecchi, 1983. *Optimization by simulated annealing*, Science.

[15] J. Černý, 1985. *Thermodynamical approach to the traveling salesmanproblem: An efficient simulation algorithm*, Journal of Optimization Theory and Applications

[16] R.L. Iman,W.J. Conover, 1980. *Small sample sensitivity analysis techniques for komputer models, with an application to risk assessment*, Communications in Statistics - Theory and Methods.

[17] S.-J. Wu, P.-T. Chow, 1995. *Steady-state genetic algorithms for discrete optimization of trusses*, Computers & Structures.

[18] A. Kučerová, E. Janouchová, 2011. *Design of Experiments suitable for Sampling-Based Sensitivity Analysis*, in Proc. of the Second International Conference on Soft Computing Technology in Civil, Structural and Environmental Engineering, Civil-Comp Press, Stirlingshire, Scotland.

IMPLEMENTATION OF SLIP WITH FRICTION BOUNDARY CONDITION FOR FLOW PROBLEMS

FILIP KOLARIK[1], BOREK PATZAK[2],

Abstract: *In modeling of fresh concrete flow, one needs to consider proper boundary conditions on walls. Neither "full slip" nor "no slip" boundary condition is satisfactory in real applications. This paper is focused on implementation of "slip with friction" boundary condition into OOFEM code. In this boundary condition, the tangent component of stress vector is proportional to the tangent component of velocity vector.*

Keywords: slip boundary condition, flow simulation, fresh concrete.

1. INTRODUCTION

In modeling of flow problems, especially in real applications, one needs to devote attention to proper choice of boundary conditions. There are several ways of modeling influence of boundary to flow. Best known, and probably the easiest one, is "no slip" boundary condition, where tangent component of velocity is equal to zero at the boundary. Although this is not very physical, sometimes it is useful. Big problems arise in free surface problems. When eulerian description of flow is used (as usual in CFD), free surface is usually modeled as interface between two immiscible fluids. Then, the use of "no slip" boundary condition prevents the interface movements near the boundary. On the other side, one can apply "full slip" boundary condition. This is problematic especially in non-Newtonian flow, where the use of "full slip" boundary condition leads to undervaluation of yield stress effect. These two boundary conditions represent two extremes. Between them, one can distinguish between various types of friction. Let aside the case of constant friction (it can be a function of position and time – that makes no difference), which has to be known a priori. Suitable form of

[1] Ing. Kolařík Filip, Czech Technical University in Prague, Faculty of Civil Engineering, Department of Mechanics, filip.kolarik@fsv.cvut.cz

[2] Prof. Dr. Ing. Patzák Bořek, Czech Technical University in Prague, Faculty of Civil Engineering, Department of Mechanics, borek.patzak@fsv.cvut.cz

friction, so called “slip with friction” boundary condition was proposed by Galdi and Layton [5]. Tangent component of velocity is proportional to tangent component of stress vector. This boundary condition is also known as Navier boundary condition. The focus of this paper is on implementation of “slip with friction” boundary condition into OOFEM [6, 7] code.

The paper starts with problem formulation and then proceeds with derivation of contributing terms of governing equation. Finally, the response of numerical model with implemented boundary condition is tested.

2. FORMULATION OF PROBLEM

We are interested in modeling of incompressible Newtonian fluid flow, described by Navier-Stokes equations . The two-dimensional formulation will be considered here. Let Ω be bounded domain with boundary $\partial\Omega$, which is composed of three mutually disjoint parts Γ_D, Γ_{SWF}, Γ_{OUT}. On first part Γ_D Dirichlet boundary condition is prescribed, Γ_{SWF} is part of boundary, where slip with friction boundary condition is prescribed, and on Γ_{OUT}, so called “do nothing” boundary condition, is considered, which is usually used for modeling outflow. The problem under consideration has the following form:

$$\rho\frac{\partial \boldsymbol{u}}{\partial t}+\rho(\boldsymbol{u}\cdot\nabla)\boldsymbol{u}-\nabla\cdot\boldsymbol{\tau}-\nabla p-\rho\boldsymbol{b}=\boldsymbol{0}\ \ in\ \Omega \tag{1}$$

$$\nabla\cdot\boldsymbol{u}=0\ \ in\ \Omega \tag{2}$$

$$\boldsymbol{u}=\boldsymbol{g}\ \ on\ \ \Gamma_D \tag{3}$$

$$\boldsymbol{u}\cdot\boldsymbol{t}+\beta^{-1}\boldsymbol{n}\cdot(\boldsymbol{\tau}-p\boldsymbol{\delta})\cdot\boldsymbol{t}=0\ \ on\ \ \Gamma_{SWF} \tag{4}$$

$$\boldsymbol{n}\cdot(\boldsymbol{\tau}-p\boldsymbol{\delta})=\boldsymbol{0}\ \ on\ \ \Gamma_{OUT} \tag{5}$$

The unknowns are the velocity field $\boldsymbol{u}$ and the pressure p. The density ρ, body force $\boldsymbol{b}$ and Dirichlet boundary conditions $\boldsymbol{g}$ on Γ_D are prescribed. Friction parameter β in slip with friction boundary condition is assumed to be constant. The outer normal and tangent vectors $\boldsymbol{n}$, $\boldsymbol{t}$ are assumed to exist almost everywhere on $\partial\Omega$. The unit tensor is denoted by $\boldsymbol{\delta}$ and $\boldsymbol{\tau}$ is stress tensor, which is related to $\boldsymbol{u}$ by constitutive and geometrical equations, μ denotes viscosity:

$$\boldsymbol{\tau}=2\mu\boldsymbol{D} \tag{6}$$

$$\boldsymbol{D} = \frac{1}{2}\left(\nabla \boldsymbol{u} + (\nabla \boldsymbol{u})^T\right) \tag{7}$$

Choosing proper function spaces for unknown and test functions, variational formulation of (1-5) is obtained in usual way by multiplying with the pair of test function $\boldsymbol{w}$, q and integrating over whole domain.. After discretization, provided that proper finite element spaces are defined, stabilized finite element formulation of problem (1-5) can be stated as follows: find $\boldsymbol{u}^h \in \boldsymbol{S}_u^h$ and $p^h \in \boldsymbol{S}_p^h$ such that $\forall \boldsymbol{w}^h \in \boldsymbol{V}_u^h$ and $\forall q^h \in \boldsymbol{V}_p^h$ holds:

$$\begin{aligned}
&\int_\Omega \rho \boldsymbol{w}^h \cdot \frac{\partial \boldsymbol{u}^h}{\partial t}\, d\Omega + \int_\Omega \rho \boldsymbol{w}^h \cdot \left(\boldsymbol{u}^h \cdot \nabla \boldsymbol{u}^h\right) d\Omega + \int_\Omega \nabla \boldsymbol{w}^h : \boldsymbol{\tau}\left(\boldsymbol{u}^h\right) d\Omega - \int_\Omega \boldsymbol{w}^h \cdot \nabla p^h \, d\Omega \\
&\quad - \int_\Omega \boldsymbol{w}^h \cdot \boldsymbol{b}\, d\Omega - \int_\Gamma \boldsymbol{w}^h \cdot (\boldsymbol{\tau} - p\boldsymbol{\delta}) \cdot \boldsymbol{n}\, d\Gamma + \int_\Omega q^h \left(\nabla \cdot \boldsymbol{u}^h\right) d\Omega \\
&+ \sum_{el} \left[\int_{\Omega_e} \boldsymbol{\tau}_{SUPG} \left(\boldsymbol{u}^h \cdot \nabla \boldsymbol{w}^h\right) \cdot \left(\rho \frac{\partial \boldsymbol{u}^h}{\partial t} + \rho \boldsymbol{u}^h \cdot \nabla \boldsymbol{u}^h - \nabla \cdot \boldsymbol{\tau}\left(\boldsymbol{u}^h\right) + \nabla p^h - \boldsymbol{b} \right) d\Omega_e \right] \\
&+ \sum_{el} \left[\int_{\Omega_e} \tau_{PSPG} \frac{1}{\rho} \nabla q^h \cdot \left(\rho \frac{\partial \boldsymbol{u}^h}{\partial t} + \rho \boldsymbol{u}^h \cdot \nabla \boldsymbol{u}^h - \nabla \cdot \boldsymbol{\tau}\left(\boldsymbol{u}^h\right) + \nabla p^h - \boldsymbol{b} \right) d\Omega_e \right] \\
&\quad + \sum_{el} \left[\int_{\Omega_e} \tau_{LSIC} \nabla \cdot \boldsymbol{w}^h \rho \nabla \cdot \boldsymbol{u}^h \, d\Omega_e \right] = 0
\end{aligned} \tag{8}$$

Terms in the first two lines follow from standard Galerkin discretization, terms in the third line are due to SUPG stabilization, because of convective effects, terms in the fourth line provide PSPG stabilization (LBB condition is not satisfied), and last term provides additional stability for high velocities. Coefficients τ_{SUPG}, τ_{PSPG} and τ_{LSIC} can be computed as norm of certain terms of (8), see [2]. For further information about solving (8), see for example [3].

3. DERIVATION OF BOUNDARY CONDITION TERMS

In this paper, we are primarily interested in boundary term, arising from Green theorem

$$\int_\Gamma \boldsymbol{w}^h \cdot (\boldsymbol{\tau} - p\boldsymbol{\delta}) \cdot \boldsymbol{n}\, d\Gamma \tag{9}$$

For derivation of boundary condition terms, we will start at non-discretized form of term (9). in the case of outflow boundary condition, procedure is following:

$$\int_{\Omega} \nabla\cdot(\boldsymbol{\tau} - p\boldsymbol{\delta})\cdot\boldsymbol{w}\ d\Omega = \int_{\Gamma_{OUT}} \boldsymbol{n}\cdot\boldsymbol{\tau}\cdot\boldsymbol{w}\ d\Gamma - \int_{\Omega} \boldsymbol{\tau}:\nabla\boldsymbol{w}\ d\Omega - \int_{\Omega} \nabla p\cdot\boldsymbol{w}\ d\Omega = \int_{\Gamma_{OUT}} p(\boldsymbol{n}\cdot\boldsymbol{w})\ d\Gamma - \int_{\Omega} \boldsymbol{\tau}:\nabla\boldsymbol{w}\ d\Omega - \int_{\Omega} \nabla p\cdot\boldsymbol{w}\ d\Omega \tag{10}$$

where definition (5) of outflow boundary condition was used. Arose boundary term, the first one in second line of (10), is than discretized using suitable approximation functions. In our case, linear approximation is used. Using matrix notation, discretized term in element point of view has form:

$$\int_{\Gamma} \boldsymbol{N}^{T}\boldsymbol{n}\boldsymbol{N}\boldsymbol{p}\ d\Gamma\ \boldsymbol{p} \tag{11}$$

where

$$\boldsymbol{N} = \begin{bmatrix} N_1 & 0 & N_2 & 0 & N_3 & 0 \\ 0 & N_1 & 0 & N_2 & 0 & N_3 \end{bmatrix} \qquad \boldsymbol{N}\boldsymbol{p} = \begin{bmatrix} N_1 & N_2 & N_3 \end{bmatrix} \tag{12}$$

Here, N_1-N_3 are linear approximation functions on triangle, $\boldsymbol{p}$ is vector of unknown nodal values of pressure and $\boldsymbol{n}$ is unit outer normal vector to boundary.

In the case of slip with friction boundary condition, derivation is little bit longer. Again, we will start at non-discretized form of term (9). To derive the final discretized form, we need to decompose the test function $\boldsymbol{w}$ into normal and tangent components, like below:

$$\boldsymbol{w} = (\boldsymbol{w}\cdot\boldsymbol{n})\boldsymbol{n} + (\boldsymbol{w}\cdot\boldsymbol{t})\boldsymbol{t} \tag{13}$$

using this decomposition, further derivation can be done by

$$\int_{\Gamma_{SWF}} \boldsymbol{n}\cdot(\boldsymbol{\tau} - p\boldsymbol{\delta})\cdot\boldsymbol{w}\ d\Gamma = \int_{\Gamma_{SWF}} \left[\boldsymbol{n}\cdot(\boldsymbol{\tau} - p\boldsymbol{\delta})\right]\cdot\left[(\boldsymbol{w}\cdot\boldsymbol{n})\boldsymbol{n} + (\boldsymbol{w}\cdot\boldsymbol{t})\boldsymbol{t}\right]\ d\Gamma = \int_{\Gamma_{SWF}} (\boldsymbol{w}\cdot\boldsymbol{n})\boldsymbol{n}\cdot(\boldsymbol{\tau} - p\boldsymbol{\delta})\cdot\boldsymbol{n}\ d\Gamma + \int_{\Gamma_{SWF}} (\boldsymbol{w}\cdot\boldsymbol{t})\boldsymbol{n}\cdot(\boldsymbol{\tau} - p\boldsymbol{\delta})\cdot\boldsymbol{t}\ d\Gamma \tag{14}$$

and using slip with friction boundary condition (4), we have

$$\int_{\Gamma} \alpha^{-1}(\boldsymbol{w}\cdot\boldsymbol{n})(\boldsymbol{u}\cdot\boldsymbol{n})\ d\Gamma + \int_{\Gamma} \beta(\boldsymbol{w}\cdot\boldsymbol{t})(\boldsymbol{u}\cdot\boldsymbol{t})\ d\Gamma \tag{15}$$

The first term leads to so called “penetration with resistance” boundary condition and is not in the center of our attention in this paper. The second term leads to slip with friction boundary condition and after discretization has the following form:

$$\int_{\Gamma} \left(\boldsymbol{N}^T \boldsymbol{t}\right) \cdot \left(\boldsymbol{t}^T \boldsymbol{N}\right) \, d\Gamma \, \boldsymbol{r}_u \tag{16}$$

where $\boldsymbol{N}$ has the same meaning like before, $\boldsymbol{t}$ is unit tangent vector to the boundary and $\boldsymbol{r}_u$ is unknown nodal vector of velocity.

Discretized problem (8) leads to system of algebraic equation, which can be written in following schematic form:

$$\begin{bmatrix} A(\boldsymbol{u}) & B \\ C & 0 \end{bmatrix} \begin{bmatrix} \boldsymbol{u} \\ p \end{bmatrix} = \begin{bmatrix} \boldsymbol{f} \\ 0 \end{bmatrix} \tag{17}$$

In case, where PSPG stabilization is used, zero blocks are replaced by proper full blocks due to the stabilization. Looking at that scheme, we can say that slip with friction boundary condition gives contribution to block A (in general to each element of that block). The outflow boundary condition contributes to block B.

4. NUMERICAL RESULTS

For numerical testing, flow in 2-D channel across the step was chosen. In this benchmark, the most distinctive feature is recirculating vortex behind the step. In all computations, P1P1 “Taylor-Hood”, linear in both velocity and pressure, triangle element was used. Due to LBB condition, SUPG/PSPG stabilization technique was applied. As a benchmark test, standard two dimensional channel flow test was used. Computational domain is rectangular 2x15. On the left side, constant velocity inflow is prescribed as a Dirichlet boundary condition. On the top and the bottom, slip with friction boundary condition, and on the right side outflow boundary condition is prescribed. In Fig. 1 velocity profile at outflow related to friction coefficient β is shown. It can be seen, that for higher values of β, standard parabolic velocity profile is given. Full friction boundary condition is the limit case. In Fig. 2 there is velocity profile along the boundary with prescribed friction. Velocity near the inflow is higher because of Dirichlet boundary condition. Further from the inflow, one can see declining velocity and convergence to limit velocity corresponding to the level of friction.

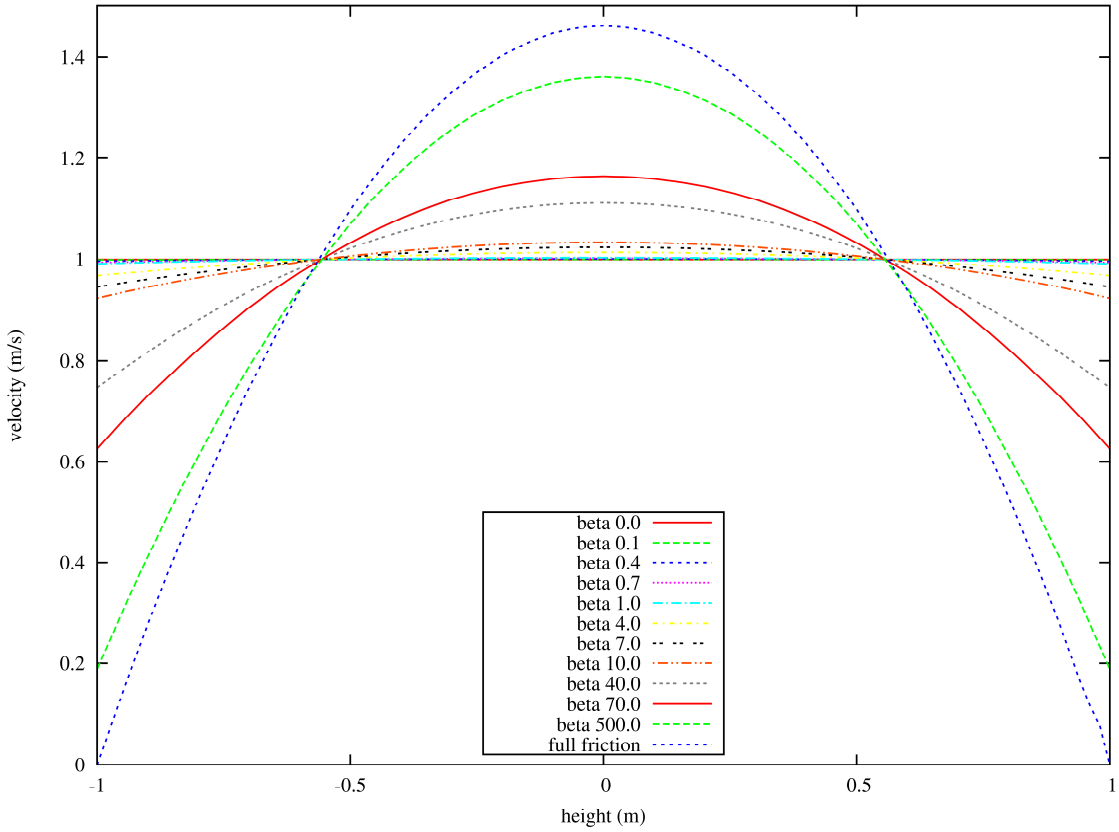

Fig. 1 Velocity profile at outflow boundary.

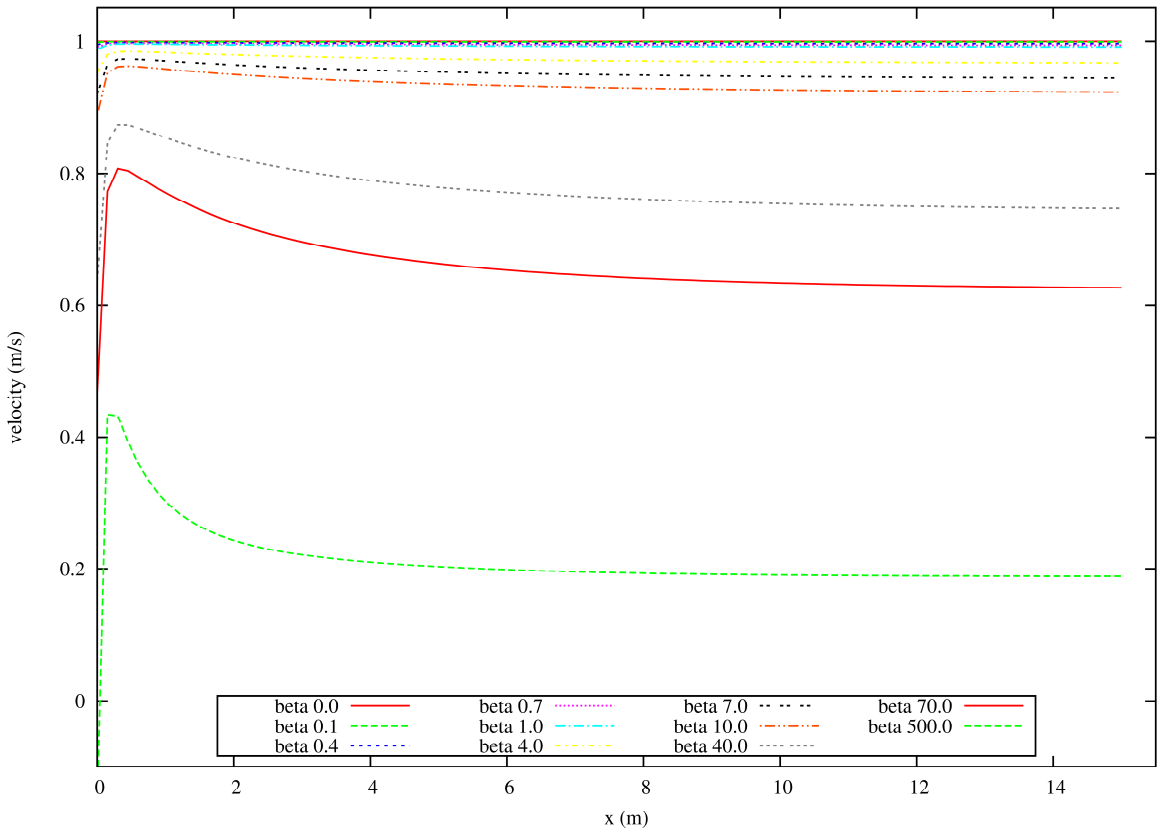

Fig. 2 Velocity at the bottom with "Slip with friction boundary"

ACKNOWLEDGEMENT

This work was supported by the SGS 11/021/OHK1/1T/11 „Advanced algorithms for numerical analysis and modeling"

REFERENCES

[1] DONEA, J.; HUERTA, A. *Finite Element Methods for Flow Problems*. 1st ed. The Atrium Southern Gate, Chichester, West Sussex, PO 19, 8SQ, England : John Wiley & Sons Ltd., 2003. 362 p. ISBN 0471496669.

[2] TEZDUYAR, T.; OSAWA, Y.*: Finite Element Stabilization parameters computed from element matrices and vectors*. Computer Methods in Applied Mechanics and Engineering, Volume 190, Issues 3-4, 27 October 2000, Pages 411-430.

[3] PATZÁK, B.; BITTNAR, Z. *Modeling of fresh concrete flow*. Computers and Structures, 2009, 87 (15), 962-969.

[4] VOLKER, J. *Slip with friction and penetration with resistance boundary conditions for the Navier–Stokes equations—numerical tests and aspects of the implementation*. Journal of Computational and Applied Mathematics, Volume 147, Issue 2, 15 October 2002, Pages 287-300.

[5] GALDI, P., LAYTON, W. *Approximation of the larger eddies in fluid motion ii: a model for space filtered flow*. Math. Models Methods Appl. Sci. 10 (3) (2000) 343-350.

[6] PATZÁK B., BITTNAR Z., *Design of object oriented finite element code.* Advances in Engineering Software, 32(10-11):759--767, 2001.

UP-SCALING MODEL FOR PREDICTION OF MACROSCOPIC ELASTIC PROPERTIES OF ALUMINIUM FOAM

VLASTIMIL KRÁLÍK [1], JIŘÍ NĚMEČEK [2]

Abstract: *This paper is focused on the prediction of macroscopic elastic properties of highly porous aluminium foam. The material is characterized by a closed pore system with very thin pore walls and large air pores. Intrinsic material properties of cell wall constituents are assessed with nanoindentation whereas analytical homogenizations are employed for the assessment of the cell wall elastic properties. 2D microstructural FEM model was applied to obtain effective elastic properties of the whole structure. The Young's modulus was found 0.3-0.6 GPa on the studied material.*

Keywords: *aluminium foam, porous system, nanoindentation, micromechanics, homogenization*

1. INTRODUCTION

Metal foams and especially lightweight aluminium foams belong to the up-to-date engineering materials with high potential to many applications. Metal foam is a highly porous hierarchical material with a cellular microstructure. Macroscopically, it can be characterized by attractive mechanical and physical properties such as high stiffness and strength in conjunction with very low weight, excellent impact energy absorption, high damping capacity and good sound absorption capability. The usual source material for the production of metal foams is aluminium and aluminium alloys because of low specific density (~2700 kg/m^3), low melting point (~660 °C), non-flammability, possibility of recycling and excellent corrosion resistance. Metal foams are used in applications ranging from automotive and aerospace industries (e.g. bumpers, car body sills, motorcycle helmets) to building industry (e.g. sound proofing panels) (see e.g. the review by Banhart **Chyba! Nenalezen zdroj odkazů.**).

[1] Ing. Vlastimil Králík; Czech Technical University in Prague, Faculty of Civil Engineering, Department of Mechanics; Thákurova 2077/7; 166 29, Prague, CZ; vlastimil.kralik@fsv.cvut.cz

[2] Doc. Ing. Jiří Němeček, Ph.D.; Czech Technical University in Prague, Faculty of Civil Engineering, Department of Mechanics; Thákurova 2077/7; 166 29, Prague, CZ; jiri.nemecek@fsv.cvut.cz

Two-scale microstructure based model for the assessment of overall elastic properties on highly porous aluminium foam (Alporas®) is proposed in the paper. The model utilizes the micromechanical approach [2] that is used for the upscaling of mechanical properties (e.g. elastic modulus) on microscopically inhomogenoues composites to the upper level (defined by the representative volume element, RVE). The material can be described as a system with stochastically distributed solid metal phase which forms thin walls (typically ~100 μm thick, Fig. 1b,c) of closed cells (i.e. large pores having typically ~1-13 mm in diameter **Chyba! Nenalezen zdroj odkazů.**, Fig. 1a). The proposed micromechanical model separates the foam microstructure into two levels.

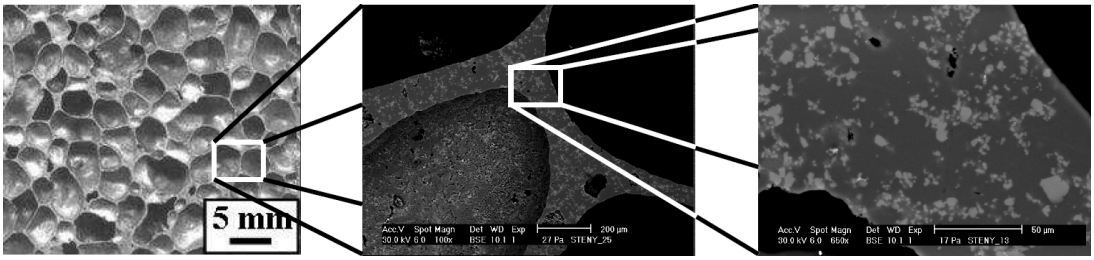

(a) (b) (c)

Fig. 1. (a) Overall view on a typical structure of aluminium foam. (b) ESEM image of a cell wall. (c) Detailed ESEM image of a cell wall showing Ca/Ti-rich area (light zones).

Level 1 (the cell wall level, RVE~100 μm) consists of prevailing aluminium matrix (Al-rich area) with embedded heterogeneities in the form of Ca/Ti-rich areas.

Level 2 (the foam level, RVE~20 mm) includes the Level 1 and large pores (average diameter ~2.6 mm).

2. ESEM AND MICROSTRUCTURAL ANALYSIS

The microstructure of the cell wall was studied in electron microscope (ESEM). Two distinct phases, visible as differently colored areas in ESEM images were distinguished (Fig. 1c). The chemical composition of the two phases was checked with EDX element analysis in ESEM. As expected, the majority of the volume (dark zone) was composed of aluminum and aluminium oxide Al_2O_3 (further denoted as Al-rich area). Lighter zones contained significant amount of calcium and titanium (further denoted as Ca/Ti-rich area). The non-uniform distribution of these zones shows on inhomogeneous mixing of the admixtures that are added during the production process.

3. NANOINDENTATION

Intrinsic elastic properties of the microstructural constituents were assessed by statistical nanoindentation at this level. The tests were performed using a Hysitron Tribolab system® at the CTU in Prague [3].

Elastic moduli were evaluated for each individual indent. Overall results are depicted in Fig. 2a in which histogram of all elastic moduli from two different positions and results merged from both positions are shown. No significant differences between the positions were found. Therefore, merged results were further used for the deconvolution [4] of elastic properties. It can be seen in Fig. 2b that a significant peak appears around 60 GPa. This value can be considered as a dominant characteristic of a solid phase (Al-rich). Tab. 1 contains numerical results from the deconvolution with the estimated volume fractions of the phases.

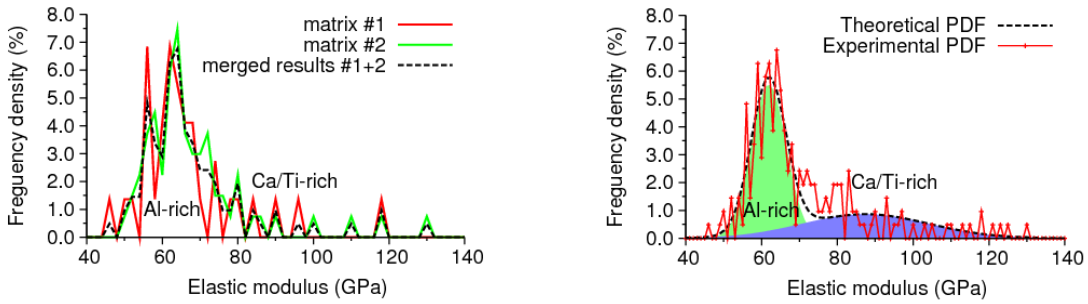

(a) (b)

Fig. 2. (a) Probability density functions of elastic moduli from two measured positions and merged. (b) Deconvolution of elastic moduli in two phases (Al-rich and Ca/Ti-rich).

Tab. 1. Elastic moduli and volume fractions from deconvolution

Phase	Mean (GPa)	St. dev. (GPa)	Volume fraction (-)
1 (Al-rich zone)	61.883	4.618	0.638
2 (Ca/Ti-rich zone)	87.395	16.684	0.362

The characteristic value for the first phase roughly corresponds to the elastic modulus of pure aluminium (70 GPa, ref. [4]). The lower value obtained from nanoindentation suggests that probably some small-scale porosity or impurities (Ca) added to the molten are intrinsically included in the results of this phase. The value of Al-rich zone is also in excellent

agreement with the value 61.7 GPa measured by Jeon et al. [6] on melted Al-1.5 wt.%Ca alloy.

4. LEVEL 1 HOMOGENIZATION

Based on these results, effective elastic properties (Young's modulus) of the solid phase were evaluated by selected analytical homogenization schemes, namely Voigt and Reuss bounds, Mori-Tanaka method and self-consistent scheme [2]. The homogenized elastic modulus for the cell wall is summarized in Tab. 2. Very close bounds and insignificant differencies in the elastic moduli estimates by the schemes were found.

Tab. 2. Effective values of Young's modulus by different homogenization schemes

Homogenization technique	Mori-Tanaka	Self-consist. scheme	Voigt bound	Reuss bound
Young's modulus Level 1 [GPa]	70.076	70.135	71.118	69.195

5. LEVEL 2 HOMOGENIZATION

At first effective elastic properties of Level 2 were estimated with the same analytical schemes used in Level 1. In this level, cell walls are considered as homogeneous having the properties that come from the Level 1 homogenization. The large pores were considered as inclusions in this homogenization. The volume of large pores was assessed as 91.4 % by weighing. The homogenized elastic modulus for the Level 2 structure is summarized in Tab. 3. It is clear that the analytical methods do not give appropriate results, because the basic assumptions following from Eshelby's solution of an ellipsoidal inclusion in an infinite body and volume fraction restrictions are not fulfilled. Nevertheless, the correct solution should lie between Voight and Reuss bounds that are, of course, quite distant (Tab. 3). Both Mori-Tanaka and self-consistent schemes tend to reach lower stiffness value of E (the air) due to the very large volume fraction of pores.

At second, more appropriate two dimensional microstructural FEM model was applied. The model geometry was generated from high resolution optical images of Al-foam (Fig. 3a) in which pore centroids were detected. From these points, Voronoi cells using Delaunay triangulation and equivalent 2D-beam structure were generated (Fig. 3b). As a first estimate, uniform cross-sectional area was prescribed to all beams. Homogenized elastic modulus reached 0.3-0.6 GPa in this model (Tab. 3) depending on the RVE boundary conditions. Such

result is in good agreement with the range of experimental values (0.4-1 GPa) reported for Alporas® e.g. by Ashby et. al. [7].

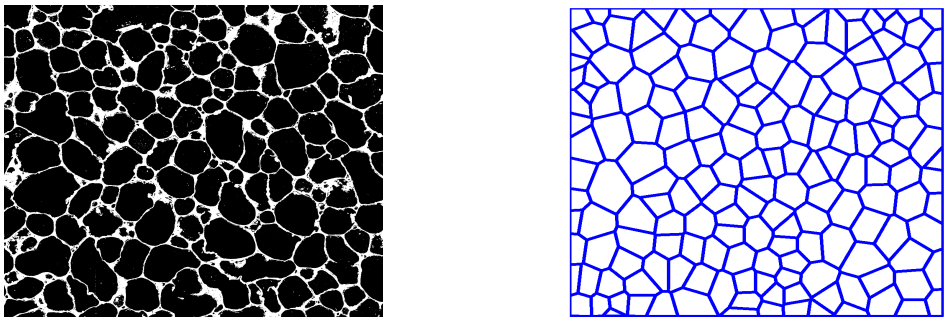

(a) (b)

Fig. 3. (a) High resolution optical image of Al-foam. (b) 2D-beam structure.

Tab. 3. Effective values of Young's modulus by different homogenization schemes

Homogenization technique	Mori-Tanaka	Self-consist. scheme	Voigt bound	Reuss bound	Numerical
Young's modulus Level 1 [GPa]	3.151	0.001213	6.02	0.00109	0:3 - 0:6

6. CONCLUSION

Micromechanical elastic properties of Al-foam (Alporas®) cell wall constituents were obtained through statistical nanoindentation and deconvolution techniques. Analytical homogenization schemes showed very similar results of effective cell wall elastic properties (Level 1 - E_{eff}≈70 GPa).

This microscale parameter together with corresponding volume fractions of cell walls and large pores were used in micromechanical up-scaling to the upper level. Effective elastic properties of Level 2 were estimated with the same analytical schemes used in Level 1. The analytical methods do not give appropriate results. Therefore more appropriate two dimensional microstructural FEM model was applied. Homogenized elastic modulus of this FEM model reached 0.3-0.6 GPa. This values are in good agreement with other range of experimental values obtained by conventional methods. Further development of the numerical model (influence of boudary conditions, RVE size, extension to 3D) and extending an experimental program is planned in the future.

ACKNOWLEDGEMENT

Support of the GAČR (P103/09/1748) and CTU in Pragu (SGS10/135/OHK1/2T/11) is gratefully acknoledged

REFERENCES

[1] Banhart J., 2001. *Manufacture, characterisation and application of cellular metals and metal foams*, Progress in Materials Science, Vol. 46, No. 6, pp. 559-632, ISSN 0079-6425.

[2] Zaoui A., 2002. "*Continuum Micromechanics: Survey*", Journal of Engineering Mechanics, Vol. 128, No. 8, pp. 808-816, ISSN 0733-9399.

[3] Králík V., Němeček J., 2011. *Nanoindentation based evaluation of effective elastic properties of metal foam,* In proceedings of Engineering Mechanics 2011, Svratka, Czech Republic, pp. 315-318.

[4] Němeček J., Šmilauer V. & Kopecký L., 2011. *Nanoindentation characteristics of alkali-activated aluminosilicate materials*, Cement and Concrete Composites, Vol. 33, No. 2, pp.163-170, ISSN 0958-9465.

[5] http://www.webelements.com

[6] I. Jeon et al., 2009. "*Cell wall mechanical properties of closed-cell Al foam*", Mechanics of Materials, Vol. 41, No. 1, pp. 60-73, ISSN 0167-6636.

[7] Ashby M. F., Evans A., Fleck N. A., Gibson L. J., Hutchinson J. W., Wadley H. N., 2002. *Metal Foams: A Design Guide***,** Materials & Design, Vol. 23, No. 1.

APPROXIMATION-BASED APPROACHES TO IDENTIFICATION OF MATERIAL MODEL PARAMETERS

TOMÁŠ MAREŠ[1], ANNA KUČEROVÁ[2],

Abstract: *Increasing complexity of material models requires increasing efficiency and robustness of identification strategies. The presented contribution presents a comparison of several different approaches to parameters identification based on artificial neural networks or genetic programming.*

Keywords: *parameter identification, model approximation, neural networks, genetic programming, microplane model M4*

1. INTRODUCTION

Numerical modeling of material behavior includes the problem of parameter identification. This problem may be quite complex, because some parameters may not have easy physical interpretation. There are two ways of parameter identification – forward and inverse [1].

In forward identification the task is to find a set of parameters minimizing the difference between model output and experimental data using some optimization technique. The difficulties arise from the complexity of the model and the corresponding objective function leading to time consuming process. To overcome this problem, one may employ some computational*l*y cheaper approximation of the numerical model.

The presumption for inverse parameter identification is based on the existence of an inverse relation between model inputs and outputs. However, the validity of such presumption cannot be guaranteed generally, but can be justified at bounded parameter domain. Then *the* task is to find *an* approximation of this relation.

[1] Tomáš Mareš; Czech Technical university in Prague, Faculty of Civil Engineering, Department of Mechanics ; Thákurova 7, 16629 Prague, Czech Republic; tomas.mares.1@fsv.cvut.cz

[2] Ing Anna Kučerová PhD; Czech Technical university in Prague, Faculty of Civil Engineering, Department of Mechanics ; Thákurova 7, 16629 Prague, Czech Republic; anicka@cml.fsv.cvut.cz

2. NEURAL NETWORKS

Neural network (NN) is a simplified mathematical model of nervous system. It consists of computational units (neurons) connected by a prescribed rule, connections (synapses) are weighted, so the neural network can be seen mathematically as a oriented weighted graph. In our experiments, we used a full-connected, feed-forward, multilayer neural network, where the neurons are organized into layers. The first and the last layer correspond to the input and output vectors respectively. The layers in between are called as hidden layers. Every neuron from one layer is connected to every neuron in the following one. In particular, we used only one hidden layer, because it was proved, that one hidden layer with enough neurons is sufficient to achieve universal approximation property [2]. The activation function of hidden neurons employed in our implementation was a logistic sigmoid :

$$o_{\text{hidden}} = \text{sig}(\xi) = {}^{1}/_{(1 + \exp(-\xi))} \tag{1}$$

where inner potential - $\xi = \sum_{i=0}^{i=n} w_i\, o_i - b$ - is a sum of neuron inputs weighted by synaptic weights (w_i) and b denotes bias, While in case of the output neuron the identity function : $o_{\text{output}} = \xi$ seemed to be sufficient.

In order to determine the number of hidden neurons, we propose simple adaptation algorithm. It starts with a arbitrarily chosen small number and repeatedly increases by one while the error measured on validation data set decreases by specified speed, i.e.

$$E_{(t)}/E_{(t-1)} < 0.9 \tag{2}$$

where terms $E_{(t-1)}$ and $E_{(t)}$ denote validation error before and after increasing this number respectively.

Input synaptic weights were initialized by Nguyen-Widrow method [3], output weights were initialized by uniform distributed random numbers from interval (-1, 1). The optimization of the synaptic weights is governed by the nonlinear conjugate gradients method. Three individual weights initializations and optimization runs were performed for each NN architecture. All inputs and outputs were scaled to interval (-1, 1) The resulting method was implemented in C++.

3. GENETIC PROGRAMMING

The idea of genetic programming is based on an automatic development of program in a tree form composed of predefined primitives (nodes), using natural selection from population of programs based on defined objective (or fitness) function and genetic operators - (for more information see [4]) . In the case of search for model approximation, the primitives are operators ('+', '-', '*') with the arity egual to two, functions (sin(), logistic sigmoid(), cos(), tanh()) with the arity equal to one, and terminals (x_1, x_2, ….., x_n, constant) with the zero arity. Constants were initialized using uniformly distributed random numbers from interval (-10, 10). The goal is to find an appropriate mathematical expression for given data. To simplify and speed up the computation we tried to search the expression in a form :

$$a * F + b \tag{3}$$

where F denotes the expression build by genetic programming, a and b are constants determined by simple linear regression. Fitness function was defined by following formula :

$$E = \frac{1}{n} \sum_i (O_i - D_i)/(D_{max} - D_{min}) \tag{4}$$

where O_i and D_i stand for an output of given expression obtained for the i.th learning example and the corresponding desired output, respectively. n is the number of examples and $(D_{max} - D_{min})$ compensates the data standardization. The fitness function can be interpreted as an error relativ to the output interval range. The same function is also used as an NN error measure in order to estimate approximation performance. We employed following genetic operators : crossover (switching two randomly chosen subtrees from two selected members of the population), mutation (regenerating subtree of a selected population member), local mutation (replacing node in a chosen tree with another one having the same arity), and edit (replacement of constant subtrees with one constant terminal).

Table 1 – parameters of genetic programming

Crossover probability	0.33
Mutation probability	0.33
Local mutation probability	0.33
Population size	1000
Selection mechanism	Tournament (n = 4)
Fitness evaluation limit	100000
Maximal depth of expression tree	12

The resulting algorithm was also implemented in C++ language.

4. IDENTIFICATION OF MICROPLANE M4 PARAMETRS

Microplane model M4 [5] is a complex 3D numerical model for concrete allowing for description of tensional and compressive softening, damage of the material, different combinations of loading, unloading and cyclic loading, also the development of anisotropy within the material. Disadvantages of this model lay in enormous computational cost and unclear physical interpretation of the most of its parameters. Therefore a robust procedure for parameters identification is on demand. Some work on parameters estimation of microplane model M4 in the inverse fashion was already presented, e.g. in [1] and [6].

We focused on parameters E, k1 and c20, which should be identified from the uniaxial compression test. We used the simulation of uniaxial compression of concrete cylinder with 150 mm diameter and 300 mm height. Output of the model was a stress – strain diagram, described by a set of 18 discrete points at prescribed strain values. 70 simulations were performed for randomly chosen sets of material parameters, 60 input – output vector were used for training of neural network/genetic programming, the rest of them for a validation.

In the case of forward identification the goal is to approximate the microplane model in order to replace its time consuming evaluations by fast evaluation of NN or GP during the optimization process. Two approaches to this task were considered. In the first one (A), we tried to approximate the whole microplane model, i.e. the mapping $\mathrm{E}, \mathrm{k1}, \mathrm{c20}, \nu, \varepsilon \dashrightarrow \sigma$. In the second scenario (B), we tried to find 18 separate functions for 18 predefined values of strain, so the desired approximations correspond to mapping : $\mathrm{E}, \mathrm{k1}, \mathrm{c20}, \nu \overset{\varepsilon}{\rightarrow} \sigma$. We have presumed that this procedure would lead to simpler functions i.e. easier architecture, faster optimization of neural networks weights, lesser depth of trees in case of genetic programming and finally greater precision.

NN adaptation started with 10 and 3 hidden neurons in procedure A and B, respectively. In the first scenario, the resulting number of hidden neurons reminded the same, while in the second one varied between 3 and 9 neurons. For each approach, ten different approximations were constructed and used for identification of ten different strain – stress diagrams. The minimization of differences between the testing and predicted data (measured by Euclidian distance) was governed by the GRADE algorithm with CERAF strategy (for more detail see [1]). The results of forward parameter identification are summarized in table 2.

Table 2 – forward identification results

approx. method	error of parameter identification [% of interval range]								
	E			k1			c20		
	min.	av.	max.	min.	av.	max.	min.	av.	max.
GP – A	0.019	12.3	46.2	0.03	10.5	30.6	1.24	44.6	116
NN - A	0.11	7.95	41.0	0.29	7.40	31.7	0.63	26.2	84.5
GP - B	0.0013	0.82	4.22	0.009	1.97	5.49	0.034	23.8	84.2
NN - B	0.0013	0.37	1.29	0.062	1.24	3.41	0.11	11.1	54.7

It is obvious that the approximation of the whole microplane model in the scenario A and the corresponding parameter identification did not provide the parameter estimates with satisfactory precision. In the case of 18 separate functions were results much better, it was possible to identify parameters E and k1 with less than 2% precision error. However determination of c20 remained impossible. NN was a bit more precise, but the difference between both approximation methods was not significant.

Approximation of inverse relation should directly provide desired parameter estimate using all 18 stress values (microplane M4 output) as the input. Since there is a redundancy among all these values, so input space dimension of approximation can be reduced by computing Pearson correlation coefficient between each parameter and stress value in given point of diagram and choosing only most influential values of stress, see Table 3. (Detailed results of this procedure can be found in [1]).

Table 3 – inverse relations inputs and outputs

Parameter	Inputs
E	$\sigma_1, \sigma_2, \sigma_3$
k1	$\sigma_5, \sigma_{18}, \sigma_{\mathrm{peak}}, \varepsilon_{\mathrm{peak}}, \mathrm{E}_{\mathrm{predict}}$
c20	$\sigma_6, \sigma_8, \sigma_{12}, \sigma_{16}, \mathrm{E}_{\mathrm{predict}}, \mathrm{k1}_{\mathrm{predict}}$

In the case of inverse mapping approximation started NN adaptation with one hidden neuron, resulting numbers of hidden neurons were 5, 4 and 3 for parameters E, k1 and c20,

respectively. NN started to overfit soon in the case of inverse identification of c20. See table 4 for summarized inverse parameter identification results.

Table 4 – inverse identification results

approx. method	inverse mapping approximation error [% of interval range]								
	E			k1			c20		
	min.	av.	max.	min.	av.	max.	min.	av.	max.
GP	0.520	0.522	0.523	1.01	1.37	1.88	21.90	21.91	21.95
NN	0.298	0.340	0.387	0.849	0.860	0.876	22.13	22.43	22.94

It may be seen, that parameters E and k1 were identified more precise than in the case of forward identification. Differences between forward identification B and inverse identification are not very significant and both these approaches can be recommended for a practical usage. On the other hand, no need for optimization process being a potential source of additional errors an consuming more computational time is an important advantage of the inverse approach.

The attempt to estimate c20 was not very successful. The importance of this parameter for uniaxial compression test and possibilities to identify it only from this experiment is up to further discussion.

5. CONCLUSION

- Both GP and NN can provide useful approximation. NN tends to be a bit more precise than GP. The drawback of NN is nontrivial choice of hidden neurons number.
- In the case of forward approach, one may obtain reliable parameter estimates using approximations of stress-strain diagram in predefined points. However, neither NN nor GP were unable to achieve useful approximation of the whole microplane M4 model.
- Microplane model M4 parameters E and k1 can be estimated with satisfactory precision using appropriate method. All proposed methods of identification failed in the case of parameter c20. This may be caused by using only data from uniaxial compression test.

ACKNOWLEDGEMENT

This outcome has been achieved with the financial support of the Czech Science Foundation, project No. 105/11/P370.

REFERENCES

[1] Kučerová A. 2007. *Identification of nonlinear mechanical model parameters based on sofcomputing methods,* Ph.D. thesis, Ecole Normale Supérieure de Cachan, Laboratoire de Mécanique et technologie.

[2] Horník K., Stinchcombe M., White H. 1989. *Multilayer feedforward networks are universal approximators,* Neural Networks, vol 2.

[3] Nguyen D., Widrow B. *Improving learning speed of 2-layer neural network by choosing initial values of adaptive weights,* technical report, Information Systems Laboratory, Stanford University.

[4] Koza J. R. 1992. *Genetic Programming: On the Programming of Computers by Means of Natural Selection.* MIT press.

[5] Bažant Z. P., Caner F. C., Carol I., Adley M. D., Akers S. A. 2000. *Microplane model M4 for concrete. Part I: Formulation with work-conjugate deviatoric stress, Part II: Algorithm and calibration,* Journal of Engineering Mechanics, vol 126, no. 9

[6] Kučerová A., Lepš M., Zeman J. 2007. *Back analysis of microplane model parameters using soft computing methods,* CAMES: Computer Assisted Mechanics and Engineering, vol 14, no. 2

DEVELOPMENT OF CEMENT PASTES HYDRATION HEAT: EFFECT OF A PVA NANOTEXTILES AS SURFACE LAYERS

RYPAROVÁ PAVLA[1], TOMÁŠ NÉMETH[2], JAN MUKAŘOVSKÝ[3], PAVEL TESÁREK[4]

Abstract: *The article deals with the effect of nanofiber use as a surface treatment of cement pastes. There is interesting and promising field of nanofiber application in building industry as the surface treatment with specific properties. Such a treatment can affect the hydration process of cement based materials. Suitably designed nanofiber can prevent or limit water vaporization from the surface during cement hydration and so affect the final mechanical properties (strength) of cement based materials. In the article, there is investigated the effect of nanofibers with different weight per unit area applied on cement pastes made from CEM I 42.5 R (wet) cement. Finally, the mechanical properties (compressive strength and tensile strength in bending) and weight decrease (related to water vaporization from the test samples) were assessed.*

Keywords: *Nanofibers, cement paste, mechanical properties, hydration processes,*

1. INTRODUCTION

The effect of the hydration processes in wet concrete on final properties, that are typically represented by the mechanical properties above all, is frequently discussed topic nowadays. From the very beginning of wet concrete design, there are several parameters (water to cement ration, cement type, filler and his granulometry, amount and type of aggregate, etc.) to be

[1] Mgr. Pavla Ryparová; Czech Technical University in Prague, Faculty of Civil Engineering; Thákurova 7, 166 29 Prague 6, Czech Republic; pavla.ryparova@fsv.cvut.cz.

[2] Ing. Tomáš Németh; Czech Technical University in Prague, Faculty of Civil Engineering; Thákurova 7, 166 29 Prague 6, Czech Republic, tomas.nemeth@fsv.cvut.cz.

[3] Ing. Jan Mukařovský, Ph.D.; Czech Technical University in Prague, Faculty of Civil Engineering; Thákurova 7, 166 29 Prague 6, Czech Republic; jan.mukarovsky@fsv.cvut.cz.

[4] Ing. Pavel Tesárek, Ph.D., Czech Technical University in Prague, Faculty of Civil Engineering; Thákurova 7, 166 29 Prague 6, Czech Republic; jan.mukarovsky@fsv.cvut.cz.

optimized to get the concrete that meets all the requirements, nowadays oriented namely to the durability of concrete structure. Every concrete structure has to meet further specific requirements and parameters that are related to e.g. structure size, its location in the building, or the way of treatment [1].

The hydration process itself can be determined resp. is related to ambient environment, where the temperature is the predominant parameter. Further, the effect of water vaporization from the not covered structure surfaces is also of a high importance. At this point, there are several ways how to protect especially the horizontal surfaces of concrete structures during the hardening and solidification process in wet concrete. The reason is to prevent the surface from cracking that enables water penetration near the steel reinforcement and its degradation thus the degradation of the whole reinforced concrete structure [2], [3].

As one of the easiest ways for surface protection there is used complete covering or protection of horizontal surfaces (reinforced concrete floors) by using plastic foils or different spray application or coating that should prevent from excessively high water vaporization [4], [5]. The water vaporization, together with further effects, can affect also the development of hydration heat inside the concrete components that is considerable especially in massive reinforced concrete components [6]. As an alternative to the above mentioned ways, there can be used very thin protective layer based on nanofibers that are being widely used in different industrial branches nowadays. Using electrospinning method, it is possible to produce nanofibers that have specific material properties that can be continually modified according to the need during production. Such a nanofibers can suitably moderate the vaporization. The nanofiber sheets (produced in width of up to 4 m) could be unrolled on wet surface of newly layed concrete structure.

2. MATERIALS AND SAMPLES

The testing of temperature distribution during development of hydration heat was done on cement paste cubes with dimensions of 100x100x100 mm. The cubes were cast into the mould where the mould was functioning also as thermal insulation. This way, there were modeled half-infinite ambient conditions. The moulds were made of extruded polystyrene (Styrodur 3035 CS) supporting the sample cubes on five sides. The temperature distribution was measured with digital temperature sensors placed along vertical axis of the cubes. The sensors are working in operative range from -10 to +85 °C with accuracy of ± 0.5 °C.

The nanofibers were spun in different weights per unit area (0.1; 5 and 10 g/m^2) especially for this testing. The used polyvinyl alcohol (PVA) nanofibers can be spun approx. up to 5 g/m^2 in one layer, higher weights per unit area are spun in two (up to 10 g/m^2) or more layers. Extremely fine nanofibres can´t exist independently they need a kind of support, a material that would assure sufficient mechanical resistance. These nanofibers were spun on polymeric support textile (spunbond). The PVA nanofibres itself are very instable and dissolves when in touch with water. That is way the polymer have to be stabilized by adding of suitable heat activated catalytic agent. After heating up (10 minutes at 140 °C) the polymeric nano structure becomes stable.

3. EXPERIMENTAL RESULTS

The measured results are presented on Fig. 1 and 2. Fig. 1 shows the temperature distribution on referent A sample cubes from cement paste (without additional treatment). Fig. 2 shows the temperature distribution on B sample cubes where the upper side of the cube were covered with nanofiber (10 g/m^2). Comparing both temperature distributions, it is clear that the B sample cubes with nanofibre surface treatment had major temperature growth of up to approx. 5 °C for every time step and temperature sensor position. Further, from the observation of cement paste surface, it is visible that the nanofiber “grew into” the surface and became its component. Separating of these layers requires “a certain” force for ripping off. Contrary to this “growing into” the spunbond can be separated from the “grown into” nanofiber cleanly and easily.

4. CONCLUSIONS

The article is dealing with an experimental use of PVA nanofibers applied on wet surface of cement paste. The positive result is the nanofiber “growing into” the wet surface of cement paste above all. Also the effect of major temperature growth in B sample cubes with nanofiber treatment is not negligible.

ACKNOWLEDGEMENT

This outcome has been achieved with the financial support of the Ministry of Education, Youth and Sports of the Czech Republic, project No. 1M0579 – CIDEAS.

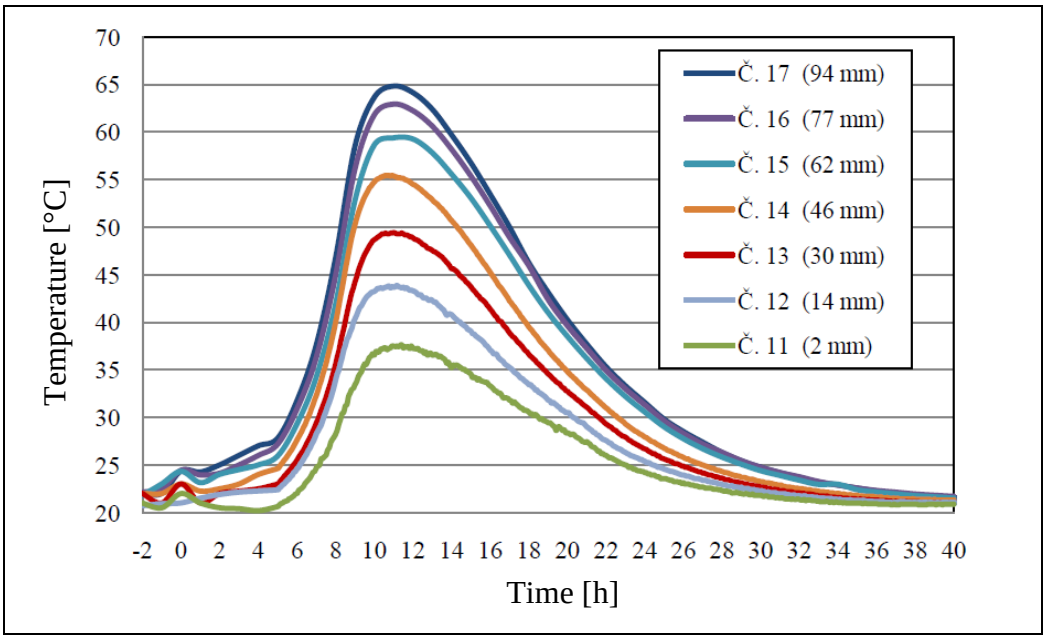

Fig. 1. Temperatures distribution in samples A

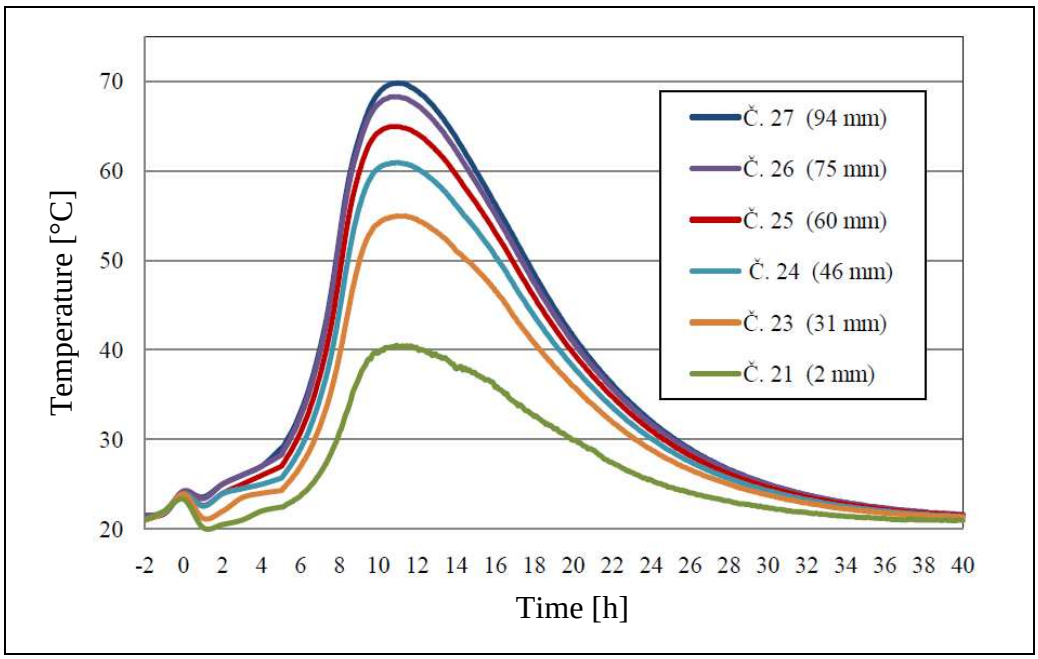

Fig. 2. Temperature distribution in samples B

REFERENCES

[1] Němeček, J., Šmilauer, V., Kopecký, L. 2009, *Characterization of Alkali-activated Fly-ash by Nanoindentation*, In: Proceedings of the Nicom3 – Nanotechnology in Construction 3. Berlin: Springer-Verlag, 2009, p. 337-343. ISBN 978-3-642-00979-2.

[2] Tydlitát, V., Tesárek, P., Černý, R., 2008, *Effects of the Type of Calorimeter and the Use of Plasticizers and Hydrophobizers on the Measured Hydration Heat Development of FGD Gypsum*, In: Journal of Thermal Analysis and Calorimetry. vol. 91, no. 3, p. 791-796. ISSN 1388-6150.

[3] Tesárek, P., Wilczynská, A., Korecký, T., Padevět, P., 2010, *Mechanical Properties of Gypsum Blocks after Fire***,** In: Experimentální Analýza Napětí 2010. Olomouc: Palacky University, 2010, vol. 1., p. 431-434. ISBN 978-80-244-2533-7.

[4] Padevět, P., Wilczynská, A., Tesárek, P., 2010, *Determination of Compressive and Bending Strength of Hardened Gypsum***,** In: Experimentální Analýza Napětí 2010. Olomouc: Palacky University, 2010, p. 301-305. ISBN 978-80-244-2533-7.

[5] Hájková, A., Padevět, P., Plachý, T., Němcová, H., Tesárek, P., 2011, *Study of FGD Gypsum Mechanical Properties – Before and After Recycling*, In: Experimentální analýza napětí 2011. Brno: Brno University of Technology, 2011, p. 79-84. ISBN 978-80-214-4275-7.

[6] Tesárek, P., Mraček, T., Padevět, P., 2010, *Material Properties ag a Gypsum Block Exposed to Influence of Weather***,** In: Experimentální Analýza Napětí 2010. Olomouc: Palacky University, 2010, p. 427-430. ISBN 978-80-244-2533-7.

DETERMINATION OF DYNAMIC PROPERTIES OF ASPHALT CONCRETE USING THE RESONANCE METHOD

HANA NĚMCOVÁ [1], TOMÁŠ PLACHÝ [2], ANDREA HÁJKOVÁ [3], JIŘÍ VAVŘIČKA [4]

Abstract: *The paper presents the determination of mechanical properties of asphalt concrete used in layers of pavement. The resonance method was used for determination of dynamic Young´s modulus and dynamic shear modulus of the asphalt concrete. These properties were determined twice in different temperatures: 0 ºC and 20 ºC. The resulting values of the properties were compared and discusssed.*

Keywords: *asphalt concrete, resonance method, dynamic Young´s modulus*

1. INTRODUCTION

Assessment of asphalt concrete in terms of dynamic modulus of elasticity and the development of new asphalt concrete for optimum performance are activities which require increased need for finding new methods that will lead to verify the dynamic properties of course layer pavement.

In this case the resonance method was used. Each sample of solid material vibrates after giving a mechanical impulse. The value of the resonant frequency is dependent on the dimensions of the specimen, its density and Young´s modulus. Based on these physical relations, the dynamic Young´s modulus and dynamic shear modulus were determined.

[1] Ing. Hana Němcová, DiS.; Department of Mechanics, Faculty of Civil Engineering, Czech Technical University in Prague, Thákurova 7, 166 29 Prague 6, Czech Republic;hana.nemcova@fsv.cvut.cz

[2] Ing. Tomáš Plachý, Ph.D.; Department of Mechanics, Faculty of Civil Engineering, Czech Technical University in Prague, Thákurova 7, 166 29 Prague 6, Czech Republic; plachy@fsv.cvut.cz

[3] Ing. Andrea Hájková; Department of Mechanics, Faculty of Civil Engineering, Czech Technical University in Prague, Thákurova 7, 166 29 Prague 6, Czech Republic; hop.hop@seznam.cz

[4] Ing. Jiří Vavřička; Department of Road Construction, Faculty of Civil Engineering, Czech Technical University in Prague, Thákurova 7, 166 29 Prague 6, Czech Republic; jiri.vavricka @fsv.cvut.cz

2. MATERIALS AND SPECIMENS

The experiment used 4 samples of asphalt concrete, ACO 16 + with dimensions of 40 x 40 x 170 mm. Specimens were cut from the plate-type test, which was prepared with the shock compaction energy 2 x 50 shots [1]. The mixture consists of non-recycled aggregate [2] with a nominal grain size of up to 16 mm- grain line (Figure 1) and was used as a binder asphalt 50/70 with a total binder content of 5.3 % by weight [3]

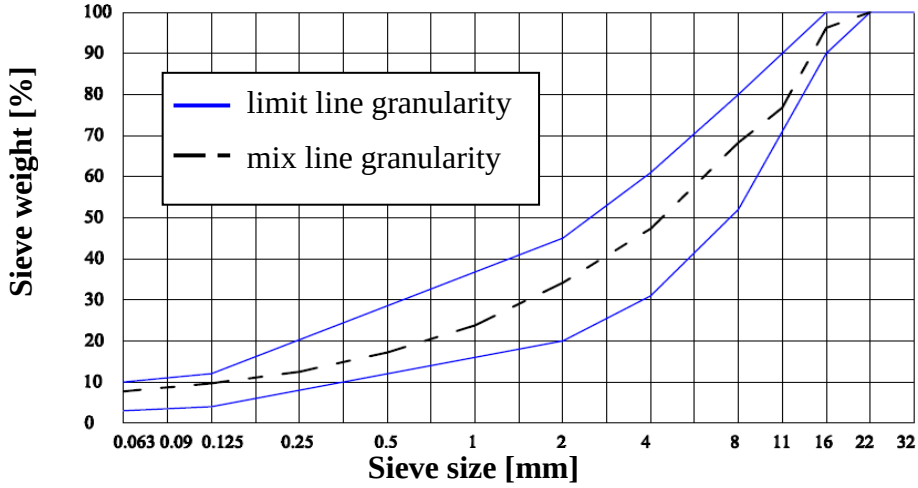

Fig. 1. Grading curve

3. IMPULSE EXCITATION METHOD

The test procedure was performed in accordance with ASTM C215 [4] and with ČSN EN 14146 Natural stone test methods – Determination of the dynamic modulus of elasticity [5]. Principle of this method lies in the oscillation of the specimen using the longitudinal, bending and torsional vibrations. In the next chapters there are mentioned the corresponding relations for calculations of the dynamic Young´s modulus and dynamic shear modulus based on the fundamental resonance frequencies.

3.1 DYNAMIC MODULUS OF ELASTICITY

The fundamental natural frequency of longitudinal vibration F_L [Hz] was determined as the basic resonant frequency of the Frequency Response Function (FRF). The dynamic Young´s modulus Ed_L [MPa] can be determined using the relation:

$$Ed_L = 4 \cdot 10^{-6} \cdot l^2 \cdot F_L^2 \cdot \rho \qquad (1)$$

where l [m] is the length of the specimen, ρ [kg/m^3] is the density of the specimen, F_L [Hz] is the fundamental natural frequency of the longitudinal vibration of the specimen.

3.2 DYNAMIC SHEAR MODULUS

The first torsional resonant frequency was evaluated using the same procedure as the above described longitudinal one. The dynamic shear modulus G_d [MPa] can be determined based on the equation

$$G_d = 4 \cdot 10^{-6} \cdot l^2 \cdot F_T^2 \cdot \rho \cdot R \qquad (2)$$

where l [m] is the length of the specimen, ρ [kg/m^3] is the density of the specimen, F_T [Hz] the fundamental torsional resonant frequency of the specimen, R is correction factor dependent on the width-to-thickness ratio of the specimen (the prism-shaped specimen is R = 1.183).

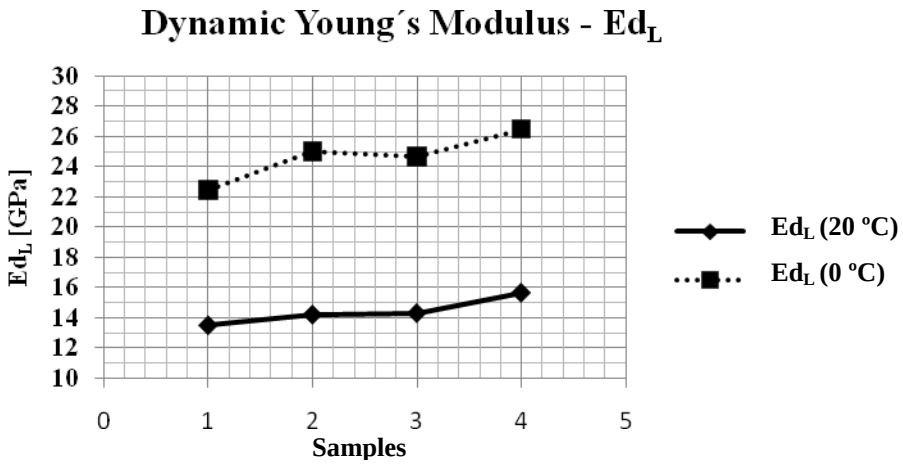

Fig. 2. Dynamic Young´s modulus Ed_L determined based on the basic longitudinal resonant frequency

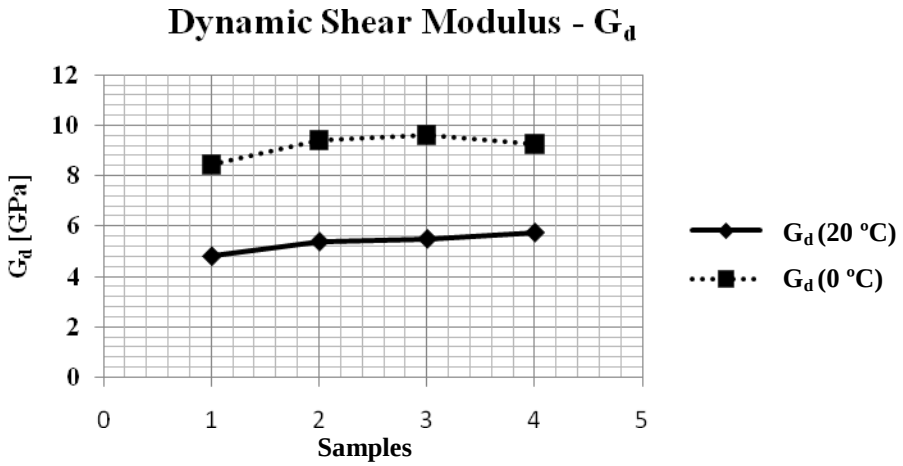

Fig. 3. The dynamic shear modulus G_d determined based on the torsional resonant frequency

4. RESULTS

Samples were subjected to the resonance method at two temperatures. The samples were measured at the laboratory temperature of 20 (±2) Cº and then they were placed in the freezer box (0 Cº) for 12 hours. After removing, the measurements were repeated.

The resulting values of dynamic Young´s modulus (Fig. 2.) and dynamic shear modulus (Fig. 3) increased almost twice due to temperature. This is mainly due to the properties of asphalt binder, which is stiffer with decreasing temperature.

5. CONCLUSION

Test measuring the dynamic modulus of elasticity can be beneficial in the file significant test methods in assessing the design of asphalt mixtures. Its advantages are simplicity and repeatability of measurements at different temperatures on the same samples. The measurement results are affected by the size of aggregates and the binder amount in the sample. Although the measurement was done only on a small group of samples, we can say that this method will be used for more samples. The measurements obtained at the given conditions are approaching values of proven methods.

ACKNOWLEDGEMENT

This work has been supported by grant CTU under No. SGS10/136/OHK1/2T/11, Advanced experimental methods.

REFERENCES

[1] ČSN EN 12697-30, *Bituminous mixtures – Test methods for hot mix asphalt – Part 30: Specimen preparation by impact compactor.* Praha: Czech Standard Institute, pp. 20, 2007

[2] ČSN EN 13108-1, *Bituminous mixtures – Material specifications – Part 1: Asphalt Concrete.* Praha: Czech Standard Institute, pp. 64, 2008

[3] Type test report No. 136004/ITT/2011. 2011. Faculty of Civil Engineering, CTU in Prague, Faculty of Civil Engineering – experimental centre . pp. 7.

[4] ASTM C215, 2008. *Standard Test Method for Fundamental Transverse, Longitudinal, and Torsional Frequencies of Concrete Specimens*, DOI: 10.1520/C0215-08, pp. 7

[5] ČSN EN 14146, *Natural stone test methods – Determination of the dynamic modulus of elasticity (by measuring the fundamental resonance frequency).* Praha: Czech Standard Institute, pp. 16, 2005

MODELING OF BEHAVIOUR OF FIBERS IN COMPOSITE MATERIALS UNDER CYCLIC LOADING AND UNLOADING

MICHAL PŘINOSIL[1], **PETR KABELE**[2]

Abstract: *This article deals with the behaviour of single fiber in composite materials. For modeling a single fiber's response during pulling from the surrounding matrix is used a new approach, including debonding and pulling-out fibers on both sides of the crack. Unloading and reloading of the fibers may occur during this process. To monitor the behaviour of fibers during loading and unloading, FEM model is created.*

Keywords: *Fiber composite, debonding process, pull-out process, cyclic loading, FEM*

1. INTRODUCTION

Engineered Cementitious Composites (ECC) represent new trend of High Performance Fiber Reinforced Cementitious Composites (HFRCC). This material consists of fine grained cement matrix (mixture of cement, sand, fly ash, water and other additives) and short randomly oriented fibers at average 2 % of volume.

The main ability of ECC is strain hardening behaviour - high tensile strain capacity with range 3-5 % with increasing tensile load. During this process large number of fine cracks is formed with the limited width about 60 – 100 μm and the spacing of several millimeters. This behaviour is so-called "multiple cracking". This property can be used in various applications, where the material has to accommodate large deformation without losing macroscopic integrity or where the limited crack width is required.

ECC is micromechanically designed material. For description of behaviour there is a number of models at different levels. In this article, micromechanical FEM model is used for connection of basic material properties with response of single fiber.

[1] Ing. Michal Přinosil; Czech Technical University in Prague, Faculty of Civil Engineering; Thákurova 7, 166 29, Praha 6, Czech Republic; michal.prinosil@fsv.cvut.cz

[2] Prof. Ing. Petr Kabele, Ph.D.; Czech Technical University in Prague, Faculty of Civil Engineering; Thákurova 7, 166 29, Praha 6, Czech Republic; petr.kabele@fsv.cvut.cz

2. MODELING OF SINGLE FIBER BEHAVIOUR

For description of behaviour of single fiber a number of the analytical relations was derived in the past. In our article we use relation published in [1]. The process of extracting fiber is divided into two phases: the phase debonding of fiber from the surrounding matrix and the phase pulling-out of full debonded fiber. This process is shown in Figure 1.

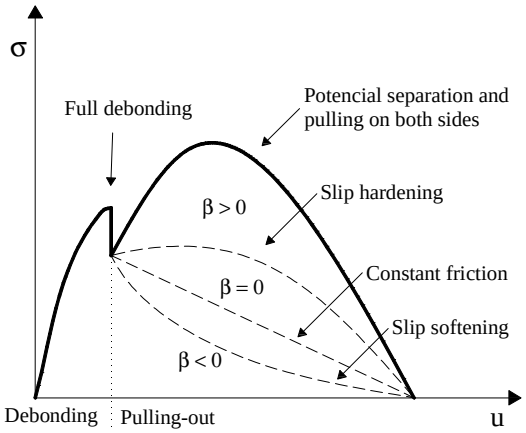

Fig. 1. Single fiber pull-out response

In [2] this model has been extended of possible debonding and pulling-out of the fiber on both sides of the crack. Considering that the embedment lengths on both sides of crack are different, this approach leads to stress drop on both sides of fiber (balance of forces) at full separation of fiber on shorter embedment length and its subsequent pulling out and contraction of fibers at the longer embedment length. Subsequently, the fiber is unloaded during pulling-out, or is reloaded considering the hardening response (Figure 2).

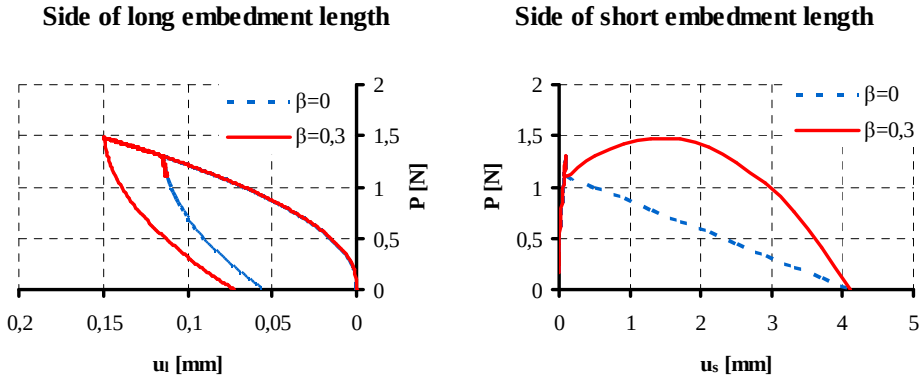

Fig. 2. Response on both sides of fiber

(β = 0 - only unloading, β = 0,3- reloading and unloading)

Because in most cases unloading occurs in the phase of debonding, model is created especially for it.

3. CYCLIC LOADING AND UNLOADING

For the purpose of this article we developed 1D FEM model in the environment of software MATLAB. Frictional forces along the fiber were replaced by nodal loads, which take into account that these forces don't operate, when the node is removed from the matrix. The orientation of these forces on each node is determined by the condition of balance of forces along whole fiber and their orientation changes from the free end to embedment side. Number of elements changes with the length of debonded fiber from the matrix. Separation occurs while exceeding the cohesive strength fibers with a matrix in embedment node (Figure 3). The calculation is controlled by prescribed displacement of the free end.

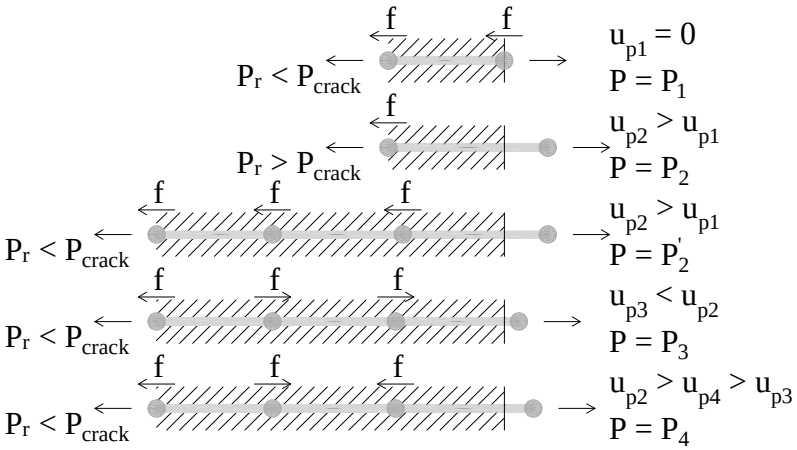

Fig. 3. The phases of cyclic pulling fiber

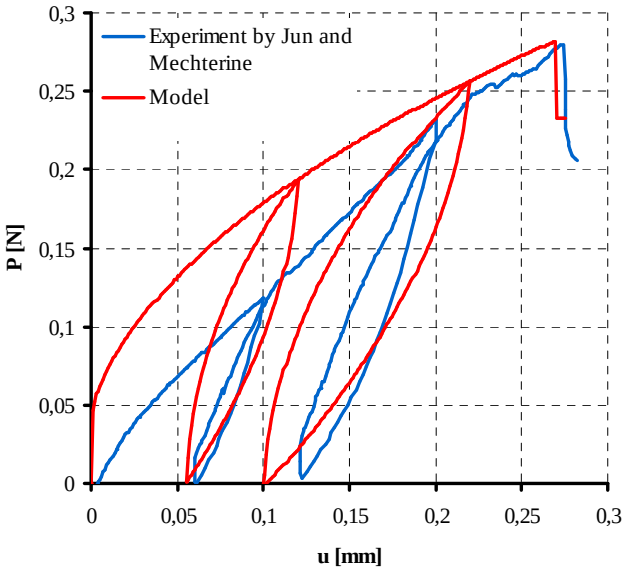

Fig. 4. Comparison fiber response under cyclic loading

4. COMPARING THE RESULTS WITH AN EXPERIMENT

To verify the model we used data measured during the pull-out experiment of the fiber from matrix with cyclic loading [3]. This experiment was performed on the PVA fibers pulling out from cement matrix. We don't know the exact values of material parameters, but our aim was to capture the best results measured during the experiment. Comparison of results from the experiment and the FEM model are shown in Figure 4.

5. CONCLUSION

From the results in Figure 4 it is evident that the model can capture well the response of single fiber measured during the experiment. Differences can be caused by the arrangement of the experiment. It is also evident from Figure 4 that the slope of the unloading curve gradually decreases and thus decreases the overall stiffness of response. When unloading (at zero force at the free end of the fiber), the residual length of the pulled fiber at the free end is approximately equal to half the maximum of the pulled length.

Compared to analytical relationship this model neglects elastic deformation of the surrounding cement matrix. On the other hand, it takes into account real distribution of frictional forces, including the removal of these forces on the pulled part of the fiber.

This model also allows monitoring the distribution of stress in the fiber along its length at various points of the loading curve.

Results can be also used in modeling the behaviour of single crack response (cohesive law) with consideration of pulling fibers on its both sides.

ACKNOWLEDGEMENT

The presented work has been supported by a research grant SGS11/021/OHK1/1T/11.

REFERENCES

[1] LIN, Z., et al. On interface property characterization and performance of fiber-reinforced cementitious composites. *Concrete Science and Engineering*. 1999, 1, pp. 173-184. Available from WWW: <http://ace-mrl.engin.umich.edu/NewFiles/publications/zlin_ CSE99.pdf>.

[2] YANG, E.H.; LI, V.C. Fiber-Bridging Constitutive Law of Engineered Cementitious Composites. *Journal of Advanced Concrete Technology*. 2008, 6, 1, pp. 181-193. Available from WWW: <http://ace-mrl.engin.umich.edu/NewFiles/publications/2007/ yang-fiber-bridging.pdf>.

[3] Jun, P.; Mechterine, V. Institute of Construction Materials, TU Dresden Germany.

NANOFIBERS: INFLUENCE OF SURFACE THREATMENT ON MECHANICAL PROPERTIES OF CEMENT PASTE

RYPAROVÁ PAVLA[1], ALEŠ WÁGNER[2], JAN MUKAŘOVSKÝ[3], PAVEL TESÁREK[4]

Abstract: *The article deals with the use of nanofibers with different weight per unit area as a surface treatment applied on cement paste test samples. As the goal, there was the determination of the influence of nanofiber surface treatment on temperature distribution during the development of cement paste hydration heat of the samples. The development of hydration heat has fundamental influence on the final strengths of indurated cement paste.*

Keywords: *Nanofibers, cement paste, mechanical properties, hydration processes.*

1. INTRODUCTION

Problems related to cement hydration processes in wet concrete are generally known. There are designed varied treatments to prevent or at least limit cracking (related to shrinkage, drying up, etc.) at the early phases of hardening and solidification process of the concrete and cement based materials. Furthermore, also the final mechanical properties (compressive strength, tensile strength in bending, and modulus of elasticity) can be negatively influenced during the hydration processes [1]. The treatment is usually related to the desirable design of wet concrete, the concrete structure or component size, etc. but also to the surface treatment of not covered structure surfaces (usually horizontal and large) especially during the first few days after casting. As the surface treatment there is used complete covering or protection of horizontal surfaces (reinforced concrete floors) by using plastic foils or different spray

[1] Mgr. Pavla Ryparová; Czech Technical University in Prague, Faculty of Civil Engineering; Thákurova 7, 166 29 Prague 6, Czech Republic, pavla.ryparova@fsv.cvut.cz.

[2] Ing. Aleš Wágner, Czech Technical University in Prague, Faculty of Civil Engineering; Thákurova 7, 166 29 Prague 6, Czech Republic, ales.wagner@fsv.cvut.cz.

[3] Ing. Jan Mukařovský, Ph.D.; Czech Technical University in Prague, Faculty of Civil Engineering; Thákurova 7, 166 29 Prague 6, Czech Republic; jan.mukarovsky@fsv.cvut.cz.

[4] Ing. Pavel Tesárek, Ph.D.; Czech Technical University in Prague, Faculty of Civil Engineering; Thákurova 7, 166 29 Prague 6, Czech Republic, tesarek@fsv.cvut.cz.

application or coating. All that should prevent from excessively high water vaporization and prevent or limit the cracking [2].

As the surface treatment, there can be also used the nanofibers that have specific properties. Using the electrospinning method (NanoSpider technology by Elmarco), that is successfully used in industry which reduces the cost of nanofibres to an acceptable level and that enables spinning of different types of polymers where the properties of nanofibers can be continually modified according to the need, there arise a wide field of potential use of nanofibres in building. Specifically, the nanofibers can be used as membranes with continually variable barrier properties, fibres for protection of wet concrete, or e.g. fibres with implemented particles with biocide effects. There are also studies about composites of PVA and cement. The nanofibers can be used, according to the polymer type, as stabilized fibers against humidity or soluble in humid environment.

2. MATERIALS AND SAMPLES

Tested samples were made from cement paste which was prepared using cement CEM 42.5 R (Mokrá, Czech Republic). The water/cement ratio was in this case 0.41, the cement paste was prepared by hand.

The nanofibers of different weights per unit area (0.1; 5 and 10 g/m^2) were spun on laboratory device Nanospider in Center for Nanotechnology in Civil Engineering (Faculty of Civil Engineering, CTU in Prague). The nanofibers were spun from PVA with crosslinking agents and finally stabilized by heating up at temperature around 140 °C. The nanofiber ifself was spun on polymeric support textile (spunbond) with 18 g/m^2 weight per unit area that was made from polypropylene (PP) with antistatic treatment.

Six different sets of samples were tested, which were denotes as: A – samples without surface treatment (reference samples), B – samples only with the spun bond, C – samples with the nanofibers and the spun bond (position of the spun bond was above the nanofibers), square weight of the applied nanofibers was 0.1 g/m^2, D – samples with the nanofibers and the spun bond, square weight of the applied nanofibers was 5 g/m^2, E – samples with the nanofibers and the spun bond, square weight of the applied nanofibers was 10 g/m^2, F – samples with 1 mm layer of PVA (applied on a free surface).

The cement paste was placed on crystallization basins with diameter 100 mm and a high 15 mm and in forms with diameters of 20x20x100 mm. Then the surfaces of tested samples were

modifying using the spun bond or the nanofibers with the spun bond. Finally, the samples were placed at laboratory conditions with temperature 20 ± 2 °C and relative humidity 30 ± 2.

3. EXPERIMENTAL RESULTS

The results can be divided into two groups. In the first group, there are the results from mechanical tests. In the second group, there is investigated the water vaporization from the surface of wet cement paste samples.

From the mechanical properties, there were measured the compressive strength and tensile strength in bending [3]. The standard testing of the compressive strength was done on bearing area 40x20 mm, the tensile strength in bending was done as standard three point bending with the width of span of 60 mm. The cement paste samples with the dimensions of 20x20x100 mm were treated on the surface with the nanofibers of different weight per unit area or treated different way as mentioned above. The samples were stored in laboratory environment after casting and subsequently tested after 28 days [4]. These results were compared with the reference samples without any special treatment. The different ways of surface treatment did not led to differences in the results, the measured differences were up to 10 % which can be considered as measurement error [5], [6].

The influence of surface treatment on water vaporization from the free surface of samples was measured as time dependent weight (water) loss during first 28 days after casting. After this period, there was only minimal weight (water) loss. The typical time behavior of the single sample sets is shown on Fig. 1. It is evident that all the samples had uniform time behavior where are no evident differences between the sample sets of different surface treatment. The biggest differences arrived on the 5th day when the variance arose up to 10 %. It is necessary to note that all the samples didn´t have the same initial weight (volume) because not all the basins were filled up equally.

The measured results can be interpreted as follows:

I. The nanofibers after its heat stabilization can be spread (applied) on the surface of wet cement paste without problems. The nanofibers adhere to the wet sample surface thanks to the water included in the cement paste and large surface area of the nanofibers.

II. The nanofibers bound with the wet cement paste. After 28 days it is possible to separate the nanofibers (with 5 and 10 g/m^2) from the cement paste but on the bottom of the nanofibers there are resisting the rest of hydration products of the clinker minerals.

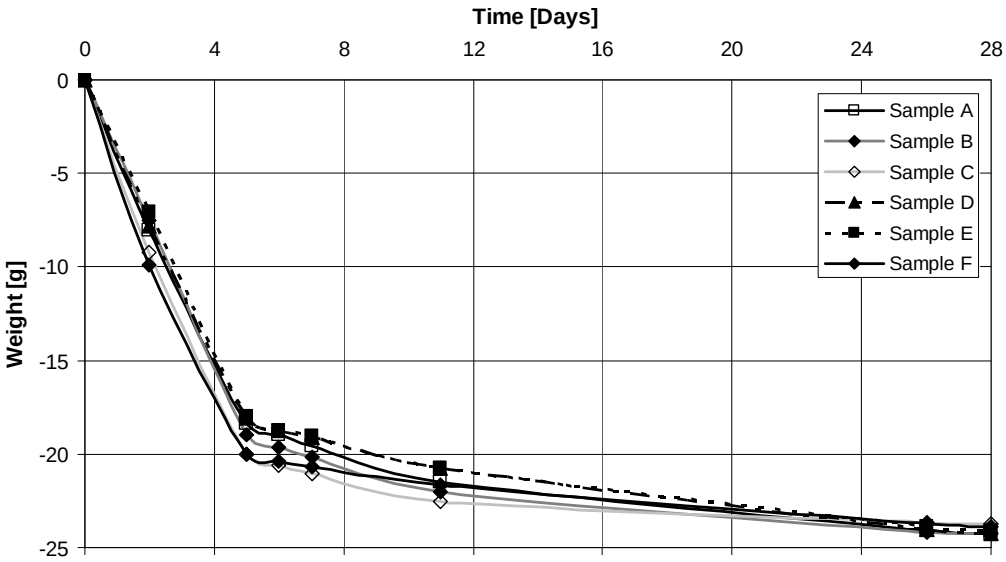

Fig. 1. Water loss of the tested samples

4. CONCLUSIONS

The article describes the first known (published) experiments related to the application of nanofibers on the surface of wet cement paste. In the described experiments, there was proved the real possibility of application of material from the "nano" sphere on the surface of "macro" material, although it was "fine" cement paste. The way of application could be compared to upholstering where the thin layer of nanofibers is spread on the wet surface of building material.

The fundamental question is whether there got to an interaction between the material surface and the surface treatment (nanofibers). Whether the bonding of these two materials was caused only by the large specific areas of the nanofibers or it was caused also by any interaction between PVA and hydrated clinker minerals or other hydration products originated from the hydration of cement paste.

ACKNOWLEDGEMENT

This outcome has been achieved with the financial support of the Ministry of Education, Youth and Sports of the Czech Republic, project No. 1M0579 – CIDEAS.

REFERENCES

[1] Tydlitát, V., Tesárek, P., Černý, R., 2008, *Effects of the Type of Calorimeter and the Use of Plasticizers and Hydrophobizers on the Measured Hydration Heat Development of FGD Gypsum,* In: Journal of Thermal Analysis and Calorimetry. vol. 91, no. 3, p. 791-796. ISSN 1388-6150.

[2] Němeček, J., Šmilauer, V., Kopecký, L. 2009, *Characterization of Alkali-activated Fly-ash by Nanoindentation*, In: Proceedings of the Nicom3 – Nanotechnology in Construction 3. Berlin: Springer-Verlag, 2009, p. 337-343. ISBN 978-3-642-00979-2.

[3] Padevět, P., Wilczynská, A., Tesárek, P., 2010, *Determination of Compressive and Bending Strength of Hardened Gypsum***,** In: Experimentální Analýza Napětí 2010. Olomouc: Palacky University, 2010, p. 301-305. ISBN 978-80-244-2533-7.

[4] Hájková, A., Padevět, P., Plachý, T., Němcová, H., Tesárek, P., 2011, *Study of FGD Gypsum Mechanical Properties – Before and After Recycling*, In: Experimentální analýza napětí 2011. Brno: Brno University of Technology, 2011, p. 79-84. ISBN 978-80-214-4275-7.

[5] Tesárek, P., Wilczynská, A., Korecký, T., Padevět, P., 2010, *Mechanical Properties of Gypsum Blocks after Fire***,** In: Experimentální Analýza Napětí 2010. Olomouc: Palacky University, 2010, vol. 1., p. 431-434. ISBN 978-80-244-2533-7.

[6] Tesárek, P., Mraček, T., Padevět, P., 2010, *Material Properties ag a Gypsum Block Exposed to Influence of Weather***,** In: Experimentální Analýza Napětí 2010. Olomouc: Palacky University, 2010, p. 427-430. ISBN 978-80-244-2533-7.

INELASTIC CALIBRATION OF PARTICLE MODELS USING CELLS WITH PERIODIC BOUNDARY CONDITIONS

JAN STRÁNSKÝ[1], MILAN JIRÁSEK[2],

Abstract: *A systematic approach to the calibration of particle models, i.e. characterizing a relationship between microscopic (defined on the level of individual interparticle bonds) and macroscopic parameters, using cells with periodic boundary conditions is presented, focused on inelastic conditions. To demonstrate the applicability of the described method, the plane stress failure envelope for the investigated model is constructed for different combinations of microscopic parameters.*

Keywords: *Particle models, calibration, periodic boundary conditions, multi-axial loading, failure envelope*

1. INTRODUCTION

Using discrete numerical methods, the studied problem is discretized by discrete elements (rigid spherical particles with uniform diameter in this paper), which are mutually connected by deformable bonds. “Microscopic” constitutive parameters of these bonds (normal and shear stiffness, tensile strength and ductility and shear yielding parameters in this paper) influence the behavior of the whole model on the macroscopic scale and the micro-parameters are usually identified (calibrated) using some kind of optimization (from the easiest trial-and error method to sophisticated sensitivity analysis) such that the macroscopic behavior of the model corresponds to the actual behavior (e.g. to the experimentally observed one) as closely as possible. For this purpose, periodic boundary conditions (PBCs) seem to be suitable tool.

All described methods were implemented into open-source software YADE [1], which was chosen for numerical simulations.

[1] Ing. Jan Stránský; Czech Technical University in Prague; Thákurova 7, 166 29 Prague, Czech republic; jan.stransky@fsv.cvut.cz

[2] Prof. Ing. Milan Jirásek, DrSc.; Czech Technical University in Prague; Thákurova 7, 166 29 Prague, Czech republic; milan.jirasek@fsv.cvut.cz

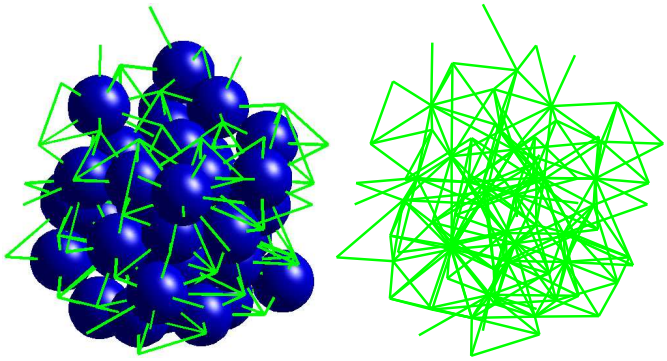

(a) *(b)*

Fig. 1. Illustration of particles (a) and bond network (b)

2. PERIODIC BOUNDARY CONDITIONS

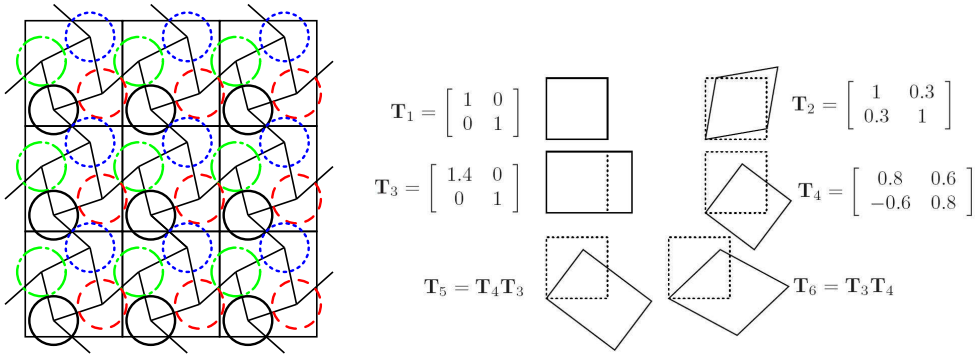

(a) *(b)*

Fig. 2. 2D illustration of periodic cell (a) and 2D illustration of the cell transfromations (b)

Consider a periodic cell as a block filled with a periodic assembly of particles and bonds. Periodicity means that this cell (as well as all its particles and bonds and all their properties – velocity, stress, damage etc.) is surrounded by identical cells shifted along the cell edges, see fig. 2a. In quasi-static (still dynamic) case, the periodic simulation is governed by the shape of periodic cell. We can modify the periodic cell via its 3x3 transformation matrix **T** (identity matrix initially) in two basic ways: rotation (when no strain occurs) and deformation (normal or shear strain without rotation), see fig. 2b. At the beginning of our simulation, the cell is rotated to the requested position. The computational procedure in a generic k-th step of simulation is as follows: First, the polar decomposition [2]

$$\mathbf{T}_k = \mathbf{UH} \qquad (1)$$

is performed on **T**. **U** is an orthogonal matrix and **H** is a positive semi-definite symmetric matrix. Apart from this mathematical definition, polar decomposition has a straightforward geometric meaning: **U** represents rigid body rotation and **H** is related to the shape change. In terms of infinitesimal strain theory, the strain **E** is obtained as

$$\mathbf{E} = \mathbf{T} - \mathbf{I}, \qquad (2)$$

where **I** is the identity matrix. Another definition of strain (e.g. logarithmic) could be incorporated.

The prescribed strain increment (in global coordinates) $\Delta\mathbf{E}$ is then appropriately rotated to cell's local coordinates and added to the shape matrix **H**. Afterwards, the new value of **T** is composed from **U** and new **H**:

$$\mathbf{T}_k = \mathbf{UH}, \qquad \mathbf{T}_{k+1} = \mathbf{U}(\mathbf{H} + \mathbf{U}^T\Delta\mathbf{E}\mathbf{U}) \qquad (3)$$

Prescribed strain components can be directly applied via the cell's shape change. However, stress cannot be prescribed directly. Therefore, we developed a special strain predictor, which considers the values of stress and strain in a few last steps and predicts the strain value for the next step such that the value of stress is as close as possible to the prescribed one, see [1] for more details. The stress is computed according to [3]

3. CALIBRATION

The topic of DEM calibration was studied by many authors [4,5,6,7], but only a few of them used periodic boundary conditions [8] and, according to our knowledge, there is no study of PBC in combination with post-peak behavior and strain localization. In inelastic calibration (usually fitting ultimate stress/strain and shape of stress-strain diagram under specific load conditions - typically uniaxial tension or compression), using PBC can reduce (unreal) local stress concentrations when applying prescribed displacement or force on certain particles.

For the case of uniaxial tension, a problem can arise when applying prescribed stress/strain on opposite "faces" of a specimen. If the sphere packing of the face is regular, the transition of regular to irregular (random) particle structure is usually broken and damaged first, before the "real structure" can be investigated. Another possibility would be to cut a plane from random packing and fix some particles up to a given distance from the face, but this can lead to stress

concentration at the transition of fixed and unfixed particles and devaluation of simulation results. For this reason, the periodic boundary conditions seem to be suitable solution.

However, all that glitters is not gold. In the calibration with the help of PBC, we have to pay attention to the cell orientation with respect to the load, especially if strain localization occurs. In general, there exists an "optimal" orientation of the periodic cell, where the localized zone is parallel to the cell surface or is crossing the cell from one corner to another. For the simple case of uniaxial tension, the optimal orientation is zero. Then the localization zone (crack) has the minimal area (and is only one) and the minimal amount of energy is needed to split the cell. For other orientations, the periodic boundary conditions force the crack crossing the cell boundary to continue at the periodic image of the cross point on another cell edge (see fig. 3). The crack is then longer than in the ideal case, more energy is needed for its propagation and the behavior of the cell is more ductile (see fig. 4a). Notice the same behavior in pre-peak (elastic) range and different behaviors in post-peak (inelastic) range. The most ductile response is exhibited by a cell rotated by about 30°, the most fragile (as expected) by an unrotated cell. Results for 45° lie in between, see fig. 4 for illustrative example.

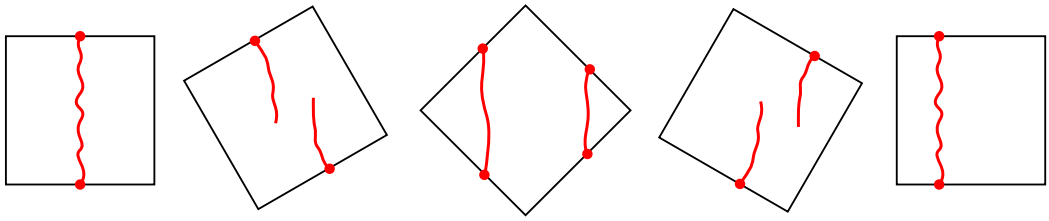

Fig. 3. Different localization zone using PBC for uniaxial tension in horizontal direction

In a general calibration procedure, the most brittle (optimal) cell position has to be found numerically and its behavior is considered as the real one (unaffected by periodic boundary conditions).

4. RESULTS

For the case of uniaxial tension, the most brittle ("optimal") behavior is obtained for a non-rotated cell. For the case of uniaxial compression, the most fragile behavior occurs approximately for a rotation between 20◦ and 30◦ and for simple shear near 45◦. An important fact for all the studied cases is that the pre-peak (elastic) response is the same for all orientations (verifying isotropy of the model) and the strength (maximum reached stress) is

also almost identical for all cases. Under this assumption, the plane stress failure envelope is constructed for different material parameters in fig. 5.

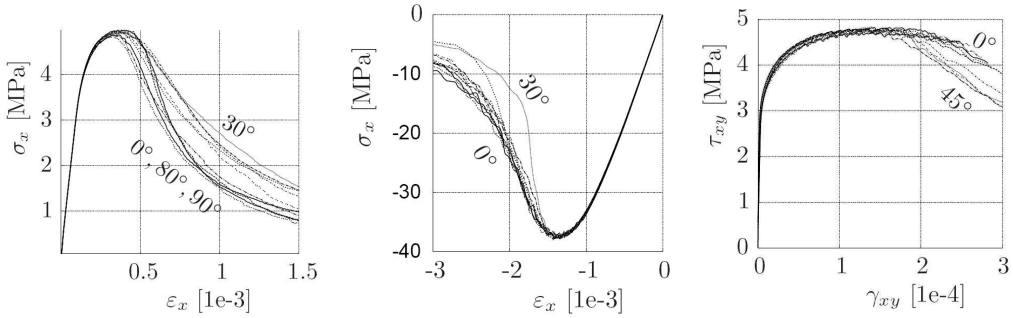

(a) *(b)* *(c)*

Fig. 4. Results for uniaxial tension (a), uniaxial compression (b) and simple shear (c)

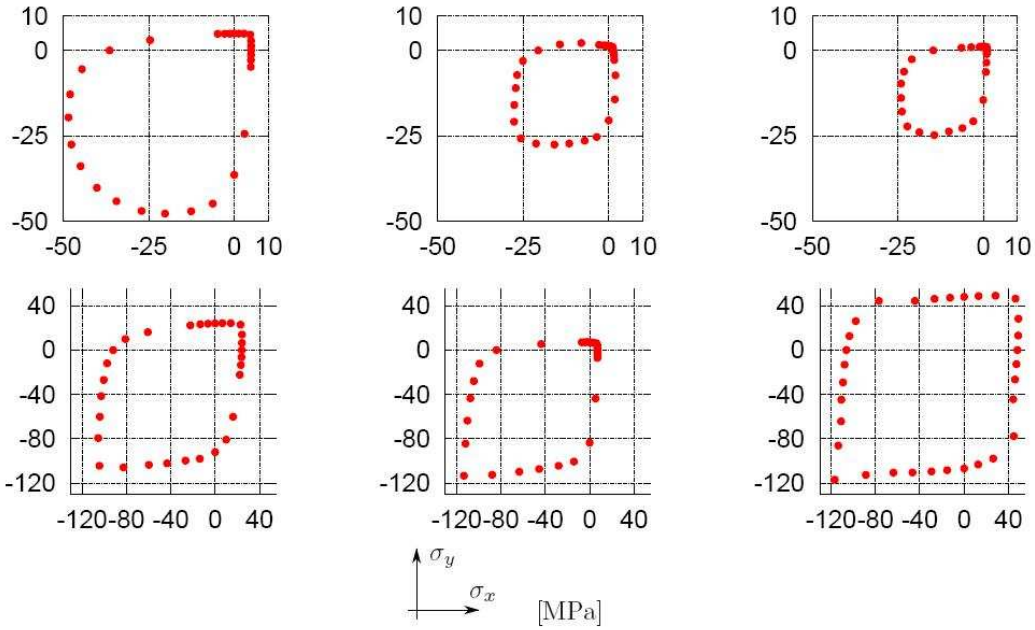

Fig. 5. Plain stress failure envelope constructed for different sets of micro-parameters

5. CONCLUSION

A systematic calibration method for discrete models with the help of periodic boundary conditions was presented. This method is applicable to any type of particle model and for both elastic and inelastic material parameters identification. In the case of inelastic calibration, PBC can reduce local stresses due to force or displacement prescribed on certain particles. A special attention has to be paid to the cell orientation with respect to the load. For realistic

results, the optimal orientation (without negative effects of PBC) has to be found and the parameters should be calibrated on such an orientation. This orientation is parameter-dependent, so by changing the parameters to be optimized, the optimal calibration orientation can be changed as well.

ACKNOWLEDGEMENT

Financial support of of the Czech Technical University in Prague under project SGS11/021/OHK1/1T/11 is gratefully acknowledged.

REFERENCES

[1] Šmilauer, V., Catalano, E., Chareyre, B., Dorofeenko, S., Duriez, J., Gladky, A., Kozicki, J., Modenese, C., Scholtes, L., Sibille, L., Stránský, J. and Thoeni, K. 2010. *Yade Documentation*. The Yade Project, 1st ed., http://yade-dem.org/doc/.

[2] Computing the polar decomposition - with applications. 1986. *Siam J. Sci. Stat. Comput.* 160–1174.

[3] Kuhl, E., D'Addetta, G. A., Leukart, M. and Ramm, E. 2001. Microplane modelling and particle modelling of cohesive-frictional materials. In *Continuous and Discontinuous Modelling of Cohesive-Frictional Materials*, ed. P. A. Veemer et al. Springer, Berlin, 31–46.

[4] Wang, Y. N. and Tono, F. 2010. Calibration of a discrete element model for intact rock up to its peak strength. *Int. J. Numer. Anal. Methods Geomech*. 34:447–469.

[5] Cotzee, C. J. and Els, D. N. J. 2009. Calibration of discrete element parameters and the modelling of silo discharge and bucket filling. *Comput. Electron. Agric.* (2009) 65:198–212.

[6] Grima, A. P. and Wypych, P. W. 2011. Development and validation of calibration methods for discrete element modelling. *Granular Matter* 13:127–132.

[7] Wang, Y. and Mora, P. 2008. Macroscopic elastic properties of regular lattices. *J. Mech. Phys. Solids* 56:3459–3474.

[8] Miehe, C., Dettmar, J. and Z¨ah, D. 2010. Homogenization and two-scale simulations of granular materials for different microstructural constraints. *Int. J. Numer. Methods Eng.* 83:1206–1236.

ANODIC OXIDATION – SIMPLE WAY TO PROTECT METALS WITH LAYERS THINNER THAN 1 μm

JOSEF VLK [1], BRUNO SOPKO [2]

Abstract: *The oxidation process affects most of metals exposed to humid environment. This behavior is called corrosion. There are many ways to protect metals from corrosion, like paintings or cover of anti-corrode metals, but sometimes is the oxidation useful, for example in case of aluminum or titanium.*

Keywords: *Anodic oxidation, Metal protection, Humidity sensor*

1. INTRODUCTION

Anodic oxidation as a protection method constitutes the primary corrosion measure taken usually in strongly aggressive industrial acidic or alkaline solutions. The main purpose of its use is to ensure sufficient resistance of metal against uniform and localized corrosion. Pure environment is another purpose for application of anodic oxidation [1-2].

A capacitive humidity sensor with a capacitor based on oxidised material with two metallic electrodes is usually used as an effective tool for examination of layers prepared by anodic oxidation. Tantalum is usually used to understand and manage the anodic oxidation process. A moisture sensitive layer of tantalum pentoxide inserted between the electrodes serves as a dielectric. The dielectric is critical for humidity measurement in humidity sensors [3]. In common humidity sensors of this kind, polymer film is used as the dielectric layer. Some of humidity sensors are using oxides layer on a metal like aluminium, tantalum etc, or a combination of these layers, as a dielectric in a capacitor. The electrode based on Ta/Ta_2O_5 layers could be used as a gate in MOSFET under the interdigital structure [4]. Final dielectric is according to the technology either homogeneous and nonporous (used only as a dielectric for separation of a capacitor), or inhomogeneous and porous by purpose. Tantalum pentoxide

[1] Josef Vlk, Department of Physics, Faculty of Mechanical Engineering, Czech Technical University in Prague, Technická 4, Prague 6, CZ-16607, Czech Republic; josef.vlk@fs.cvut.cz

[2] Bruno Sopko, Department of Physics, Faculty of Mechanical Engineering, Czech Technical University in Prague, Technická 4, Prague 6, CZ-16607, Czech Republic; bruno.sopko@fs.cvut.cz

layer prepared by anodic oxidation or by thermal oxidation is usually employed for creation of homogeneous films. Another extreme is oxide layer, which is completely porous. In the case of introducing the porous layer to humidity, the water molecules are adsorbed, therefore the capacity of the layer is changing [3-5].

The process of anodic oxidation is explained with a following mechanism. A tantalum pentoxide layer is created on the surface of a metal electrode of humidity sensor after the tantalum electrode is dipped into the electrolyte. The intensity of an electric field in the Ta_2O_5 layer is very high, even up to 10^7 V/cm. Under the influence of this field, oxygen ions migrate in the direction towards tantalum electrode and tantalum ions towards the electrolyte. This diffusion process takes place until the electromotive force, created by the gradient of ions, is in the equilibrium with the outer voltage. After that, the oxidation process stopped. This method is used for very accurate and reproducible thickness of Ta_2O_5 layer. The thickness depends only on the applied voltage [4].

2. EXPERIMENTAL SET-UP

For anodic oxidation of tantalum, a direct current voltage source was designed and created. Maximum voltage is 48 V, maximum current is 25 mA. Optimal current density is 1 mA/cm^2 in galvanostatic mode. Anodic oxidation took place for 1 hour in the SIMAX beaker with different electrolytes. The temperature of the electrolyte was controlled. The set temperature was 25 °C with the deviation of 0.5 °C. The electrolyte was stirred during the process by electromagnetic stirrer for better distribution of the heat and stabilization of the solution's homogeneity. Negative electrode was created by an alumina plate with sputtered gold. Positive electrode was created by tantalum plate. Before and after this deposition, both electrodes (the alumina plate with gold and the tantalum plate) were washed by water and dried for 1 hour at the temperature of 50 °C. The thickness of the layer after deposition was measured by Tencor Alphastep 200 Profilometer.

Electrolytes used for experiments were:

a) Solution of ammonium citrate in water – the solution was prepared by dissolving 30 g in 1 l of distilled water and after a period of homogenization was filtrated and used for anodic oxidation.
b) Solution of ammonium citrate in glycerol – the solution was composed from 1% neutral ammonium citrate in 90% glycerol solution (the rest – 10 % - was water).

This solution was prepared by dissolving 12.43 g ammonium citrate in 121 ml of distilled water. After filtration the solution was completed with glycerol to 1 l.

c) Solution of ammonium tartrate in glycerol – the solution was composed from 1% neutral ammonium tartrate in 90% glycerol solution (the rest – 10 % - was water). This solution was prepared by dissolving 12.43 g ammonium tartrate in 121 ml of distilled water. After filtration the solution was completed with glycerol to 1 l.

3. RESULTS AND DISCUSSION

3.1 ANODIC OXIDATION

The final colour of deposited Ta_2O_5 varied according to the thickness o the layer. The film thickness of prepared samples was in the range between 100 and 600 nm. There was prepared a scale covering this range. The thickness was easily recognized by a different colour. The colour range was from blue to grey. The typical thickness gained after 1 hour by the voltage of 48 V was deep violet with thickness around 200 nm.

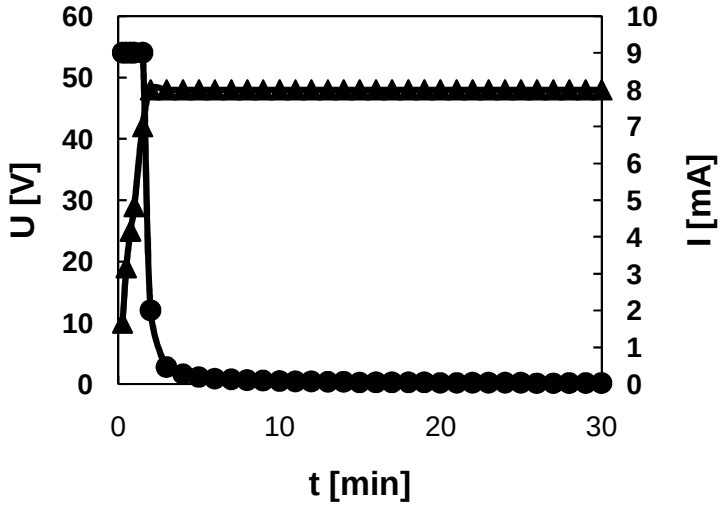

Fig. 1: Dependency of the voltage (▲) and current (●) on the time.

The typical dependency of the voltage and current on the time is pictured in Fig. 1. After an initiation of the procedure (usually around 1 min), the anodic oxidation took place. There was no evidence of stating the equilibrium between the electromotive force and the outer voltage. For the film thickness an empirical formula was obtained:

$$d = 9 + 3.67 \cdot (U + 0.82), \qquad (1)$$

where d is the thickness in nm and U is the applied voltage in V. Eq. 1 is valid only in the studied voltage range (from 10 to 48 V) and applied design of apparatus for anodic oxidation.

3.2 TANTALUM PENTOXIDE LAYER TESTING

As the main criteria for comparison of three tested electrolytes, the reaction on humidity was taken. In the Fig. 2 there are summarized the changes in capacity of the dielectric layer prepared by anodic oxidation in water solution of ammonia citrate. The reproducibility of the response is in relative scale good, but not in absolute. The next two electrolytes based on glycerol possessed almost the same results.

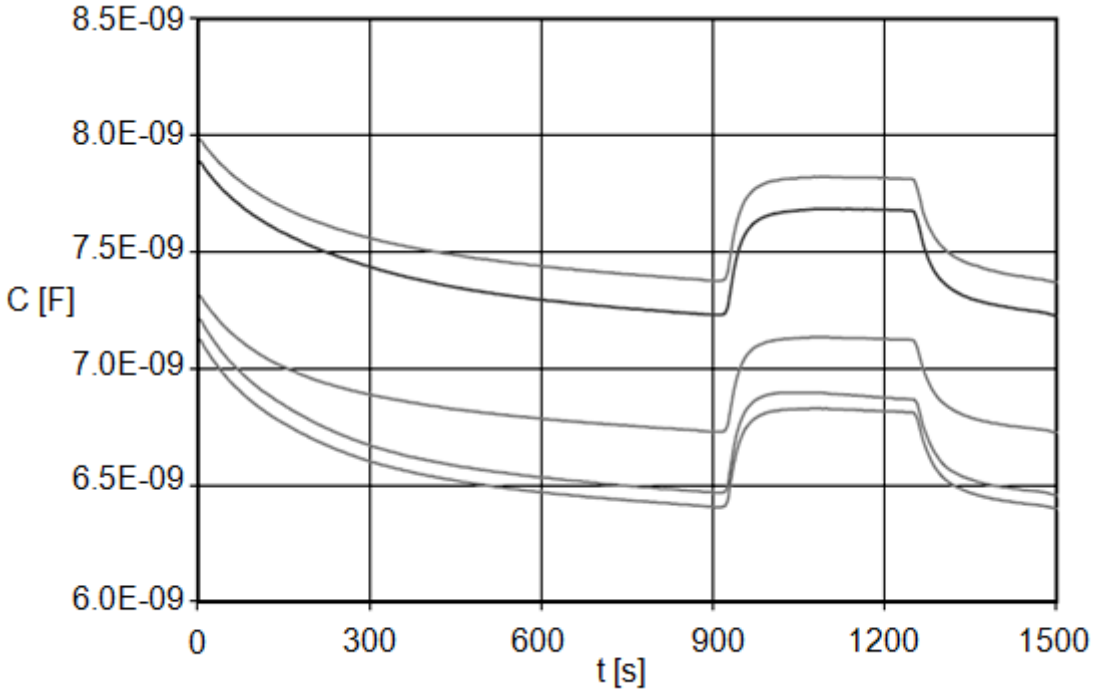

Fig. 2: *The reaction on the humidity of 60 %. Different curves represent different samples.*

4. CONCLUSION

The comparison of three tested electrolytes did not provide the best or the worst one. Therefore the main outcomes of this work are optimized conditions for anodic oxidation of tantalum and an empirical description of tantalum pentoxide film thickness. The next step of our work will be optimizing the reproducibility of the layer properties and scaling up the samples.

ACKNOWLEDGEMENT

This work was financially supported by the Grant Agency of the Czech Technical University in Prague, grant No. SGS11/149/OHK2/3T/12.

REFERENCES

[1] Glass, G.K., Hassainen, A.M., Buenfeld, N.R. 1997. *Monitoring the passivation of steel in concrete induced by cathodic protection*, Corros Sci 39, *8*, pp. 1451-1458.

[2] Novák, P. 2010. *Shreir's Corrosion* (Edit. Richardson, T.J.A.) 4, *4.24*, pp. 2857-2889.

[3] Balkus, K.J., Ball, L.J., Gimon-Kinsel, M.E., Anthony, J.M., Gnade, B.E. 1997. *A capacitance-type chemical sensor that employs VAPO-5, MnAPO-5 and MAPO-36 molecular sieves as the dielectric phase*, Sensor Actuat B-Chem 42, *67*, pp. 67-79.

[4] Comini, E., Baratto, C., Faglia, G., Ferroni, M., Vomiero, A., Sberveglieri, G. 2009. *Quasi-one dimensional metal oxide semiconductors: preparation, characterization and application as chemici sensors*, Prog Mater Sci 54, *1*, pp. 1-67.

[5] Caldararu, M., Munteanu, C., Chesler, P., Carata, M., Hornoiu, C., Ionescu, N.I., Postole, G., Bratan, V. 2007. *Supported oxides as combustion catalysts and as humidity sensors. Tuning the surface behavior by inter-phase charge transfer*, Micropor Mesopor Mat 99, *126*, pp. 126-131.

DESTRUCTIVE AND NONDESTRUCTIVE TESTING OF CONCRETE STRUCTURES AFTER FIRE

ONDŘEJ VRÁTNÝ[1]

Abstract: *The aim of this paper is to present selected destructive and non-destructive testing of reinforced concrete structures affected by fire, which are used in order to the properties of concrete and reinforcement.*

Keywords: *fire damages, concrete testing, concrete after fire, assessment of concrete*

1. INTRODUCTION

The effect of higher temperatures leads to chemical and physical changes in the structure of concrete and its mechanical properties as strength and modulus of elasticity are reduced. The temperature affects not only concrete but also on reinforcing steel and also influences the interaction of these two components of reinforced concrete. Another source of damage is the evaporation of water chemically and physically bounded in the concrete, which leads to general cracking and spalling of the reinforcement cover.

Structural damage and properties of concrete is influenced not only during the fire but also during the cooling process of the structure. The damage resulting from fire fighting water is of a very significant nature. This leads to a sudden cooling of the structure and consequently to significant stresses over the cross-section. The most accurate knowledge of the extent of structural damage needs to be obtained for the optimal design of remediation measures. It is important for smooth service life of the structure in upcoming decades. The price is often the decisive factor. If carried out research work, is appropriate to use simpler procedures for determining the level of structural damage and verify them using sophisticated laboratory tests. Therefore, a comprehensive picture of the structure in the optimum amount spending time and money is obtained.

Taking into account the above mentioned conditions and the complexity of the problem, destructive and non-destructive testing of concrete and reinforcement are an important part of the analysis of concrete structures once the fire is over.

[1] Title First Name Middle Name Surname; Full title of the Institution; Street, ZIP-code City, Country; E-mail

2. GENERAL INFORMATION ABOUT CONCRETE TESTING AFTER FIRE

Following part of the contribution is based on the (Bulletin 46), issued by the International Federation for Structural Concrete, which summarizes the knowledge of the issue *"Fire Design of Concrete Structures - Structural and Behavior Assessment"*. The Fire design is not only about the temperature behaviour on the constructions during fire, but also about checking the safety of the damaged structure. The conclusion of the construction testing has to be a definition of the best strategy for repairing or strengthening of the structure, as an alternative to the demolition. Information about the maximum temperature and damage as well as about the residual strength and stiffness in local position on the structure is very valuable for the assessment of the construction.

It is known that concrete naturally has a good behaviour at a high temperature. It depends on its incombustible nature and low thermal diffusivity. Following these facts is the propagation of thermal transients within the structural members slow which causes that during a fire very strong thermal gradients arise in the reinforcement cover. These result in the thermal damage only few centimetres deep. The damage and residual load capacity of the structure must be determined and assessed for the planning of any strengthening and reparations.

One of possible damages is spalling. The construction losses the external concrete layer and the deeper layers are exposed to the maximum temperature. In some cases the build-up of vapour pressure can result into an explosive expulsion of concrete chips, but it happens mostly within a relatively low temperature range (<400°C) and the damage inflicted by temperature is not significant.

In case of fire also chemo-physical transformations of concrete at increasing temperature are relevant. The physically combined water is released with the temperature of about 100°C, than the silicate hydrates are decomposed above 300°C and with 500°C occurs to the dehydration of the portlandite. The fire heat influences significantly the coarse aggregate too. The temperature above 600°C causes the beginning of conversion and decomposition [1]. According to [7], the concrete with siliceous aggregate loses near one half of its capacity at 650°C, while carbonate aggregate concrete exhibits nearly full capacity.

Aforementioned damage of concrete must be assessed with specific tests. After the fire expose the residual capacity and other main properties cannot be inspected with traditional destructive or non-destructive testing techniques. Concrete after fire is too heterogeneous

layered-material and therefore we have tree main possibilities of inspecting the material (Tab. 1.):

- Average response of the concrete cover
- Point by point response of small samples of different depths
- Special interpretation techniques for overall response of concrete

Tab. 1. Possible assessment of fire-damaged concrete structures [1]

Average response of the concrete cover	**Point by point response of small samples**	**Special interpretation techniques**
Schmidt rebound hammer	*Small-scale mechanical test*	*UPV indirect method*
Windsor probe	*Differential Thermal Analysis*	*Impact echo*
Capo test	*Thermo-gravimetric Analysis*	*Sonic tomography*
BRE internal fracture	*Dilatometry*	*Modal Analysis of*
Ultrasonic Pulse Velocity	*Thermoluminescence*	*Surface Waves*
	Porosimetry	*Electric Resistivity*
	Colorimetry	
	Microcrack-density analysis	
	Chemical analysis	

Basic methods that are commonly used to study the concrete after a fire are listed in the previous table. In the following sections of this contribution several selected methods will be presented. [1, 2 and 4]

3.1 VISUAL ASSESSMENT AND COLORIMETRY

The easiest observations technique is visual assessment. After cleaning the construction from the soot hidden cracks, spalls and distortions can be found in the structure. The structure can be cleaned with dry ice blasting, grit blasting, or chemical washing etc.

In the second step the traditional method for the assessment of concrete damage after a fire can be used. This method is based on the visual colour inspection of the cement matrix or concrete aggregate (Tab. 2). Colour changes in the concrete are based on the influence of the intense heat which are caused of chemical reactions. The colour of the material is associated with the approximate temperature of the concrete. For example, for the temperature range 300 °C - 600 °C, the colour changes to pink or red. This is due to the presence of iron compounds

in the aggregates which within the above mentioned temperature range dehydrates or oxidizes. When this change occurs, it is an important indication of a possible fast decrease of the concrete strength. Recently, there ~~is~~ has also been the possibility of using modern instruments for colour measurement of concrete components and therefore the paramount problem of this method, subjective evaluation, has been eliminated

Tab. 2. Physical Effects of Temperature on Concrete [7]

Temperature	**Colour Change**	**Changes in Physical Appearance and Benchmark Temperatures**	**Concrete Condition**
0 to 290°C	*None*	*Unaffected*	*Unaffected*
290 to 590°C	*Pink to red*	*Surface crazing – 300°C* *Deep cracking – 550°C* *Popouts over chert or quartz aggregate – 575°C*	*Sound but strength significantly reduced*
590 to 950°C	*Whitish Grey*	*Spalling, exposing not more than 25% of reinforcing bar surface – 800°C;* *Powered, light coloured, dehydrated paste – 575°C*	*Weak and friable*
950+°C	*Buff*	*Extensive spalling*	*Weak and friable*

Visual assessment can be used also to determine the highest temperature in the fire area and duration of the fire. The condition of structural members and associated materials can develop the heat intensity map (Tab. 3). Another possibility is the presence and condition of the timber based material. Fire duration can be determined from the thickness of the charred exterior material. [1, 2, 6, 7, 8 and 9]

3.2 CORE TEST AND CARBONATION TEST

The basic and most direct method of testing concrete is the core test. The estimation of the concrete strength carried out on testing cores cut from the structure. This test gives information about the entire core, but after the fire the strength varies along the core. The core test is still the first test of all available methods such as colorimetry, porosimetry, chemical analysis, etc. The carbonation test is usually also performed on the core.

Tab. 3. Physical Effects of Temperature on Various Materials [7]

Material	Examples	Condition	Temperature
Polystyrene	*Foam insulation; light shades; handles*	*Softens*	*50 to 60°C*
	Curtain hooks; radio containers	*Melts and flows*	*120°C*
Polyethylene	*Bags; film*	*Shrivels*	*49°C*
	Bottles; buckets	*Softens and melts*	*66°C*
UHMW / HD Polyethylene pipe	*Water and waste pipes*	*Melts, flows, bubbles, or burns*	*190°C*
Zinc	*Plumbing fixtures; flashing; galvanized surfaces*	*Drops formed*	*400°C*
Aluminium	*Small machine parts; brackets; toilet fixtures; cooking utensils*	*Drops formed*	*650°C*
Sheet glass	*Window glass; plate glass; reinforced glass*	*Softened or adherent*	*700 to 750°C*
		Rounded	*800°C*
		Thoroughly flowed	*850°C*
Brass	*Door knobs; furniture knobs; locks; lamp fixture; buckles*	*Sharp edges rounded or drops formed*	*900 to 1000°C*

Fig. 1. Carbonation phenolphthalein test [source: http://buildtest.com.my]

The carbonation test determines the carbonation depth by spraying the concrete with a phenolphthalein solution and measuring the depth of the discoloured zone. Carbonation depth is an important piece of information for the subsequent determination of the residual durability of fire damaged structure. Fire negatively influences not only the statics of the structure, but also its durability. [1]

3.3 SCHMIDT HAMMER TEST AND DRILLING RESISTANCE

The rebound hammer is a very popular tool for testing of materials. The test, called Schmidt hammer test, is very easy to perform. The Schmidt hammer test provides information about the surface hardness of the concrete. Properties of a surface layer with a thickness of about 20-30 mm can be determined. In case of fire damaged concrete the use of this test is very difficult. Due to the statistical reasons, it is necessary to execute a large number of tests. In general, this test is not very suitable for structures with heavily damaged surface (due to spalling), but for its simplicity and availability, it is used very often with some limitations of conclusions. Its application can be suggested for a fast detection of areas where the concrete of the exposed surface has lost 30-50% of its original strength.

Following the disadvantage of mere surface testing, the Schmidt hammer test, some more complicated methods of analyzing the properties of concrete after a fire on small samples from different layers were developed. The combination of the above mentioned methods promises a faster technique based on the measurement drilling resistance. This method can be described as a continuous "scanning" of the material resistance. Relevant sources generally recommend the use of this test in case of a severe thermal damage.

As with any indirect method of testing, it is necessary to establish a good correlation between the tested parameter, which, in this case, is work dissipated per unit drilling depth (J/mm), and compressive strength. Also, in this case, this relationship cannot be easily determined. Many different factors, such as fracture energy and aggregate hardness, have a huge impact on the results. The basis therefore is to always compare the results of the virgin material and the fire damaged concrete. [1, 3 and 9]

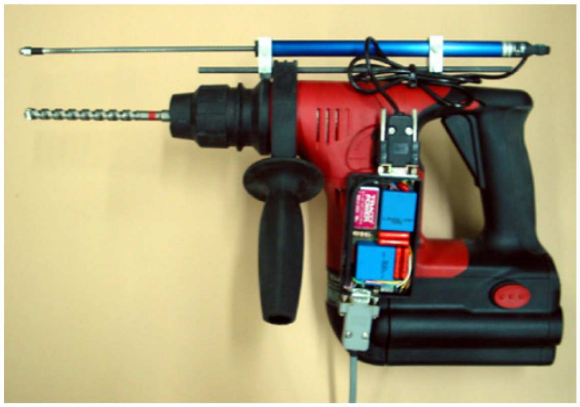

Fig. 2. The hammer drill fitted with the electronic circuits and displacement transducer [3]

3.4 CHEMO-PHYSICAL AND MECHANICAL TESTS AND CHEMICAL ANALYSIS

Chemo-physical tests can be described collectively as testing techniques based on repeated testing of small samples from different depths of the damaged concrete element under laboratory conditions. These techniques are based on chemo-physical transformations in the material.

The so-called "Disc Punching-Test" is a good example of mechanical tests suitable for testing the compressive strength of concrete. These are “punching” into thin disks, cut samples, of the damaged concrete. [1]

Chemical analysis can be performed in order to find the residual combined water in hardened cement or chloride in concrete. Chloride ions may attack the concrete during and after the fire due to the decomposition of plastic containing polychlorides, e.g. PVC. [1]

Petrographic examination and porosimetry are also very helpful test methods. [5]

4. CONCLUSION

In this article a few selected tests fire damaged concrete used to determine the degree of damage were featured. From the description, it is clear that for each of the tests significant use restrictions apply. Each of the methods have own limits and benefits. To achieve correct results, it is necessary to use appropriate tests with regard to the degree of damage of concrete and other conditions. It is also important to use the conceptual simpler logical follow-up techniques and sophisticated methods should be chosen to complement and verify methods for the optimal use of resources.

ACKNOWLEDGEMENT

I would like to thank prof. Jaroslav Procházka for conducting my study of the theme concrete structures after fire and for his valuable advices in case this paper.

REFERENCES

[1] Bulletin 46, 2008. *Fire design of concrete structures – structural behaviour and assessment*, Lausanne, International Federation for Structural Concrete

[2] Anderberg, Y., 2009. *Assessment of fire-damaged concrete structures and the corresponding repair measures*, Concrete Repair, Rehabilitation and Retrofitting II, London,
WWW: < http://dicata.ing.unibs.it/plizzari/CD/Pdf/087.pdf >

[3] Felicetti, R., 2009. *Combined while-drilling techniques for the assessment of the fire damaged concrete cover*, Proceedings of the Workshop "Application of Structural Fire Engineering", Prague, Czech Republic

[4] Fajman, P., 2009. *Postřehy o chování železobetonové konstrukce při požáru*, Beton TKS, 1/2009, 60 – 65 s.

[5] Ingham, J. P., July 2009, *Application of petrographic examination techniques to the assessment of fire-damaged concrete and masonry structures*, Materials Characterization, Volume 60, Issue 7, 11th Euroseminar on Microscopy Applied to Building Materials (EMABM), , 700 – 709 s.,
WWW: <http://www.sciencedirect.com/science/article/pii/S1044580308003173>

[6] Short, N. R., Purkiss, J. A., Guise, S. E., February 2001. *Assessment of fire damaged concrete using colour image analysis*, Construction and Building Materials, Volume 15, Issue 1, 9 – 15 s.,
WWW: <http://www.sciencedirect.com/science/article/pii/S0950061800000659>

[7] Gosain, N. K., Drexler, R. F., and Choudhuri, D., 09/2008. *Evaluation and Repair of Fire-Damaged Buildings*, STRUCTURE magazine, 18 – 22 s.

[8] Annerel, E., Taerwe, L., 2009. *Basic approach for the diagnosis of concrete after fire exposure*, Proceedings of the Workshop "Application of Structural Fire Engineering", Prague, Czech Republic

[9] Colombo, M., Felicetti R., September-October 2007. *New NDT techniques for the assessment of fire-damaged concrete structures*, Fire Safety Journal, Volume 42, Issues 6-7, Structures in Fire, , 461 – 472 s.,
WWW: <http://www.sciencedirect.com/science/article/pii/S0379711207000495>

CEMENT PASTE WITH VARYING AMOUNTS OF ADDED FLY ASH AS A BINDER IN CONCRETE: COMPRESSIVE STRENGTH AND TENSILE STRENGTH AFTER 28 DAYS

ONDŘEJ ZOBAL[1], PAVEL PADEVĚT[2],

Abstract: *Fly ash generated during coal combustion in thermal power plants is primarily considered as a waste material. However, this material has its potential and can be more widely used for construction purposes, as it is already happening in other countries around the world (Germany, USA, Australia). This paper presents the first results of measurement of compressive strength and bending tensile strength of cement paste with varying amounts of fly ash after 28 days.*

Keywords: *Fly ash, compressive strength, tensile strength*

1. INTRODUCTION

In the Czech Republic is around 50% of electric energy is still obtained from thermal power plants burning coal. Annually, on average produces about 8 million tons of fly ash. This fact places the Czech Republic's largest producers of power plant fly ash per capita in the world. In Fig. 1 is seen in the microscopic picture typical shape of fly ash. Fly ash is taken primarily as a waste material, but growing effort to use this material in industry, mainly in construction. In the U.S. example is the construction of highways [1].

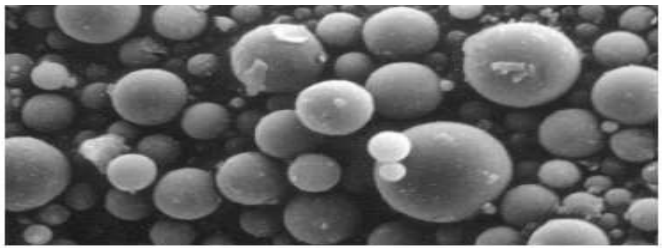

Fig. 1. Microscopic image of fly ash - 2000 x magnification, [1]

[1] Ing. Ondřej Zobal; Department of Mechanics in Faculty of Civil Engineering, CTU in Prague, Thakurova 7/2077, 166 29 Prague 6 – Dejvice, Czech Republic, ondrej.zobal@fsv.cvut.cz

[2] Ing. Pavel Padevět, Ph.D.; Department of Mechanics in Faculty of Civil Engineering, CTU in Prague, Thakurova 7/2077, 166 29 Prague 6 – Dejvice, Czech Republic, pavel.padevet@fsv.cvut.cz

It is therefore important to obtain information about its properties and behavior [2], alkali-activated fly ash can be, this issue deals with for example, [3]. This article describes an experiment, however, dealing only with the mechanical properties of fly ash added in varying amounts in the cement paste with no other additives after 28 days.

2. MATERIAL

For the purpose of the experiment was necessary to produce high-quality mixture of water, cement and fly ash. Coefficient of a mixture of water has a value of 0.4. Cement was obtained from the site Radotín and is a Portland cement CEM I 42.5 R. Fly ash from the site was chosen Mělník type fly ash in concrete. It is one of the best fly-ash in the Czech Republic, which is used in blended cements. It made several sets with different percentage of fly ash to the cement content in the mixture. Individual sets are described in Tab. 1, where you can see the development density of each set of mixtures. It can be seen that with a higher content of fly ash reduces the value of the density.

Tab. 1. Sets of test samples and their density

Type	CEM I 42,5R	Fly Ash	Volume density
[-]	[%]	[%]	[kg/m^3]
I	100	0	2059 ± 89
II	60	40	1820 ± 22
III	50	50	1844 ± 19
IV	40	60	1749 ± 32
V	30	70	1650 ± 29

3. SPECIMENS

For the experiment were designed two groups of samples, so that it can place the necessary measurements which have been scheduled:

- cylinders – diameter 10 mm, length 100 mm
  → made for compressive strength test
- prisms – 20 × 20 × 100 mm
  → made for test the tensile strength in bending

Test specimens in the shape of cylinders manufactured in special plastic molds. Prisms were made in the classic steel forms (see Fig. 2). After allowing 48 hours after the samples were placed in a water bath, where at 21 ° C are stored long term.

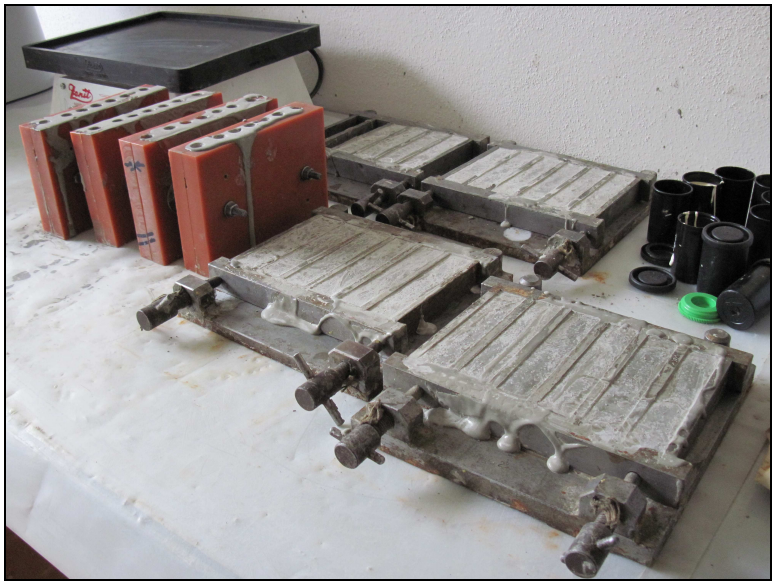

Fig. 2. Test specimens in the forms

4. METHODOLOGY

Were carried out two mechanical tests - determination of compressive strength and tensile strength. For both tests was used electromechanical testing machine MTS Alliance RT-30, the maximum loading force of 30 kN in compression and tension. The modified cylinders pressure test was performed. Cylinders were shortened from 100 mm in length 40 mm. Diameter samples did not change, remaining value of 10 mm and a loading area therefore the size of 78.5 mm2. At each sample was mounted strain gauge during the test, which recorded values of strain to calculate the size of the modulus of elasticity. The classic three-point bending test to obtain values of tensile strength in bending was performed on prisms. Prisms before the test has been modified. The load acted in the middle range of support and were placed 10 mm from the edge of the sample and span between supports (effective length) was therefore the value of 80 mm [4].

5. EVALUATION

In Fig. 3 shows the evolution of compressive strength for each set of test samples after 28 days. All measurements were statistically evaluated, it is shown for each result and standard deviation.

In Fig. 4 shows the development of tensile strength in bending for each set of test samples after 28 days. As with the compressive strength shown here is the standard deviation. The observed trends are summarized in the conclusion.

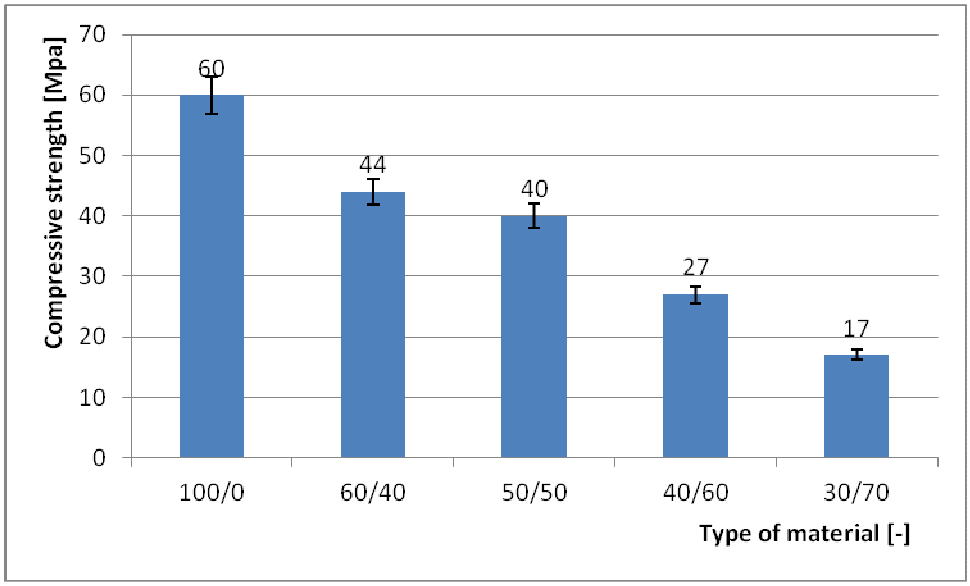

Fig. 3. Compressive strength after 28 days

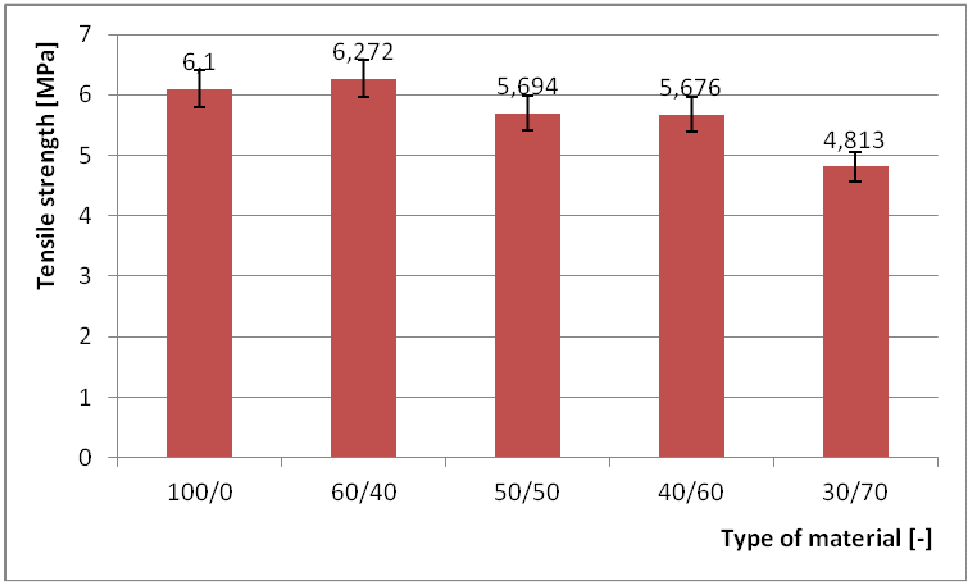

Fig. 4. Tensile strength after 28 days

6. CONCLUSION

Measurement results observed mechanical properties of cement and water mixture with different proportion of fly ash with a water factor of 0.4 without any additives and ingredients we now bring this knowledge (all measurements were statistically evaluated and has always been determined by standard deviation, which ranged up to 10%). Density with a higher ash content in the mixture decreases. Compressive strength after 28 days with a higher ash content also decreases. Pure cement has a value of compressive strength after 28 days of about 60 MPa when the mixture is only 30% cement and 70% fly ash, the compressive strength value

of the third. The tensile strength after 28 days is not increasing ash content in the mixture almost no effect, values range from about 5 to 6 MPa.

Another aim of our work is to continue to monitor the evolution of the material in time and focus on other properties such as static modulus of elasticity, heat of hydration, fracture energy, etc. We would like to pay and structure of materials at the micro level. Another objective is to improve and expand the database of fly ash produced in the Czech Republic and to create a comprehensive look at this material and could be better and more widely used for industrial needs.

ACKNOWLEDGEMENT

This experiment at the Faculty of Civil Engineering CTU in Prague could run the support of the project, SGS 10/136/OHK1/2W/11 "Advanced experimental methods".

REFERENCES

[1] American Coal Ash Association, 2003. *Fly Ash Facts for Highway Engineers*, Federal Highway Administration, Washington. p. 81.

[2] Fečko, P.: *Popílky*, Vysoká škola báňská, Technická univerzita Ostrava, 2003

[3] Hlaváček, P., Šmilauer, V., Šulc, R., Kopecký, L., Škvára, F., 2011. *Elastic properties of geopolymer concrete based on fly-ash*, In: 31st Cement and Concrete Science Conference 2011. London: Imperial College Press, p. 1-4.

[4] Zobal, O., 2010. *Vliv teploty nemateriálové vlastnosti cementové pasty*, Diplomová práce, Fakulta stavební ČVUT v Praze. p. 58.